

WET CHEMICAL SYNTHESIS STRATEGIES TO DEVELOP
ALUMINUM MANGANESE NANOPARTICLES
FOR HIGH DENSITY MAGNETIC RECORDING

by
MICHAEL ALLEN IVIE II

A DISSERTATION

Submitted in partial fulfillment of the requirements
for the degree of Doctor of Philosophy
in the Department of Chemical and Biological Engineering
in the Graduate School of
The University of Alabama

TUSCALOOSA, ALABAMA

2010

Copyright Michael Allen Ivie II 2010

ALL RIGHTS RESERVED

ABSTRACT

As the technology era grows rapidly, there is always a need for quick access to stored data. Magnetic tape is one type of recording media used of information storage. Its main use in computer applications is for archival storage and mass storage systems. Magnetic tape is a multi-component material consisting of a base film with a top layer of magnetic particles. Particles that are used for magnetic recording devices must exhibit good magnetic properties including large coercivity and saturation magnetization. As the need for tape performance and storage capacity increases, new types of particulate media are needed to meet these demands. One candidate of particles for future magnetic tape is ferromagnetic AlMn nanoparticles. AlMn has a ferromagnetic tetragonal $L1_0$ phase which is exhibited by a class of transition metal alloy systems such as FePt, CoPt, FePd, MnPt, etc. This phase in the AlMn binary system is labeled as the τ phase and has a large anisotropy value of approximately 10^7 ergs/cc which translates to good magnetic properties suitable for use in magnetic tape. The advantages of producing AlMn nanoparticles for magnetic recording are the low cost and abundance of precursor materials.

This dissertation investigated strategies to develop a solution phase chemical synthesis to produce AlMn nanoparticles. Metal nanoparticle systems are synthesized primarily by the reduction of metal salt precursors with a reducing agent in the presence of stabilizing agents in an organic solvent. Systems of metal nanoparticles with the

tetragonal $L1_0$ phase characterized by high anisotropy values such as FePt and MnPt are produced via this route, and these techniques are considered as a foundation to make AlMn nanoparticles. Cyclic voltammetry experiments give the reduction potentials of Al and Mn precursors to determine suitable reducing agents. The results of the AlMn nanoparticle synthesis attempts are chronicled by the reducing agent that was used in the reaction. Different combinations of precursors, surfactants, and solvents are used in coordination with the following reducing agents: superhydride ($C_6H_{16}BLi$), potassium (K), hydrogen (H_2), lithium aluminum hydride ($LiAlH_4$), and sodium (Na). Also, synthesis attempts of AlMn(X) tertiary nanoparticles and core-shell AlMn nanoparticles are presented.

LIST OF ABBREVIATIONS AND SYMBOLS

MRAM – magnetic random access memory

MP – metal particles

INSIC – Information Storage Industry Consortium

τ – tau phase

mm – millimeter

cm – centimeter

nm – nanometer

μm – micrometer

Tb – terabite

Gb – gigabite

in^2 – inches squared

Gb/in^2 – gigabites per inches squared

ME – metal evaporated films

GMR – giant magnetoresistive

TMR – tunneling magnetoresistive

Oe – oersteds

kOe – kilooersteds

K – anisotropy constant

$L1_0$ – tetragonal phase exhibited by a group of metal alloys with high anisotropy

$L1_2$ – an ordered crystallographic phase

erg – unit of energy

cc – cubic centimeters

erg/cc – ergs per cubic centimeter

% - percent

°C – degrees Celsius

°C/s – degrees Celsius per second

°C/min – degrees Celsius per minute

ϵ – epsilon phase

Å – angstrom

et al – Latin meaning “and others”

i.e. – Latin phrase id est meaning “that is”

{100} – crystallographic plane in brackets

hcp – hexagonal close packed

fct – face centered tetragonal

fcc – face centered cubic

tP2 – Pearson symbol for the $L1_0$ tetragonal crystal structure

B19 – Strukturbericht designation for the orthorhombic ϵ' phase

s – second

ϵ' – epsilon prime (intermediate phase) with an orthorhombic structure

torr – unit of pressure

emu – electromagnetic unit

emu/cc – electromagnetic units per cubic centimeter

M_s – saturation magnetization

r.f.– radio frequency

d.c. – direct current

W – watts

H – magnetic field

H_c – coercivity
mL – milliliter
g – grams
mmols – millimoles
nm/s – nanometers per second
V – volts or volume
mV – millivolts
kV – kilovolts
mA – milliamperes
μA – microamperes
kPa – kilopascals
D_c – critical diameter
M – moles per liter
C – Carbon
Acac – acetylacetonate
THF – tetrahydrofuran
DMF – dimethylformamide
TOA – trioctylamine
N₂ – nitrogen
H₂ – hydrogen
TMAOH – tetramethyammonium hydroxide
wt % - weight percent
at % - atomic percent
mol % - mole percent

α – alpha

β – beta

γ – gamma

λ – lambda

θ – theta

k – Boltzmann's constant (1×10^9)

n – diffraction order

ΔE – energy barrier

KV – anisotropy constant x volume (magnetic energy)

kT – Boltzmann's constant x temperature (thermal energy)

KV/kT – thermal stability of a magnetic material

H_0 – intrinsic coercivity

T – temperature

t – time

f_0 – constant (1×10^9)

m – constant

d – spacing between two adjacent crystallographic planes (d-spacing)

hkl – Miller indices

R – radius of diffraction ring (mm)

L – camera length (mm)

E – reduction potentials

JCPDS – Joint Committee on Powder Diffraction Standards

ICDD – International Center for Diffraction Data

Cu $K\alpha$ – copper k alpha

θ - 2θ – theta and two theta scan
V/s – volts per second
 μ A – microamperes
SHE – standard hydrogen electrode
SCE – standard calomel electrode
GC – glassy carbon
mV/s – millivolts per second
eV – electron volts
BE – binding energy
KE – kinetic energy
rpm – revolutions per minute
ppm – parts per million
 Φ – work function of the XPS system
XRD – x-ray diffraction
TEM – transmission electron microscopy
STEM – scanning transmission electron microscopy
EDS – energy dispersive spectroscopy
SEM – scanning electron microscopy
AGM – alternating gradient magnetometry
CV – cyclic voltammetry
FEG – field emission gun
DI – deionized water

ACKNOWLEDGEMENTS

I am pleased to have the opportunity to thank the many colleagues, friends, family and faculty members who have helped me with this research project. I would like to give a special thanks to John Wiest, the chairman of this dissertation, for sharing research experience, support, guidance, and motivation throughout my graduate school career. Also, I am most indebted to Dave Nikles, who served as my co-advisor, for valuable insight and providing me with the opportunity for a challenging dissertation topic. I would like to thank the rest of my committee members, Tonya Klein, Alan Lane, and Greg Thompson for invaluable input, inspiring questions, and the support of both my dissertation and my academic growth. I would also like to thank my colleagues Shishou Kang and Chandan Srivastava for technical support in my research. Thanks to INSIC and the MINT center at the University of Alabama for providing funding for my research.

I want to express my deepest gratitude for the encouragement and support from my wife, parents, grandparents, and friends. A special thanks to my lovely bride, Jaime, for all her love, support, and inspiration. Finally, I would like to thank the department of chemical and biological engineering at the University of Alabama for giving me the opportunity to achieve my doctorate degree.

“If you believe in yourself and have dedication, pride, and never quit, you will be a winner. The price of victory is high but so are the rewards.” Paul “Bear” Bryant

“Emancipate yourself from mental slavery; none but ourselves can free our mind.”
Redemption Song, Bob Marley

CONTENTS

ABSTRACT.....	ii
LIST OF ABBREVIATIONS AND SYMBOLS.....	iv
ACKNOWLEDGEMENTS.....	ix
LIST OF TABLES.....	xiii
LIST OF FIGURES.....	xiv
LIST OF ILLUSTRATIONS.....	xx
CHAPTER 1 INTRODUCTION.....	1
1.1 Recording Media Technology.....	3
1.2 Aluminum Manganese Binary System.....	12
1.3 Nanoscale Magnetism.....	26
1.4 Metal Nanoparticle Systems.....	32
1.5 Dissertation Objectives.....	41
CHAPTER 2 EXPERIMENTAL METHODS.....	43
2.1 Chemicals and Materials.....	43
2.2 Synthetic Procedures.....	45
2.2.1 Standard Isolation and Purification Technique.....	49

2.2.2	Phase Transfer Isolation and Purification Technique.....	50
2.2.3	Isolation and Purification Technique from MnPt and MnO Reactions.....	52
2.3	Characterization Techniques.....	53
2.3.1	X-ray Diffraction (XRD).....	53
2.3.2	Transmission Electron Microscopy (TEM).....	57
2.3.3	Energy Dispersive Spectroscopy (EDS).....	61
2.3.4	Alternating Gradient Magnetometer (AGM).....	63
2.3.5	Cyclic Voltammetry (CV).....	66
2.3.6	X-ray Photoelectron Spectroscopy (XPS).....	69
CHAPTER 3 RESULTS AND DISCUSSION.....		71
3.1	FePt and MnPt Syntheses.....	72
3.2	Reduction Potentials using Cyclic Voltammetry (CV).....	80
3.3	AlMn Synthesis Attempts using Superhydride.....	87
3.4	AlMn Synthesis Attempts using Potassium (K).....	92
3.5	AlMn Synthesis Attempts using Hydrogen (H ₂).....	94
3.6	AlMn Synthesis Attempts using LiAlH ₄	100
3.7	AlMn Synthesis Attempts using Sodium (Na).....	110

3.8	AlMn(X) Tertiary Nanoparticle Syntheses.....	145
3.9	Core-Shell Structure AlMn Nanoparticle Syntheses.....	154
CHAPTER 4 CONCLUSIONS AND FUTURE WORK.....		162
APPENDIX.....		166
REFERENCES.....		168

LIST OF TABLES

1.1	Stable phases in the AlMn system.....	16
2.1	Metal precursors and solvents used in synthesis attempts.....	44
2.2	Reducing agents and surfactants used in synthesis attempts.....	45
2.3	Calculated d-spacings from the hexagonal ϵ phase.....	56
2.4	Calculated d-spacings from the tetragonal τ phase.....	56
2.5	Standard reduction potentials.....	67

LIST OF FIGURES

1.1	Cross section of magnetic tape.....	3
1.2	Magnetic tape storage roadmap.....	9
1.3	The binary AlMn system phase diagram.....	15
1.4	Important parameters of a magnetic hysteresis loop.....	28
1.5	Coercivity as a function of particle size.....	29
1.6	FePt phase diagram.....	33
2.1	Picture of an AlMn reactor setup.....	48
2.2	Flow chart of an AlMn nanoparticle synthesis.....	48
2.3	Picture of the AGM used in this research.....	65
3.1	TEM image and electron diffraction pattern of FePt nanoparticles.....	75
3.2	High resolution TEM image, histogram, and fourier transform of FePt nanoparticles.....	76
3.3	XRD spectrum of FePt nanoparticles as made and annealed at 600°C.....	76

3.4	XRD spectrum of as made MnPt ₃ nanoparticles.....	78
3.5	TEM image of MnPt ₃ nanoparticles.....	79
3.6	TEM image with histogram of MnPt ₃ nanoparticles.....	79
3.7	Graph to determine the potential window of diphenyl ether.....	83
3.8	Graph of CV analysis of Al(acac) ₃ in diphenyl ether.....	84
3.9	Graph of CV analysis of Mn(acac) ₂ in diphenyl ether.....	84
3.10	Graph of CV analysis of Pt(acac) ₂ in diphenyl ether.....	85
3.11	Graph of CV analysis of Fe(acac) ₂ in diphenyl ether.....	86
3.12	XRD spectrum from an AlMn synthesis using superhydride.....	89
3.13	XPS survey scan of the particles generated from an AlMn synthesis using superhydride.....	90
3.14	High resolution XPS scan of Al 2p and the peaks indicate the presence of Al ₂ O ₃	90
3.15	High resolution XPS scan of Mn 2p and the peaks indicate the presence of various Mn oxide states.....	91

3.16	XRD spectrum of the precursor sample before heat treatment.....	97
3.17	XRD spectrum of the sample after heat treatment in the tube furnace.....	98
3.18	XRD spectrum from particles obtained from an AlMn synthesis using LiAlH ₄	103
3.19	XRD spectrum from the sediment obtained from an AlMn synthesis using LiAlH ₄	104
3.20	TEM images of Mn ₂ O ₃ particles produced from the synthesis using LiAlH ₄	104
3.21	XRD spectrum from the particles generated from an AlMn reaction using LiAlH ₄	108
3.22	XRD spectrum of the sediment from an AlMn reaction using LiAlH ₄	108
3.23	XRD spectrum of the particles from an AlMn synthesis using Na as made and annealed at 500°C.....	113
3.24	TEM images from an AlMn synthesis using Na.....	114
3.25	XRD spectrums of the particles as made and annealed at 400°C.....	116
3.26	TEM image of particles from an AlMn synthesis using Na.....	116

3.27	High resolution TEM image with histogram and d-spacing.....	117
3.28	XRD spectrums of the sample as made and annealed at 950°C.....	120
3.29	High resolution TEM image with histogram and d-spacing.....	120
3.30	Hysteresis loops of particles as made and annealed at 950°C.....	121
3.31	Graph of remnant coercivity as a function of time at field and plotted with Sharrock's equation to provide KV/kT.....	122
3.32	TEM image of the sediment from the AlMn synthesis.....	125
3.33	High resolution TEM image of the sediment with histogram and d-spacing.....	126
3.34	XRD spectrum of the sediment before the phase transfer technique.....	128
3.35	TEM image from the particles after the phase transfer technique.....	129
3.36	High resolution TEM image with histogram and d-spacing of the particles after the phase transfer technique.....	129
3.37	XRD spectrum of the particles after the phase transfer procedure.....	130
3.38	XRD spectrum of the sediment of the AlMn reaction using Na.....	135

3.39	TEM images of the sediment generated from the AlMn synthesis using Na.....	136
3.40	High resolution TEM image with histogram and d-spacing.....	136
3.41	XRD spectrum from the redispersed particles from the AlMn synthesis.....	137
3.42	TEM images of the redispersed particles from the AlMn synthesis using Na....	139
3.43	Hysteresis loop from the as made redispersed particles.....	140
3.44	High resolution TEM images with histograms and d-spacings.....	141
3.45	Single particle STEM-EDS of the redispersed particles from the AlMn synthesis.....	143
3.46	Electron diffraction pattern of the redispersed particles taken on the TEM.....	144
3.47	TEM images of the redispersed cubic particles.....	144
3.48	XRD spectrum of the as made AlMnCu synthesis.....	149
3.49	XRD spectrum of the as made AlMnPt synthesis.....	151
3.50	XRD spectrum of an as made AlMnPt synthesis.....	153

3.51	TEM images from an AlMnPt synthesis.....	153
3.52	XRD spectrum of particles from a synthesis attempt of core-shell AlMn nanoparticles.....	157
3.53	XRD spectrum of particles from a synthesis attempt of core-shell AlMn nanoparticles.....	159

LIST OF ILLUSTRATIONS

2.1	AlMn reaction setup.....	47
2.2	Schematic of XRD and Bragg's Law.....	54
2.3	Schematic diagram of TEM components.....	59
2.4	Diagram of the principle of EDS.....	62
2.5	Spectrum of possible x-rays generated from an element.....	63
2.6	Schematic of the AGM and sample holder.....	66
3.1	Schematic of the tube furnace reactor setup.....	99

CHAPTER 1

INTRODUCTION

As the information age progresses, the demand for high performance, low cost, and nonvolatile information storage systems increases at a fast rate. There are a variety of information storage systems including magnetic tape drives, hard disks, floppy disk drives, optic disk drives, flash memory, magnetic random access memory (MRAM), and holographic optical storage. This research is focused on one of the most widely used of these storage systems, magnetic tape. An important characteristic of magnetic tape's storage capacity and performance is the magnetic layer, and the magnetic nanoparticles that encompass this layer. To achieve better performance and increased storage capacity, inexpensive small particles with large anisotropy values are required. Today's commercial tapes use acicular metal particles (MP), but they are rapidly reaching their limit to meet the storage demands. As a result, there is a need for new particle developments with characteristics that include small size and suitable magnetic properties needed for high density recording. Over the past decade, nanoparticles with sizes ranging from 2-10 nm have been produced from a class of metal alloys that have a tetragonal $L1_0$ phase that exhibits uniaxial magnetocrystalline anisotropy in the range of $K = 10^7$ erg/cc³ with an "easy" c-axis. These nanoparticles are subjected to heat treatments to transform to the $L1_0$ phase which has attractive magnetic properties. The family of magnetic alloys includes the CoPt, FePt, FePd, AlMn, and other binary systems. Nanoparticle systems of

CoPt, FePt, and FePd have been studied extensively over the last several years for magnetic recording purpose, but the expensive materials required to produce these particles are a deterrent for large scale commercial production. AlMn permanent magnetic materials have received attention from a commercial point of view over the past three decades because of good magnetic properties and a low cost of raw materials. The research of the AlMn system has been limited to bulk alloys and thin films with no reports of AlMn nanoparticles.

This research investigates the opportunity to create a method to develop a process to produce ferromagnetic AlMn nanoparticles. AlMn nanoparticles could be established as the next generation of particulate media used in magnetic recording devices such as magnetic tape. With little guidance to follow or strategy for the production of AlMn nanoparticles, it is crucial to use several different angles in literature searches to develop a research plan. The areas of exploration to formulate a development method for AlMn nanoparticles includes the early characterization and production methods of bulk alloys, derive a fundamental knowledge of magnetism, and learn general characteristics of well known systems of transition metal nanoparticles such as FePt and CoPt. Incorporating knowledge from each of these topics can help formulate a research plan for synthesis development, along with other procedures and techniques to be successful in this endeavor. First, recording media technology is discussed including background on magnetic tape, INSIC's tape roadmap, and particle candidates that can potentially be used in future tapes. Then, the AlMn binary system is discussed at length including the

ferromagnetic τ phase. Subsequently, a brief synopsis on nanoscale magnetism and how it relates to the recording industry is mentioned. Next, general metal nanoparticle characteristics and production methods are reviewed. Finally, the specific objectives of this dissertation research are stated.

1.1 Recording Media Technology

Magnetic tape is one of the oldest computer storage technologies and serves the demand for information storage applications very well due to its high capacity, reliability, and competitive pricing.[1] During the computer era, a new need arose for rapid access to stored data. Particulate recording tape continues to be the dominant tape medium, with many refinements over the past several decades. Figure 1.1 shows a schematic cross section of magnetic tape.

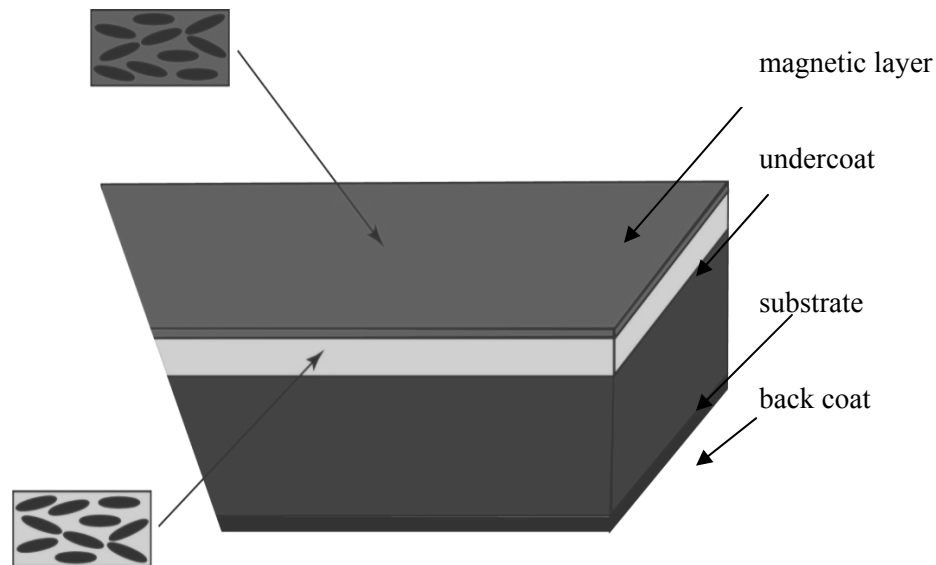


Figure 1.1 Cross section of magnetic tape

Generally, magnetic tape consists of four layers. The first layer is a magnetic layer typically 50-100 nm thick. The most essential aspect of this layer is the magnetic particles. The first magnetic tapes were made with large iron oxide particles more than 1 μm in diameter.[1] The particle sizes have been dramatically decreased throughout the years with the volume in the magnetic layer increased, which directly correlates to higher storage capacity. Today, commercial tapes utilize acicular metal particulate composites (MP) which are typically an iron/cobalt alloy.[2] This research focuses on the particles used in the magnetic layer. To form this magnetic layer, the particles are well dispersed in a polymeric binder, together with solvents, dispersants, lubricants, antistatic agents, and, if necessary, fillers to help resist mechanical wear. The binder is expected to have high flexibility, high elasticity, high wear resistance, and low friction on metal or plastic surfaces. The binder is typically cross-linked polymers because it is necessary for the binder to have contradictory requirements. For example, polymers of low molecular weight give smoother dispersions, but are less wear resistant and have higher friction values. Some examples of these polymers are as follows: copolymers of vinyl chlorides, copolymers of vinylidene chloride, polyvinyl formal, polyvinyl acetate resins, acrylate and methacrylate resins, soluble polyurethane elastomers, modified cellulose derivatives, epoxy and phenoxy resins, and polyamides.[3] The solvent selected for the dispersion must be compatible with the binder system which means it must hold the solubles in solution and maintain the magnetic particle dispersion. The solvent should also be reasonably fast drying. Some examples of these solvents are as follows: methyl ethyl

ketone, methyl isobutyl ketone, cyclohexanone, tetrahydrofuran (THF), dioxane, n-methyl pyrrolidone, n-dimethyl formamide (DMF), and toluene.[3] In order to achieve a stable dispersion, it is necessary to prevent agglomeration and sedimentation.

Agglomeration is partially avoided due to the organic polymer binder molecules. In addition, active dispersants of low molecular weight with hydrophilic and hydrophobic groups are used. All dispersants must be carefully selected and their amount chosen with respect to the surface chemistry of the particles and binder system. Lubricants, such as silicon oils, fatty acids, or hydrocarbons, are added to assure good tape life. The idea for adding a lubricant is that it forms a monolayer on the surface of the magnetic coating and helps prevent friction from the recording process. Nonmagnetic fillers like silicic acid, alumina, or chromium trioxide are often added to improve the wear resistance and frictional properties of the magnetic coating.[3]

The next layer is the undercoat which is approximately 1 μm thick and provides physical support to the magnetic layer.

Standard substrate material for particulate recording media is a biaxially oriented polyethylene terephthalate (polyester) film on the order of 6 μm thick. Important properties of the polyester films are their surface smoothness and resistance to wear. Having these properties helps avoid defects in the final magnetic coating. Defects can cause local signal reductions and can jeopardize the performance of the tape. The substrates main purpose is to give mechanical stability to the magnetic layer during the

wear and tear generated from winding and unwinding during the recording and reading process.[3]

The back coat consists of carbon black in a urethane binder and is approximately 500 nm thick. This urethane binder acts as an anti-static agent. The carbon black increases the conductivity of the tape and allows static electric charges to be dissipated.

Magnetic tape is manufactured by a double slot-die coating process where a magnetic dispersion and a non-magnetic underlayer are simultaneously cast onto a polymer base film. Immediately after coating, before drying occurs, the films are placed into a magnetic field to align the acicular particles parallel to the machine direction of the tape. The drying process is done under a stream of hot air generated in an oven. This web leaves the oven and is wound onto a reel and kept for a period of time. The dried magnetic coating usually is not completely solid; it has a compressible sponge-like structure. Consequently, the dried web is passed through several calendaring steel rolls to compact the coating and smooth the surface of the magnetic coating. This calendared tape is placed in a curing room where the temperature and humidity are controlled for a period of a few hours (often overnight). Finally, the cured, calendared tape is slit to the proper width and wound onto a reel for packaging.[3] During the coating process the particles are aligned by a field so that their long axes tend to be parallel with the length of the tape. This is done in order to make the remnance, which occurs after magnetization is removed, in the direction of the length of the tape, as large as possible.[4]

Recording information onto a tape goes through a process of writing the data on the tape and then reading the data for playback. Generally, during recording and playback regions of the tape are magnetized in one direction or the other to the same extent. To record information, current pulses are fed to the winding on the recording head core. Each pulse magnetizes the core, thus creating a field in the air gap. As the moving tape passes the gap, the fringing field of the gap magnetizes the tape. Not all this magnetization is retained, as this particular section of tape leaves the gap area, but a certain remnant portion is retained and this portion constitutes the recording.[1, 4] Data is written in binary code as either a 0 or 1 on the tape.[1] Reading the tape depends on the ability of the playback head to sense the exterior field created by the magnetization of each section of tape. When a 1 is below the gap, the field at the tape surface prefers the low-reluctance path through the high permeability core to the air-gap path, and the flux in the core is counterclockwise. When a 0 is below the gap, the flux is reversed to clockwise. Therefore, as the tape moves past the gap, the transition from a 1 to a 0 will reverse the flux in the playback core and induce a voltage pulse in its winding.[4] The key issue in digital recording is to get as much information into each inch of tape as possible. High density recording requires high remnance, high coercivity, and small coating thickness.[1] All of these parameters have a direct correlation to the magnetic particles encompassed in the magnetic layer.

The Information Storage Industry Consortium (INSIC) assembled a roadmap that predicted future goals for tape storage capacity to meet with future storage demands. In

2007, tape capacity reached approximately 1 Tb with an areal density close to 0.7 Gb/in². [5] The demand for increased storage capacity increases at a rate of about 42% per year. Over the next decade, INSIC predicts that tape capacity will double every two years and be at 32 Tb with an areal density of about 16.86 Gb/in² in 2018. [5] Figure 1.2 shows a graph of the magnetic tape storage roadmap produced by INSIC through 2011. To meet such storage capacity goals all areas of recording must be improved. Magnetic media volumetric information density has three dimensions, each of which must be optimized to achieve the expected increase in tape capacity and performance. These three dimensions are linear density, track density, and layer density (the inverse of tape thickness). [5] New developments in the next five to ten years will be required to improve these parameters to achieve lofty future demands. For this research, the focus is on magnetic materials, particularly magnetic particles, used for advanced recording tapes to help meet these future storage goals.

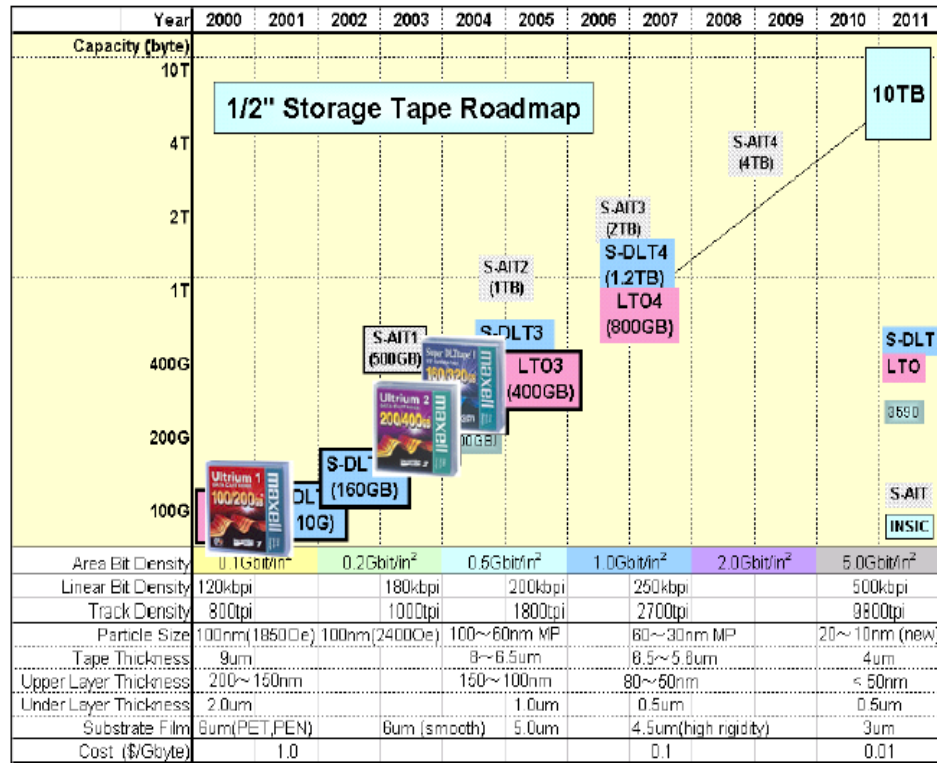


Figure 1.2 Magnetic Tape Storage Roadmap[5]

The magnetic materials under consideration for advanced recording tapes at this time are primarily acicular metal particles (MP) and metal evaporated (ME) films. This research is focused on new developments in particulate media for use in tapes. Particles used for tape must follow some general criteria such as having good magnetic properties (coercivity and magnetization), inexpensive production methods, and small sizes under 20 nm. MP are the most widely used particles in tapes today but other particles such as hexagonal ferrites (barium ferrite), iron nitride, FePt, and CoPt have been researched as candidates for future particulate media to meet the needs of ever increasing storage

capacity. Also, AlMn particles have emerged as a candidate, but no research efforts have been able to produce these particles.

MP materials are the most commonly used recording material in data tapes.[5] Development is in the direction of smaller particle size, with retention of as much of the magnetic properties as possible from the older materials. The magnetic material in MP is typically an iron-cobalt alloy surrounded by a passivation shell formed by controlled oxidation to protect the core against corrosion. This passivation layer is non-magnetic and typically a few nm thick.[2, 5] As particles become smaller, this shell becomes a larger portion of the total volume, exceeding 50% in advanced MP at present. The coercivity in the MP comes from shape anisotropy of the acicular particles.[2] The trend for increasing tape performance is making small particle size the highest priority, because the media-limited signal to noise ratio depends upon the number of particles per unit volume.[5] MP's are coming to the limit in decreased particle size due to their acicular shape reaching its thermal limitations. As the particle size is decreased, the volume of magnetic material is decreased. This trend to smaller size will ultimately be limited by insufficient thermal magnetic stability of MP.[2] The problems encountered in the effort to make smaller particles are: broader distribution of particle size, sintering, aggregates, and decreasing core volume. Because of these problems, magnetic properties, stability, and dispersibility become significantly worse.[5] All these issues make new particle developments a high priority for the recording industry.

One candidate for use in future tapes is barium ferrite. Barium ferrite is a stable oxide, so a passivation layer is not required, but its magnetization is much lower than other materials because it is an oxide. Barium ferrite offers very small, compact particles and potentially high coercivity. The combination of small size and low magnetization, creates a relatively low level of thermal stability.[1, 5] However, barium ferrite tape media have been used to demonstrate areal densities up to 17.5 Gb/in² using a single-channel system and a very narrow GMR head and also 6.7 Gb/in² in a multi-channel tape system.[6-8] One initial concern of using barium ferrites was their relatively low magnetization, but with the advent of increasingly sensitive heads (GMR and TMR) it should not be a deterrent.[5]

Spherical iron nitride (NanoCAP) particles are another candidate for future storage tapes. Iron nitride particles can have substantial coercivities of about 3500 oersteds (Oe) without the need for needle-like shape because of their crystalline structure which exhibits crystalline anisotropy. Iron nitride particles have an average particle size of 17 nm but they have a broad size range distribution.[9] The challenges of providing small, uniform particle size are similar to those in MP.[5] FePt and CoPt are transition metal nanoparticle systems that have gained much attention over the past decade due to their good magnetic properties. They exhibit a ferromagnetic, tetragonal L1₀ phase characterized by a high anisotropy constant, but the high cost of Pt is a deterrent for use in tape.[5, 10-12] AlMn has an L1₀ phase similar to FePt and CoPt with suitable magnetic properties for recording purposes. Because of these issues with particulate

media candidates, research into new magnetic particles with small size, good magnetic properties and inexpensive precursors is needed. AlMn nanoparticles could emerge as the leading candidate for use in magnetic tape due to its attractive magnetic properties, wide availability, and the low cost of raw materials.

As the trend toward smaller particles continues, particulate media used in tape will not be able to continue to use particles with shape anisotropy to meet storage capacity needs past the near future. Acicular MP lose their magnetic properties when the particle size is decreased. Aspect ratio is the proportion of the particles length to its width and it is associated with shape anisotropy values. Also with acicular particles, as the size decreases the amount of nonmagnetic material in the passivation layer increases compared to the amount of magnetic material. Acicular MP can only be decreased in size to the range of 30-40 nm before the magnetic properties are such that they are not suitable for magnetic tape.[1, 2, 5] Therefore, new particle development for use in magnetic tape will have to utilize particles with crystalline anisotropy to achieve small particle size and still maintain good magnetic properties. This reiterates the idea of developing a technique to synthesize AlMn nanoparticles for use in magnetic tape.

1.2 Aluminum Manganese Binary System

In the binary aluminum manganese (AlMn) system, a ferromagnetic phase exists between 49-60 at % Mn.[13-17] This phase is a metastable, tetragonal $L1_0$ superstructure similar to the phase of other binary systems such as FePt and CoPt.[13, 14]

It possesses a large magnetocrystalline anisotropy constant (K) around 10^7 erg/cc.[14]

This ferromagnetic phase in the AlMn system is labeled as the τ phase. The τ phase exhibits good magnetic properties including large coercivity and saturation magnetization which makes it an attractive candidate for magnetic recording applications. Because of the τ phase and its possible uses in recording, the AlMn system has been studied quite extensively. Most studies have been metallurgical investigations on bulk alloys, or sputtered thin films of AlMn. No studies into nanoparticle syntheses or wet chemical syntheses are known. It is of importance to combine knowledge of all known production methods and mechanisms of transformation to the τ phase to help develop nanoparticle synthesis techniques. In this section, the ferromagnetic τ phase of AlMn is presented on a chronological timeline from the preliminary research investigations that characterized the τ phase to the most recent investigations. Most initial studies into this phase and the mechanisms of τ phase formation were done on bulk alloys. The unique contributions of each investigation are presented to give the entire scope of knowledge on the ferromagnetic τ phase of AlMn. Next, the details into the formation mechanism of the τ phase are discussed. Then, an explanation of the origin of anisotropy of this phase is given from experimental results. Finally, other ferromagnetic AlMn production methods are given including thin films and several others. All of this knowledge from many research endeavors into the τ phase can be coupled together to help create a solution phase synthesis technique to produce AlMn nanoparticles.

The existence of a ferromagnetic phase in the AlMn binary system was first discovered by Hindricks in 1908[18], and later studied by Ishiwara et al. and Koster et al. in 1926 and 1938, respectively.[19, 20] The first extensive investigation into the structure and characteristics of the ferromagnetic phase of AlMn was done by Hiroshi Kono in 1958 on bulk alloys in the compositional range of 47-60 at % Mn.[13] He discovered a new hexagonal close packed (hcp) phase and a metastable tetragonal ferromagnetic phase. He recognized that this hcp phase was the parent or precursor phase of the ferromagnetic tetragonal τ phase. The discovery of two eutectoid regions in the AlMn system at 840°C and 870°C lead him to subject his specimens to a heat treatment at 950°C for 1 hour followed by quenching in water. The results of this experiment yielded the hcp structure called the ϵ phase. The lattice parameters of this phase were $a = 2.69\text{\AA}$ and $c = 4.38\text{\AA}$, and this phase was found to be non-magnetic.[13] Further studies indicated that the hcp ϵ phase is antiferromagnetic.[21] This ϵ phase was subsequently annealed at various temperatures between 400-650°C. After annealing, a ferromagnetic phase had been yielded. This phase was characterized as a metastable tetragonal $L1_0$ superstructure (similar to CuAu type), and labeled as the τ phase with lattice constants of $a = 3.94\text{\AA}$ and $c = 3.58\text{\AA}$.[13]

McAllister and Murray produced the first phase diagram in 1987 of this system but did not include the ferromagnetic τ phase on the diagram because it is metastable.[29] Thermodynamic studies done by Jansson and Liu both follow the phase diagram presented by McAllister and Murray, and they also do not report information on the τ

phase.[30, 31] The τ phase was included by Yanar et al. during their study of AlMn alloys. Figure 1.3 shows the AlMn binary system phase diagram from Yanar et al.[26]

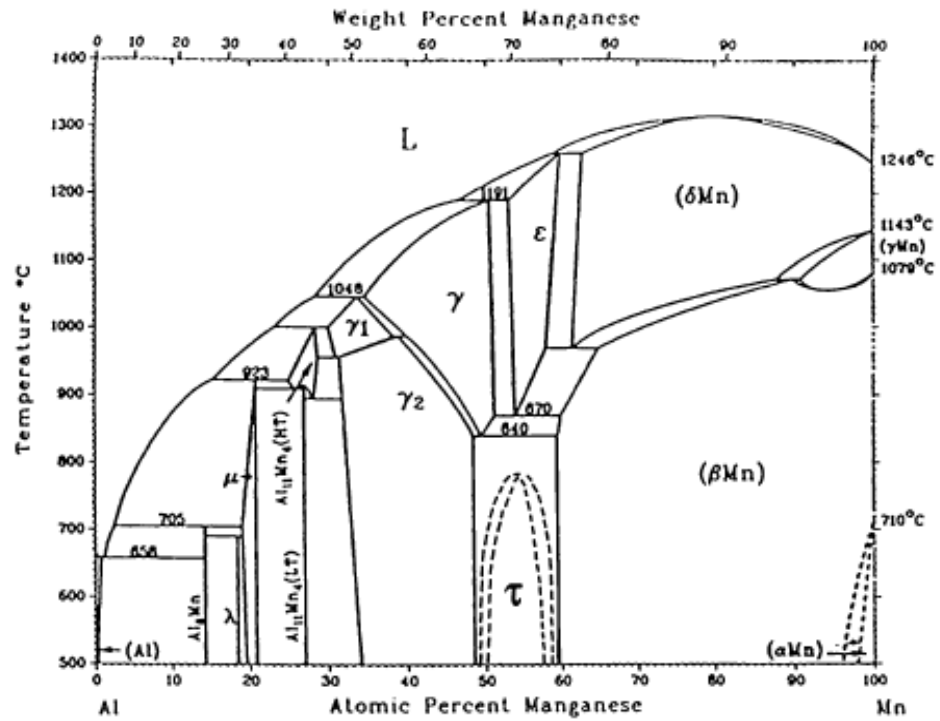


Figure 1.3 The binary AlMn system phase diagram[26]

Stable Phases in the AlMn system		
Phase	Composition at.% Mn	Modeling phase
Al	0-0.62	fcc
Al12Mn	7.7	Al12Mn
Al6Mn	14.2	Al6Mn
λ	16.8-19	Al4Mn
μ	19-20.8	Al4Mn
Al11Mn4 (higher temperature)	27	Al11Mn4
Al11Mn4 (lower temperature)	25-28.7	Al11Mn4
γ_1	30-38.7	Al8Mn5
γ_2	31.4-50	Al8Mn5
γ	34.5-52	bcc
ε	53.2-72	cph
δ Mn	71-100	bcc
γ Mn	90.9-100	fcc
β Mn	59.5-100	β Mn
α Mn	98-100	α Mn

Table 1.1 Stable phases in the AlMn system[26]

Table 1.1 illustrates the structure, compositional range in at %, and stoichiometry of all the stable phases that occur in the binary AlMn system. The metastable τ phase is not listed but it is a tetragonal $L1_0$ (CuAu) structure and the only magnetic phase of AlMn.[26]

Kono also found another route that obtained this ferromagnetic phase. He noticed that cooling rates from the ε phase had an effect on magnetic properties. It was determined that the τ phase could also be produced by cooling the hcp ε phase to room temperature at about 10°C/s without any further heat treatment. The τ phase was

ferromagnetic and Kono measured the magnetic properties including coercivities (H_c) around 4500 Oe and saturation magnetization (M_s) around 100 emu/cc. The Curie point (temperature above which a substance is no longer ferromagnetic) of the τ phase was approximately 380°C.[13] The τ phase had a layer structure: each $\{011\}$ net plane contained mainly Mn or Al atoms respectively, stacking alternatively in $\{001\}$ direction of the crystal. There were a few Mn atoms in an Al layer. The nearest neighboring pair of Mn atoms in two adjacent layers had the distance of 2.66Å, while that in a Mn layer has the distance of 2.79Å. According to the Bethe-Slater curve representing the relationship between the exchange energy of magnetization and the interatomic distance, the exchange coupling between 3d electrons of adjacent Mn atoms changes from antiferromagnetic to ferromagnetic at the interatomic distance of about 2.57Å. The distances between Mn atoms in the τ phase crystal were greater than this critical value, so the occurrence of ferromagnetism in this alloy was compatible with this prediction.[13] In 1960, Koch et al. investigated the MnAl system from 40-100 at % Mn.

Koch obtained the τ phase using similar methods used by Kono. He reported the ϵ phase also with a hexagonal structure with lattice constants of $a = 2.68\text{\AA}$ and $c = 4.34\text{\AA}$, which was consistent with Kono's study. Koch cooled the ϵ phase from 1150°C to below 700°C at a rate of approximately 30°C/s to transform it to the tetragonal τ phase with lattice parameters of $a = 2.77\text{\AA}$ and $c = 3.57\text{\AA}$. The magnetic properties observed were remarkable with coercivities around 6200 Oe and an anisotropy constant (K) of about 10^7 erg/cc.[14] The difference in the lattice constant values reported by Kono and Koch

remained unexplained for many years in the literature and served as a major problem for characterization of the τ phase in subsequent studies.

In 1963, an x-ray diffraction investigation into the magnetic τ phase of AlMn was conducted. Koch's experimental methods were used to obtain the τ phase. From x-ray powder diffraction data the τ phase had a tetragonal unit cell with $a = 2.77\text{\AA}$ and $c = 3.54\text{\AA}$. The systematic appearance of strong reflections when the sum of the indices was even and weak reflections when it was odd proved a difference in scattering power at $\{000\}$ and $\{1/2, 1/2, 1/2\}$ which indicated the τ phase was an ordered structure.[15] In 1966, Kamino et al. investigated the magnetic properties of the MnAl system alloys. Kamino experimentally prepared single crystals of MnAl and alloys of MnAl containing about 2% boron by zone melting. The magnetic properties of the MnAl alloys were similar to previous work by Koch with coercivities around 6900 Oe and an anisotropy constant of about 9.3×10^6 erg/cc. What he also found was that the alloys doped with boron also had good magnetic properties, but the boron helped stabilize the alloy.[16]

This discovery of adding small amounts of another element to the AlMn system for stabilization influenced many research experiments on AlMn alloys and AlMn thin films. By adding a small amount of additive to the AlMn alloy, production was easier, and the alloys and films were much more stable. In 1993, Stafford et al. conducted an investigation into electrodeposition of ferromagnetic AlMn, but more importantly a possible explanation for the differences in lattice constants was given. The theory was

that both sets of lattice constants could be correct. Koch's report of lattice constants of $a = 2.78\text{\AA}$ and $c = 3.57\text{\AA}$ was designated as a metastable tetragonal phase (tP2), while it was suggested that this phase could also be described as a distorted face centered cubic structure (CuAu type, $L1_0$) with lattice parameters of $a = 3.94\text{\AA}$ and $c = 3.58\text{\AA}$ like the ones reported by Kono.[22] These research investigations set the foundation for all that followed with production methods and general characterization of the τ phase in the AlMn binary system.

The mechanism of formation of the τ phase has been studied extensively throughout the literature. Kojima et al. began the investigation into the transformation mechanism to the τ phase in the AlMn system in 1974, but the first extensive study came in 1979 with Van den Broek and Donkersloot. Their studies into the phase transformation used pure $\text{Al}_{45}\text{Mn}_{55}$ alloys and carbon doped AlMn alloys. Transmission electron microscopy and diffraction techniques were used to observe various phase transformations in this system. From Kono's work, two methods of obtaining the τ phase existed either by cooling the hcp ϵ phase at a rate on the order of $30^\circ\text{C}/\text{min}$, or by quenching the high temperature ϵ phase followed by a heat treatment below 600°C . The first method points to a cooperative type of transformation. The mechanism underlying this transformation was found to shear on close packed planes as proposed on the basis of x-ray and neutron diffraction studies.[23, 24] Van den Broek et al. studied the second method of obtaining the τ phase to explore the mechanism of formation. They found the mechanism to be the same for binary AlMn as well as alloys doped with small amounts

of carbon. During the quenching phase, the hcp ϵ phase underwent an ordering reaction to obtain an orthorhombic (B19) structure. During the annealing procedures in the temperature range of 400-600°C the orthorhombic structure underwent a martensitic shear transition to achieve the tetragonal $L1_0$ structured τ phase. Inside the ordered domains of the orthorhombic structure, stacking faults provide the shear system required for the transformation from hexagonal to tetragonal structure.[17]

In 1996, experimental evidence disputed the conventional wisdom that the ferromagnetic τ phase formed via a martensitic shear transformation following B19 ordering of the ϵ phase. This study was done on carbon doped alloys ($Mn_{54.3}Al_{44}C_{1.7}$) with typical heat treatments to obtain the τ phase. Electron microscopy showed evidence that the $\epsilon \rightarrow \tau$ transformation involves a diffusional nucleation and growth process referred to as a “massive” transformation in metallurgical literature rather than via a shear mechanism.[25] Another investigation in 2002 reinforced this type of mechanism. This study was also done on AlMn bulk alloys. The τ phase was derived from the high temperature ϵ phase (hcp) upon cooling from the ϵ phase field and during isothermal aging after quenching to obtain the ϵ' phase (orthorhombic) at room temperature. This investigation indicated the formation of the τ phase involved a compositionally invariant, diffusional nucleation and growth process preferentially forming at the grain boundaries of the ϵ phase. The mechanism is characterized by a massive transformation or “massive ordering” which nucleates almost exclusively at the grain boundaries during cooling or isothermal aging within the two phase fields of the equilibrium phase diagram.[26] Also

this study reinforces the idea that the τ phase can form in two distinct manners. The $\epsilon \rightarrow \epsilon'$ ordering transformation has been revealed as a competitive metastable ordering transformation occurring below 580°C, therefore at high temperatures the τ phase can form without prior $\epsilon(\text{hcp}) \rightarrow \epsilon'(\text{B19})$ ordering.[26]

Also in 2002, an investigation by Mullner et al. into the $\epsilon \rightarrow \tau$ transformation was done using single crystal AlMn samples. This study found that this transformation actually occurred by different mechanisms depending on the microstructure and purity of the ϵ phase. It depended on the thermal treatment if the intermediate phase, the B19 ordered orthorhombic ϵ' phase, was involved. At elevated temperatures and in polycrystalline specimens a massive transformation took place with nucleation on grain boundaries which supports the previous investigations. On the other hand, at low temperatures and in single crystals of AlMn, a shear mechanism was active.[27] In the massive transformation the ϵ' phase does not take part in the transformation, whereas it plays a key role in the shear transformation mode. Mullner discovered the following sequence of events during the shear mechanism transformation. First, during the initial heat treatment the hexagonal disordered ϵ phase formed. The transformation started when the sample is quenched and coherent nucleation of ϵ' occurred. Then, the second step was a shear reaction to form the τ phase. It was not a purely martensitic (i.e. athermal) transformation, it also involved a reordering component which was thermally activated (by the final heat treatment). This reordering along one of the close packed directions of the ϵ' broke the hexagonal symmetry. A shear on $\epsilon'\{001\}$ along $\epsilon'\{010\}$

produced the final tetragonal lattice of the τ phase.[27] The presence of the orthorhombic B19 structure was necessary for the shear transformation mode. Otherwise, a less stable face centered cubic structure instead of the $L1_0$ structure would form. Also, the presence of three symmetry equivalent ϵ' variants at the beginning of the transformation required reordering during the shear mode operation. Therefore, the transformation was not purely martensitic.[27] The τ phase in AlMn has two distinct routes of formation in bulk samples. The knowledge of these routes and understanding the mechanisms of formation should be beneficial in development of an AlMn nanoparticle synthesis. More importantly, these routes could help to find the suitable annealing conditions to transform the non-magnetic as made nanoparticles to the ferromagnetic τ phase.

The ferromagnetic τ phase in the AlMn system exhibits good magnetic properties with a large anisotropy value. Several studies have explored the origin of anisotropy in the τ phase. This ferromagnetic phase has an ordered tetragonal $L1_0$ structure in which Mn atoms are located at the $\{000\}$ sites and are coupled ferromagnetically.[28] Pareti et al. performed experiments to find the origin of the anisotropy. The anisotropy of the AlMn τ phase is well described by only using the K constant. Also, the anisotropy constant and thus the anisotropy energy do not change by varying the alloy composition in the range of 47-60 at. % Mn. Anisotropy field variations observed during experimentation is attributed to the saturation magnetization behavior. The observed behavior of the anisotropy constant as a function of the temperature indicates that a single

ion mechanism is responsible for the magnetocrystalline anisotropy in the AlMn τ phase.[28]

It is of note that a crucial bit of information regarding the potential oxidation of this AlMn binary system is not reported anywhere in the literature. No prevention methods are discussed to avoid oxidation, and it is not a topic of discussion in any of the literature. For a system containing Al and Mn, where both elements like to exist in an oxidized state, it would seem logical to consider the possibility of oxidation. Also, the ferromagnetic phase of AlMn has been studied extensively in bulk alloys but not on the nanoscale. Bulk properties do not necessarily translate to the nanoscale so it is possible that oxidation must be taken into consideration with AlMn nanoparticles.[4]

Literature provides alternative systems containing ferromagnetic AlMn, but there is no knowledge of nanoparticles of this system. The majority of work done on the ferromagnetic phase of the AlMn system is on bulk alloys, but AlMn thin films have been reported to have achieved the ferromagnetic τ phase characterized by good magnetic properties. In 1987, Morisako and Matsumoto developed AlMn thin films for use in magnetic recording media. Sputtering techniques were used to deposit AlMn as thin films. Since then many studies of sputtered AlMn thin films for recording purposes have followed.[32-39] Morisako and Matsumoto used d.c. magnetron sputtering on a substrate in a high vacuum (5×10^{-7} torr) to produce AlMn films. The targets used were high purity Al (99.99%) and high purity Mn (99.99%). Substrate temperatures varied from

100-170°C for deposition. The deposition temperature followed by an annealing process determined if the τ phase was produced. The films produced by Morisako and Matsumoto exhibited low saturation magnetization around 120 emu/cc, which is only one fourth of the bulk magnetization.[34, 35] This low M_s made those films not applicable for magnetic recording media. In 1995, Huang et al. produced AlMn films containing the τ phase with coercivities up to 3000 Oe and M_s of 420 emu/cc. These films were deposited by means of an r.f. magnetron sputtering system with high purity Al and Mn disks as targets. Films were deposited on glass substrates with substrate temperatures ranging from 30-250°C. The power source operated at 80 W with an average deposition rate of 0.5 nm/s with a base pressure of approximately 5×10^{-7} torr. Thermal annealing was carried out at temperatures between 350-550°C in a vacuum. Films deposited at 30°C and annealed at 410°C with a composition of $Mn_{50}Al_{50}$ showed evidence of the τ phase with good magnetic properties.[32] AlMn thin films consisting of the τ phase could be an attractive candidate for use in metal evaporated (ME) tapes for magnetic recording. Other alternative methods of producing ferromagnetic AlMn systems include melt spinning, electrodeposition techniques, and homogeneous precipitation.[22, 40-42] Nanocrystalline $Mn_{54}Al_{44}C_2$ ribbons were made by melt spinning followed by subsequent heat treatments that yielded the ferromagnetic τ phase. The ribbon alloys were prepared by melt spinning in a single phase of the disordered hexagonal ϵ phase. Then, they were subjected to heat treatments and the highest coercivity was obtained after

annealing at 500°C. Also, the addition of 2 at % C stabilized the τ phase and prevented it from decomposing into the non-magnetic phases of β -Mn and γ -Al₈Mn₅. [43]

Several studies have given detailed synthesis techniques using electrodeposition to produce different phases of AlMn. Some electrodeposition studies produced amorphous AlMn deposits while others produced the ferromagnetic τ phase. Electrodeposition has been used with molten salts in an electrolyte to produce the ferromagnetic τ phase. AlMn was deposited onto copper substrates at temperatures from 150°C to 425°C from a chloroaluminate electrolyte composed of a 55:45 mole ratio of AlCl₃:NaCl containing MnCl₂ with a quartz electrochemical cell. The parameters of temperature and current density were varied but only the Mn content affected the deposited structure. Mn content less than 45 at. % resulted in the non-magnetic cubic Al₈Mn₅ structure while Mn content from 45.1-50 at. % resulted in deposits of the ferromagnetic τ phase in the temperature range between 185°C to 325°C. Hysteresis loops showed the sample had a coercivity around 2 kOe as deposited with no post annealing. [22, 41]

Mn-doped alumina nanoparticles have been synthesized by homogeneous precipitation with urea and the thermal evolution was studied from 60°C to 1500°C. The formation of particles occurred by hydrolysis of inorganic salts based on the thermal instability of some organic alkalis (urea) with the increase of temperature and acidification of the solution. The obtained colloidal solution is highly stable but has a

wide size distribution from 1.5-14 nm with most particles around 2 nm. The thermal evolution showed the particles obtained by this method form non-crystalline amorphous oxides below 600°C. After a heat treatment at 1000°C, cubic spinel $Mn_2Al_2O_4$ particles were obtained.[42] This method produced a wet colloidal synthesis of nanoparticles, but nothing ferromagnetic and not AlMn nanoparticles. Literature provides many ways of producing the ferromagnetic τ phase of AlMn including bulk alloys, sputtered films, electrodeposition, and melt spinning alloys but no knowledge exists of a nanoparticle array of AlMn. The only study that produced nanoparticles obtained oxide forms of Mn and Al, and no studies provided any insight into nanoparticles of AlMn and the ferromagnetic τ phase.

1.3 Nanoscale Magnetism

The ferromagnetic τ phase in the AlMn system possesses good magnetic properties, so fundamentals of magnetism and specifically magnetism in nanostructures are discussed. First, magnetic terms are defined such as the typical components of a hysteresis loop and general terms. There are five basic types of magnetism that have been observed and classified based on magnetic behavior of materials in response to a magnetic field. These types of magnetism are as follows: ferromagnetism, ferrimagnetism, antiferromagnetism, paramagnetism, and diamagnetism. Ferromagnetism and ferrimagnetism occur when the magnetic moments in a magnetic material line up spontaneously at a temperature below its Curie temperature, to produce

net magnetism. The magnetic moments are aligned randomly at temperatures above the Curie point, but are ordered below this temperature. A material that exhibits ferromagnetism has moments of equal magnitude that arrange themselves parallel to each other. In a ferromagnetic material the moments have unequal magnitude and order themselves antiparallel. When the moments are equal in magnitude and ordering occurs at a temperature called the Neel temperature in an antiparallel array to give no net magnetization, it is referred to as antiferromagnetism. Paramagnetism is a weak form of magnetism observed in substances which display a positive response to an applied magnetic field. Diamagnetism is associated with materials that have a negative magnetic susceptibility. It occurs in nonmagnetic substances such as graphite, copper, silver, gold, silicon, and many others.[4, 44] The units for measuring magnetization are emu/cc, and magnetic field strength, H , is measured in Oe. Important parameters for magnetic recording purposes are coercivity (H_c) and saturation magnetization (M_s) as shown in figure 1.4. Coercivity is the amount of field required to switch or reverse the magnetization. Saturation magnetization is the maximum magnetization in a material when fully saturated by an applied field. Magnetic materials exhibit hysteresis, memory of the applied field once it is removed, in the presence of a changing applied field and a typical hysteresis loop and its parameters is shown in figure 1.4.

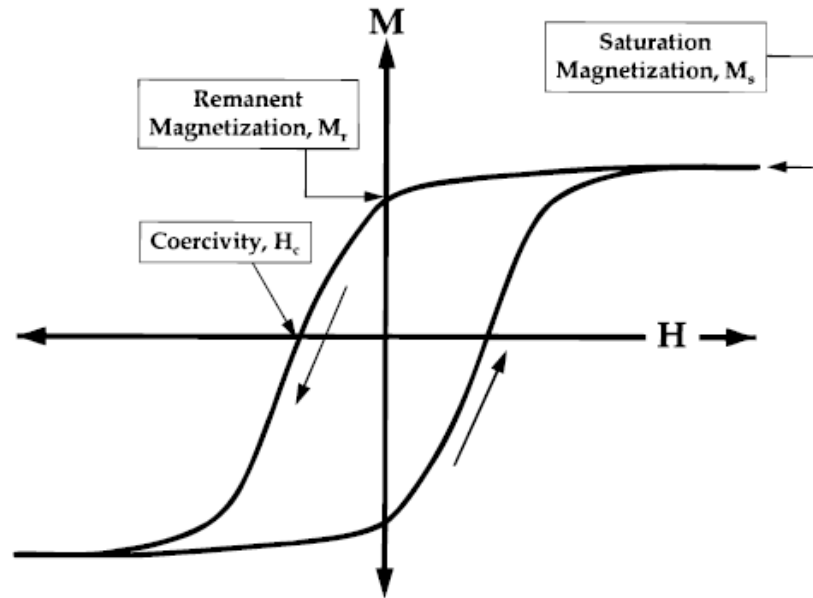


Figure 1.4 Important parameters of a magnetic hysteresis loop[4]

Magnetism in nanoparticles shows structure sensitivity. Among magnetic properties, saturation magnetization is independent of sample size, but coercivity is greatly affected by sample size. Therefore, coercivity can change depending upon the particle's size. The basis of magnetism also changes on the nanoparticle scale. A ferromagnetic material acts as a permanent magnet, and this occurs when all of a materials magnetic moments or spins line up parallel in the same direction .[4] Domains are groups of spins all pointing in the same direction and acting cooperatively. Domains are separated by domain walls, which have a characteristic width and energy associated with their formation and existence. The motion of domain walls is a primary means of reversing magnetization. In large particles (above 100 nm), energetic considerations

favor the formation of domain walls. Magnetization reversal occurs through nucleation and motion of the walls. With these large particles the coercivity does not change much with size changes. On the other hand, nanoparticles behave as single domains where particle size is directly related to coercivity. As the particle size decreases toward some critical particle diameter (D_c) the formation of domain walls becomes energetically unfavorable, hence they are called single domains. Changes in magnetization can no longer occur through domain wall motion and instead require the coherent rotation of spins, resulting in larger coercivities. As the particle size continues to decrease below the single domain value, the spins are increasingly affected by thermal fluctuations and eventually become superparamagnetic.[1, 4, 44, 45] Figure 1.5 provides a visual graph to show this theory.

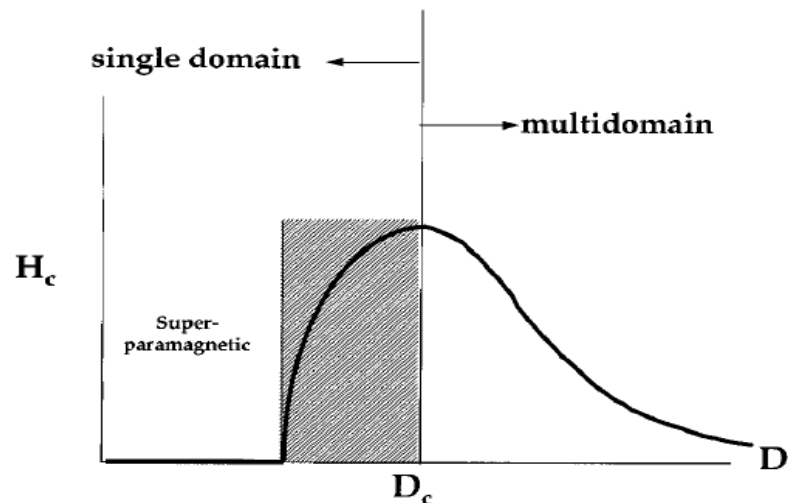


Figure 1.5 Coercivity as a function of particle size[4]

Magnetic anisotropy is a term used when describing magnetic materials. A magnetic material possess magnetic anisotropy if its internal energy depends on the direction of its spontaneous magnetization with respect to its crystallographic axes.[44] A more simple way to describe anisotropy is the magnetic properties depend on the direction in which they are measured.[4] Materials with high values of anisotropy ($K \sim 10^7$ erg/cc) are attractive candidates for use in magnetic recording. Common types of anisotropy include crystalline (magnetocrystalline), shape, stress-induced, and exchange.[4] For this research it is only important to discuss crystalline and shape anisotropy. Crystalline anisotropy arises from spin-orbital coupling and energetically favors alignment of the magnetization along a specific crystallographic axis. This axis with the energy minimum is called the “easy” axis. Crystalline anisotropy is specific to the material and independent of particle shape. The direction of easy magnetization of a crystal is the direction of spontaneous domain magnetization in a demagnetized state. This means that the easy axis plane of the crystal’s domain wall motion is at the magnetic potential energy minimum.[4, 45]

Usually materials with hexagonal or tetragonal crystal structure exhibit crystalline anisotropy. Crystalline anisotropies are calculated using equation 1.1 for nanoparticles by assuming an assembly of uniaxial, single domain particles where K is the anisotropy constant (erg/cc), V is the volume, and θ is the angle between M_s and the easy axis.[4, 45] If the volume of particles is V , then the energy barrier ΔE that must be overcome before a particle can reverse its magnetization is KV ergs.

$$(1.1) \quad E = KV\sin^2\theta$$

Shape anisotropy occurs in acicular magnetic particles such as MP used in today's commercial tape. Consider a polycrystalline specimen having no preferred orientation of its grains; therefore it has no crystalline anisotropy. If the specimen is spherical in shape, the same applied field will magnetize it to the same extent in any direction cancelling out the magnetizations. But if it is non-spherical, it is easier to magnetize it along a long axis than along a short axis. Therefore, shape alone can be a source of magnetic anisotropy.[4] Shape anisotropy is described in aspect ratios. An aspect ratio is the ratio of the length to the width of the particle. The aspect ratio is directly proportional to the anisotropy.

The thermal effect is a fundamental limit in magnetic recording. Magnetic recording media must be able to store data for long periods of time typically greater than 10 years. The thermal effect makes medium coercivity time dependent.[1, 4] Sharrock's law is used to determine a medium's thermal stability by extracting KV/kT data and is shown in equation 1.2.

$$(1.2) \quad \text{Sharrock equation: } H_c(t) = H_0 \{1 - [kT/KV \ln(f_0 t / 0.693)]^{1/m}\}$$

The parameters of Sharrock's law are as follows: H_c = medium coercivity, H_0 = intrinsic coercivity, k = Boltzmann's constant, T = temperature, K = anisotropy constant, V = volume, t = time, $f_0 = 1 \times 10^9$, and m = constant. The most important information that

can be extracted from the Sharrock equation is the particle's thermal stability, KV/kT . KV/kT is the magnetic energy vs. the thermal energy and is directly proportional to the relaxation time for the medium.[4, 44] KV/kT data can be plugged into the Arrhenius equation to calculate the time before the media spontaneously reverses magnetization and data is lost. This is shown in equation 1.3.

$$(1.3) \quad t = 1/f_0 \exp(KV/kT)$$

Values for media used for magnetic recording are on the order of $KV/kT > 60$, which equals a time of 10^9 years.[1, 3, 4, 44] AlMn nanoparticles must exhibit a thermal stability value greater than 60 to be able to use in magnetic recording.

1.4 Metal Nanoparticle Systems

The discovery of the extraordinary magnetic properties of the $L1_0$ class of permanent magnet materials dates back to the 1930's to the finding of the CoPt alloy's attractive magnetic properties tailored through heat treatment. The family of $L1_0$ magnetic alloys is most predominately represented by the CoPt, FePt, FePd, and AlMn binary systems in which the tetragonal $L1_0$ phase derives from a high temperature close-packed phase in the solid state.[46,47,67,68,69] In the CoPt, FePt, and FePd alloy systems the $L1_0$ phase is a stable ordered phase and a crystallographic derivative of a parent face centered cubic disordered solid solution.[46,47,53,54] In the AlMn system the $L1_0$ phase is metastable phase forming from a hexagonal parent phase.[13-17] Metal

alloy systems that include a tetragonal $L1_0$ intermetallic phase exhibit uniaxial magnetocrystalline anisotropies in the range of $K = 10^6 - 10^8$ erg/cc with an “easy” c-axis.[67] The most well studied nanoparticles of these metal alloy systems is FePt, and the FePt phase diagram is shown in figure 1.6.[69] Figure 1.6 shows that the $L1_0$ phase of FePt occurs between about 40-60 mol% Pt which is about 35-62 at% Pt. Compared to the AlMn phase diagram (figure 1.3), the FePt phase diagram is much less complex and there are many more phases present in the AlMn phase diagram. Over the past decade there has been an explosion of interest in these $L1_0$

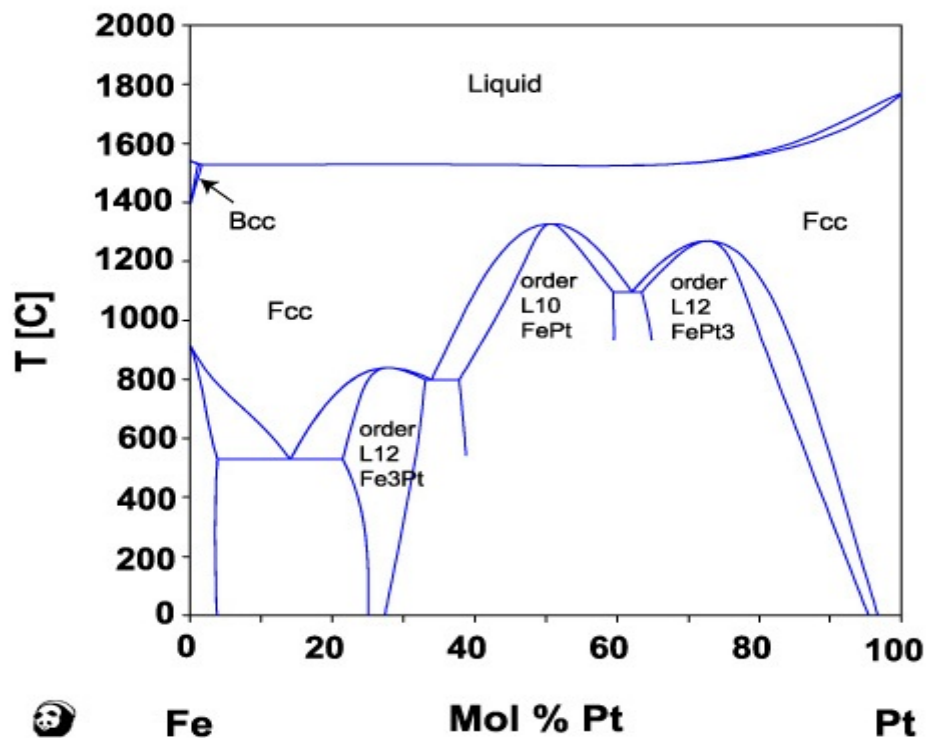


Figure 1.6 FePt phase diagram[69]

intermetallic phases and their associated magnetic properties in nanoparticles for use in a variety of areas including magnetic recording, magneto-optics, spintronics, and medical applications. For magnetic recording applications, solution phase syntheses of nanometer scale crystalline particles of metal alloys have received a great deal of attention and research investigations.[46, 47] In the nanometer size regime, new phenomena characteristics of this intermediate state of matter, found neither in bulk or molecular systems develops. For example, magnetic properties of metals strongly depend on crystallite size in the nanometer size regime.[4, 46] This enforces the need to understand the bulk system but also to investigate general nanoparticle systems as a foundation to develop AlMn nanoparticles. Many research studies have been conducted on CoPt, FePt, and FePd nanoparticle systems while no research investigations on AlMn nanoparticles exist. Since these metal alloy systems have a common $L1_0$ phase with AlMn it could be beneficial to explore the literature on research of CoPt, FePt, FePd, and other metal nanoparticle systems to help in creating an AlMn nanoparticle synthesis. Research knowledge of known systems and synthesis techniques of metal nanoparticles can only enhance in synthesis development techniques for AlMn nanoparticles. Areas of focus on metal nanoparticle systems include synthesis techniques, formation mechanisms, isolation and purification, and thermal treatments to form the $L1_0$ phase.

Metal nanoparticle systems are synthesized mainly by wet chemical solution phase reactions and generally there are four categories of these syntheses. The first is through the reduction of transition metal salt precursors. In this approach a reducing

agent is mixed with the metal precursor salts in the presence of stabilizing agents (ligands, polymers, or surfactants) in an organic solvent to produce metal nanoparticles. The size of the nanoparticles depends on many factors including the type of reducing agent, metal precursor, solvent, concentration, temperature and reaction time. This approach is used by many common transition metal nanoparticles such as FePt, CoPt, MnPt, etc.[46,47,68] The second category is electrochemical synthesis to produce metal nanoparticles. The overall process includes five steps of reaction. First, oxidative dissolution of the sacrificial metal bulk anode occurs. Next, the metal ions migrate to the cathode. Then, reductive formation of zerovalent metal atoms occurs at the cathode followed by nucleation and growth of metal particles. Finally, the growth process concludes and the nanoparticles are stabilized with protecting agents such as surfactants. The electrochemical pathway avoids contamination with by-products resulting from chemical reducing agents, and the products are easily isolated from the precipitate. This process allows size selective particle formation by tuning the current density: high current densities lead to small particles, and vice versa. Particle size is also controlled by adjusting the distance between the electrodes, the reaction time and temperature, or the solvent polarity. This method has been used to prepare monometallic nanoparticles Ni, Co, Ag, Au, etc.[68] Also, recently high surface area core shell nanoparticles have been produced by combining electrochemical and wet chemical methods. The third category is the reduction of organic ligands in organometallic precursors. Starting from low-valence metal complexes, the ligands are typically reduced with H₂ or CO. The reduced

ligands leave the metal in its zero valence state allowing the clustering of metal atoms to form nanoparticles.[68] The fourth category is metal vapor chemistry. In this method, the atomic vapor of a metal is condensed into a cold liquid containing a stabilizer. Upon warming, the dissolved metal atoms form nanoparticles. When the liquid itself acts as a stabilizer, the metal vapor can condense with the solvent vapor giving a solid matrix of nanoparticles.[68]

Most metal nanoparticles utilize the first technique of reduction of metal salt precursors for synthesis, so this technique is explored in depth along with the mechanism of formation of the nanoparticles. In these reactions, nucleation and growth of the nanoparticles are allowed to take place over an extended period of time at a moderate temperature range between 100-300°C which yields a wide range of sizes. Expanding on this strategy, new developments of nanoparticle syntheses have been established. Well separated and nearly monodispersed Au, Ag, and Pt nanocrystals have been prepared at room temperature by reducing the corresponding metal salt in an aqueous solution or via a two phase reduction method.[49] On the other hand, syntheses of high quality transition metal nanoparticles require different approaches because these particles do not crystallize well at room temperature.[46, 47] The most established early methods involved aqueous reduction of metal salts in the presence of citrate anions. Higher temperature reduction of metal salts or organometallic precursors in the presence of stabilizing ligands can be employed to produce transition metal nanoparticles. In the general scheme, organometallic precursors are dissolved in a high boiling point solvent

along with a combination of ligands. The solution is vigorously stirred and heated between 100-350°C during which a strong reducing agent is injected. Metal nanoparticles nucleate and grow until the reagent is consumed.[46, 47] Such recipes have been developed for Fe[50, 51], Co[11, 12, 52, 53], Ni[51] and alloys of FePt[12, 54] and CoPt[53] nanoparticles. Also, metal nanoparticles have been produced of MnPt₃[65] and various manganese oxides such as MnO and Mn₃O₄. [66] The information from the references on the manganese nanocrystals could be useful because they use the same organometallic precursors (Mn(acac)₂, Mn₂(CO)₁₀) that will be used in AlMn synthesis attempts.

Size control in the hot organometallic of metal nanoparticles is a kinetically driven process where the ratio between the rates of nucleation and for growth is responsible for the final nanoparticle size.[47] Murray et al. did a thorough study on general synthesis and characterization of metal nanoparticles which gives great insight into the overall process of making nanoparticles. The investigation presents methods for solution phase synthesis along with separation methods for metal nanoparticles, tunable in size from 1-20 nm.[46] Classic studies by LaMer and Dinegar show that the production of nanoparticle colloids requires a temporarily discrete nucleation event followed by a slower controlled growth on the existing nuclei.[55] Since the growth of any one nanocrystal is similar to all others, the initial size distribution is largely determined by the time over which the nuclei are formed and begin to grow. Nuclei are formed in the synthesis when the organometallic precursor is reduced to its zero valence

state by an added reducing agent. If the percentage of nanocrystal growth during the nucleation period is small compared with subsequent growth, the nanocrystals become more uniform in size over time.[56] The kinetics of FePt nanoparticles have been studied and during the initial stages of the reaction the Pt source is reduced and Pt seeds or nuclei are formed in the solution. As the Fe source is reduced either by thermal decomposition or by a reducing agent such as superhydride, the Fe nucleates with the Pt seeds to grow FePt nanoparticles. This phenomenon is referred to as focusing.[46, 47, 49, 57] Some systems exhibit a second, distinct, growth phase called Ostwald ripening.[58, 59] In this process the high surface energy of the small nanocrystals promotes their dissolution whereby monomer is released and consumed or redeposited on larger nanocrystals.[46, 47, 57] Most transition metal nanoparticles such as FePt and CoPt do not exhibit Ostwald ripening.

Since “naked” nanoparticles are kinetically unstable in solution, all preparation methods must use stabilizing agents, which adsorb to the particle’s surface. Stabilizing agents must be present during growth to prevent agglomeration and precipitation of the nanoparticles. When the stabilizing molecules are attached to the nanoparticle surface as a monolayer through covalent or ionic bonds they are referred to as a capping group.[60] The capping groups serve to mediate nanoparticle growth, sterically stabilize nanoparticles in solution, and help prevent surface oxidation.[46] There are three types of nanoparticle stabilization. First, electrostatic stabilization occurs when cations and anions from the starting materials remain in solution and associate with the nanoparticles.

The particles are surrounded by an electrical double layer which results in a coulombic repulsion that prevents agglomeration. Second, steric stabilization prevents particle aggregation through adsorption of large molecules such as polymers or surfactants. The third type of stabilization is a combination of both electrostatic and steric effects called electrosteric stabilization.[68]

After a particle synthesis, isolation and purification of the particles is required to separate the remnant byproducts and organic leftovers from the particles. If the capping groups are well bound to the surface of the nanoparticles, the resulting particles are re-dispersable in a variety of solvents such as: alkanes, aromatics, long-chain alcohols, and organic bases. The particles must initially be precipitated from the reaction solution. Size-selective precipitation involves the titration of a non solvent into the dispersion.[61] Ethanol is commonly used to precipitate out the particles. Since the largest nanoparticles in the size distribution exhibits the greatest attractive van der Waals forces, they tend to aggregate before smaller nanoparticles. As aggregates of larger particles form, there is a tendency to exclude the smaller particles.[62, 63] If the dispersion is allowed to only partially flocculate, filtering or centrifuging the suspension isolates a precipitate enriched in larger nanoparticles and leaves the smaller nanoparticles dispersed in the supernatant. Small nanoparticles (less than 2 nm) are difficult to precipitate while large nanoparticles (10 nm or greater) are difficult to re-disperse, so this size selective isolation and purification technique only works with particles in the range of 2-10 nm. Addition of more nonsolvent (ethanol) to the decanted supernatant brings about a second precipitation

of the particles.[46] Another washing technique for metal nanoparticles that can be utilized is a phase transfer method of nanoparticles synthesized in an organic medium to an aqueous medium. The use of tetramethylammonium hydroxide (TMAOH) as the phase transfer agent can successfully make nanoparticles fully re-dispersed in aqueous solution.[64]

Most metal nanoparticles are paramagnetic as made from each synthesis, and they require a subsequent heat treatment or annealing to transform into the ferromagnetic phase. For FePt, the as-made particles have a face centered cubic (fcc) structure which is non-magnetic. An annealing procedure, done in a tube furnace with temperatures ranging from 550-750°C under an atmosphere of 95 at % Ar and 5 at % H₂, is required to transform the particles to the ferromagnetic tetragonal (L1₀) structure.[10] FePt particles are fully transformed to the L1₀ phase at temperatures above 600°C which results in superlattice peaks formed in the XRD spectrum. There are many problems associated with high temperature annealing of nanoparticles such as agglomeration and sintering. Sintering causes grain growth in the particles resulting in large non-uniform particle sizes which can prevent the formation of a regular array. Salt annealing is a simple method to prevent sintering and agglomeration, while still achieving fully transformed L1₀ FePt nanoparticles. Salt (NaCl) powders of small sizes (less than 20 μm) are combined with the as made fcc particles. The salt separates the particles during the annealing process which prevents sintering while allowing phase transformation. After annealing, the salt is washed out with water leaving L1₀ FePt nanoparticles. As seen in bulk alloys of AlMn, a

precise heat treatment is required to transform to the τ phase, so it is assumed that a specific heat treatment would be required to transform as made AlMn nanoparticles into the ferromagnetic τ phase.

The well studied systems of transition metal nanoparticles provide insight into synthesis techniques, annealing procedures, and mechanisms of formation that can be used as a foundation to develop a synthesis technique for AlMn nanoparticles. It is expected that AlMn nanoparticles will have differences compared to other metal nanoparticles, but understanding these other systems will help develop a platform of strategies to develop AlMn nanoparticles.

1.5 Dissertation Objectives

This dissertation reports the research project on strategies to produce AlMn nanoparticles through a wet chemical synthesis and includes several objectives. The first objective is to try to develop a reliable and reproducible solution phase chemical synthesis of AlMn nanoparticles with sizes under 10 nm. It is also imperative to report failed synthesis attempts to detail what methods or techniques are unsuccessful for producing AlMn nanoparticles. By accounting for what does not work in these synthesis attempts, it helps to narrow the enormous scope of the main objective of creating a successful synthesis. If a synthesis is discovered that produces AlMn nanoparticles it is necessary to characterize the structure of the as-made phase. The AlMn phase diagram does not include the phase or phases of this system that would occur under the conditions

of a solution phase chemical synthesis. Also, if a successful synthesis is found, then an objective is to try to find the thermal treatment parameters needed to transform the particles to the ferromagnetic τ phase. This dissertation reports efforts to meet these objectives to develop and characterize a reliable solution phase chemical synthesis of AlMn nanoparticles.

CHAPTER 2

EXPERIMENTAL METHODS

2.1 Chemicals and Materials

Many chemicals were used during the course of this research as precursors, solvents, surfactants, isolation and purification materials, and reduction agents. Table 2.1 shows the metal precursors and solvents, and Table 2.2 shows the reducing agents and surfactants used in wet chemical synthesis attempts of AlMn nanoparticles.

Chemicals used for cyclic voltammetry (CV) experiments included tetraethylammonium tetrafluoroborate, tetrabutylammonium tetrafluoroborate, and calcium hydride (CaH_2) that were purchased from Aldrich. Other chemicals included ethanol, methanol, hexane, cyclohexane, 2-butanone, and toluene that were used for isolation and purification procedures, and they were purchased from Fisher. Deionized (DI) water was used to prepare aqueous solutions. Excluding chemicals used for CV experiments, all of the chemicals were used without further purification.

Chemicals and Materials used for AlMn Wet Chemical Synthesis Attempts	
Metal Precursors	Solvents
aluminum acetylacetonate (Al(acac) ₃ , 99%)	diphenyl ether (C ₁₂ H ₁₀ O, 70%)
manganese acetylacetonate (Mn(acac) ₃ , 98%)	benzyl ether (C ₈ H ₁₈ O ₅ , 99%)
manganese acetylacetonate Mn(acac) ₂ , 98%)	dioctyl ether (99%)
dimanganese decacarbonyl (Mn ₂ (CO) ₁₀ , 98%)	tri-n-octylamine (TOA, C ₂₄ H ₅₁ N, 99%)
alumina (Al ₂ O ₃)	pyridine (C ₅ H ₅ N, 99%)
aluminum chloride (AlCl ₃)	dimethylformamide (DMF, HCON(CH ₃) ₂ , 99%)
manganese chloride (MnCl ₂)	
trioctylaluminum (C ₂₄ H ₅₁ Al, 25%)	
iron acetylacetonate (Fe(acac) ₂ , 97%)	
copper acetylacetonate (Cu(acac) ₂ , 98%)	
platinum acetylacetonate (Pt(acac) ₂ , 97%)	
nickel acetylacetonate (Ni(acac) ₂)	
gold acetate (Au(O ₂ CCH ₃) ₃)	

Table 2.1 Metal precursors and solvents used in synthesis attempts

Chemicals and Materials used for AlMn Wet Chemical Synthesis Attempts	
Reducing Agents	Surfactants
1,2-hexadecandiol (C ₁₆ H ₃₄ O ₂ , 90%)	oleic acid (C ₁₈ H ₃₄ O ₂ , 90%)
lithium triethylborohydride (Superhydride, C ₆ H ₁₆ BLi)	oleylamine (C ₁₈ H ₃₇ N, 70%)
lithium aluminum hydride (LiAlH ₄ , 2M in THF)	trioctylphosphine (TOP, C ₂₄ H ₅ P, 90%)
sodium metal (Na stored in kerosene)	tetramethylammonium hydroxide (C ₄ H ₁₃ NO, 25%)
potassium metal (K stored in kerosene)	

Table 2.2 Reducing agents and surfactants used in synthesis attempts

2.2 Synthetic Procedures

With no prior knowledge of synthesis techniques of AlMn nanoparticles, many hundreds of synthesis techniques were conducted during the course of this research. The chemicals listed in the previous paragraph were all used in various combinations to find a successful wet chemical synthesis route to produce AlMn nanoparticles.

The general setup for each reaction remained constant while the precursors, solvents, surfactants, and reducing agents were interchanged to try and find the optimum synthesis route to generate AlMn nanoparticles. The general reaction setup is discussed in detail. First, the precursors and solvent were added to a 100 mL three necked round

bottom flask equipped with a magnetic stir bar, a reflux condenser, and a thermocouple or thermometer. The magnetic stir bar was set at medium speed to ensure good mixing during the reaction. The reflux condenser had cold water running continuously through it to prevent evaporation of the solvent during the reaction at reflux temperature. The thermocouple or thermometer monitored reaction temperature and heating rates. Illustration 2.1 shows this general setup with a schematic, while figure 2.1 shows a picture of an actual reaction setup. Next, the mixture in the flask was heated from room temperature to 100°C at a rate of approximately 10-15°C/min under an inert atmosphere provided by constant flow of N₂. When the solution reached 100°C, the surfactant(s) was injected slowly by syringe. Then the solution was heated to 200°C with the same heating rate, and the reducing agent was incorporated into the solution either by injection from a syringe or by dropping the solid into the solution. The reaction solution was heated at the same heating rate to reflux (boiling point of the solvent) and kept there for 30-45 minutes. When the solution turned black during a reaction, this indicated particle formation. Afterwards, the obtained black particle dispersion was allowed to cool to room temperature, then the dispersion was transferred to a 50 or 100 mL beaker and 20-40 mL of ethanol or methanol was added to precipitate the particles.

Figure 2.2 shows a flow chart for a synthesis of AlMn nanoparticles. After the particle synthesis, an isolation and purification procedure sometimes referred to as a washing and cleaning procedure was implemented to isolate the particles from the leftover reaction byproducts and remove excess surfactant and other organics. The

particles were isolated and purified by centrifugation after the addition of a flocculent (ethanol, methanol, etc.) and re-dispersed in a nonpolar solvent (hexane, toluene, etc.) or an aqueous solvent. This procedure typically works for particles in the size range of 2-10 nm and is the most common technique used in metal nanoparticle synthesis techniques. Particles that are less than 2 nm are difficult to precipitate out from the reaction solution,

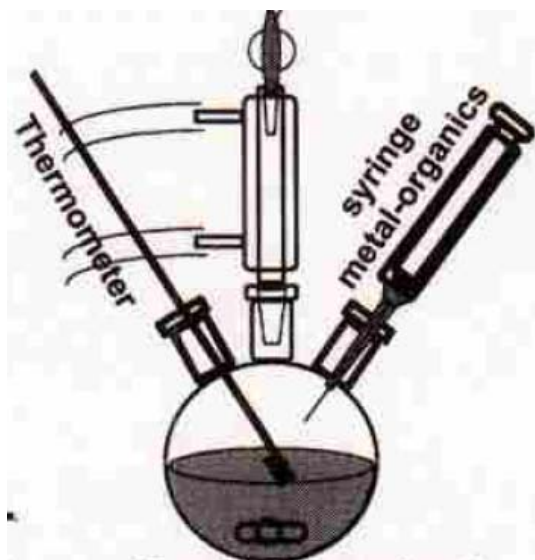


Illustration 2.1 AlMn reaction setup[46]

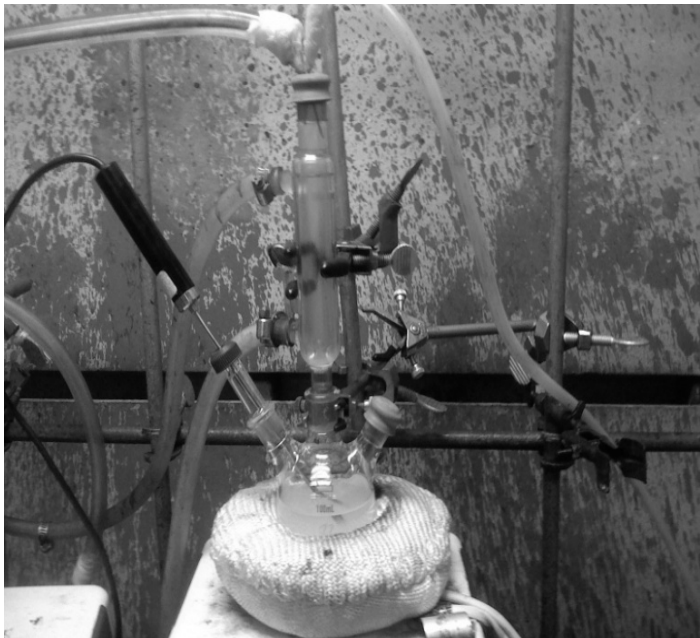


Figure 2.1 Picture of an AlMn reaction setup

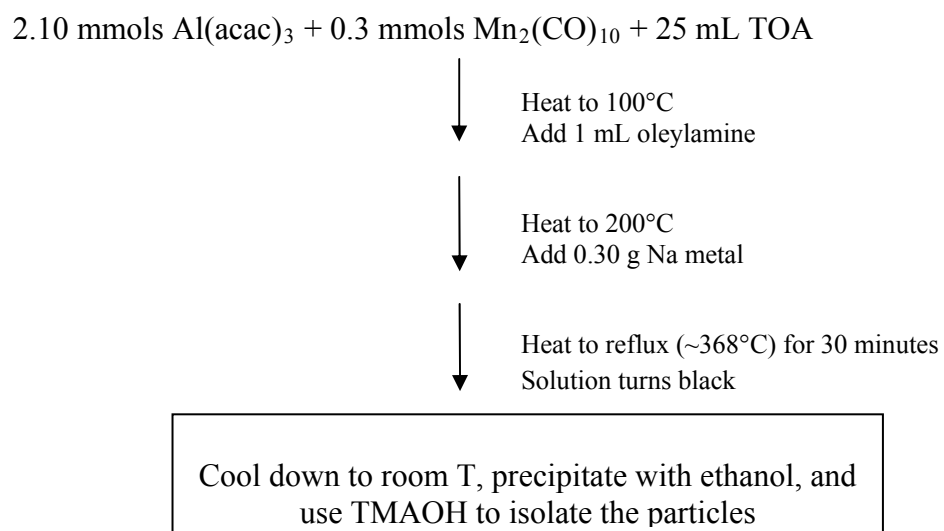


Figure 2.2 Flow chart of an AlMn nanoparticle synthesis

while particles that are larger than 10 nm are difficult to re-disperse.

Several isolation and purification procedures were used for AlMn nanoparticle reactions which included the standard technique, the phase transfer technique, and the technique used for MnPt and MnO reactions. These methods are detailed in the sections below so that in chapter 3 every isolation and purification procedure does not have to be described in detail for each reaction discussed in the next chapter.

2.2.1 Standard Isolation and Purification Technique

The isolation and purification procedure used for metal nanoparticles (FePt, CoPt, MnPt, etc.) was used for most of the AlMn nanoparticles synthesis attempts and referred to as the standard isolation and purification procedure in this dissertation.[10,54] The procedure started by pouring the reaction product from the round bottom flask into a 100 mL beaker followed by the addition of around 40 mL of ethanol to precipitate the particles. This solution was allowed to sit for several hours (4-6 hours) to allow the particles to precipitate and fall to the bottom of the beaker. The solution was centrifuged using 10 mL centrifuge tubes for 10 minutes at 3000 rpm and the precipitate was kept while the supernatant was discarded. The precipitate was dried at room temperature for 10-15 minutes to ensure all the ethanol had evaporated followed by re-dispersing the precipitate in 20 mL hexane and 0.1 mL oleylamine and 0.1 mL oleic acid to separate the particles from unwanted reaction products. The solution was sonicated for 10 minutes to allow mixing then centrifuged for 10 minutes at 3000 rpm.[10,54] The particles were re-dispersed in the supernatant while the precipitate contained unwanted reaction products.

The precipitate or sediment was kept and stored in hexane for analysis. Ethanol (20-40 mL) was added to the supernatant and placed in a storage vial overnight to re-precipitate the particles. The particles precipitated overnight by falling to the bottom of the storage vial. This solution was centrifuged for 10 minutes at 3000 rpm, and the supernatant was discarded while the particles were allowed to dry for 15-20 minutes. After drying, the particles were stored in hexane for analysis.[10,54]

2.2.2 Phase Transfer Isolation and Purification Technique

Another technique for isolation and purification of AlMn nanoparticles utilized a phase transfer method to allow the particles to be soluble in an aqueous medium. Veronica et al. used this procedure to transfer FePt nanoparticles from an organic to an aqueous medium, and it was incorporated with slight adjustments for some AlMn nanoparticle reactions in this research.[64] This procedure started with precipitation of the particles with ethanol from the reaction solution by adding approximately 40 mL of ethanol with the synthesis product into a 100 mL beaker. This solution was allowed to sit for several hours to allow the particles to precipitate and fall to the bottom of the beaker. The precipitated particles were centrifuged in 10 mL centrifuge tubes for 10 minutes at 3000 rpm and the supernatant discarded followed by a drying period of 30 minutes at room temperature. Then 2 mL of tetramethylammonium hydroxide (TMAOH) was added to the particles in the centrifuge tube and allowed to sonicate for 10-15 minutes to ensure good mixing. Next the solution in the centrifuge tube and approximately 60 mL of DI water was added to a 100 mL beaker followed by sonication for 30 minutes.

Parafin film was placed on top of the beaker to seal the contents of the beaker during sonication. This solution was transferred to 10 mL centrifuge tubes and centrifuged for 10 minutes at 3000 rpm. The supernatant was discarded while the particles were kept. Next the particles were re-dispersed with DI water only, sonicated for 5 minutes, and centrifuged for 5 minutes at 3000 rpm to remove organics left from the reaction. This last part of the procedure was repeated 3 to 4 times to ensure that the organics were completely removed.[64] The particles could then be stored in DI water only. The problem with just storing in DI water was that it took an extremely long time for the solution to dry on a Si wafer to perform analysis. Also, particles washed and cleaned by this method and stored in DI water tended not to form an evenly proportioned layer of particles on a Si wafer which negatively affected analysis.

For the AlMn reactions in this research, the following steps were taken to transfer the particles back to an organic solvent to allow easier analysis. This step may sound contradictory to the purpose of transferring from an organic medium to an aqueous medium, but this method was only used for AlMn reactions that used Na as the reducing agent. Excess Na is difficult to remove by the normal washing and cleaning procedure, so this phase transfer method was implemented to remove Na from the final reaction product in AlMn syntheses. Na readily reacts with water to form sodium hydroxide and hydrogen gas by the reaction as shown in equation 2.1. During this phase transfer washing and cleaning method, excess Na that remained in the reaction precipitate was

removed. This ensured that the particles were separated from the unwanted products generated during AlMn reactions using Na.



This final precipitate was dried at room temperature for 20-30 minutes, and then re-dispersed in 20 mL hexane and 0.1 mL oleylamine and 0.1 mL oleic acid. This solution was sonicated followed by centrifugation and the supernatant discarded. The particles were then re-dispersed in ethanol, sonicated, and centrifuged. The particles were allowed to dry for 30 minutes, and stored in hexane for analysis.

2.2.3 Isolation and Purification Technique from MnPt and MnO Reactions

Another isolation and purification technique that was used on AlMn reactions modeled a procedure used on MnPt and MnO nanoparticle syntheses. This technique is similar to the standard technique principles, but the steps of the procedure differ.[64,65] The reaction product was poured into a 100 mL beaker followed by the addition of 5 mL of hexane and 0.1 mL of oleic acid and 0.1 mL of oleylamine. This solution was sonicated for 5 minutes and paraffin film was used to cover the beaker to prevent contamination of the solution. The solution was centrifuged in 10 mL centrifuge tubes for 5-10 minutes at 3000 rpm. The particles were dispersed in the supernatant after centrifugation and the unwanted reaction products were collected in the precipitate or sediment at the bottom of the centrifuge tube. The sediment was kept for analysis and stored in hexane. The supernatant was added to a 100 mL beaker with 20-40 mL of

ethanol to precipitate the particles. The solution was allowed to sit for 30 minutes and then centrifuged in 10 mL centrifuge tubes for 10 minutes at 3000 rpm. The particles were allowed to dry for 30 minutes to allow for the evaporation of remaining ethanol then stored in hexane for analysis.[64,65]

2.3 Characterization Techniques

2.3.1. X-ray Diffraction (XRD)

XRD is an analytical tool for characterization of the phase and structure of crystalline materials. In XRD, only the planes in crystalline materials that satisfy Bragg's Law (shown in equation 2.2) will generate diffraction peaks.

$$(2.2) \quad n\lambda = 2d\sin\theta$$

The parameters of Bragg's Law are defined as follows: n is the diffraction order (usually 1), λ is the wavelength of the incident x-ray, d is the spacing between the two adjacent planes (d-spacing), and θ is the diffraction angle of corresponding planes.[70] Illustration 2.2 gives a visual description of x-ray diffraction and Bragg's Law.

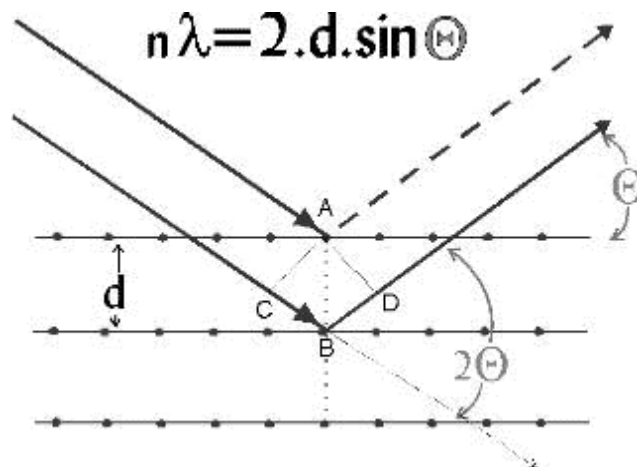


Illustration 2.2 Schematic of XRD and Bragg's Law [65]

Acquired diffraction patterns can be indexed based on the Joint Committee on Powder Diffraction Standards (JCPDS) or the International Center for Diffraction Data (ICDD) database and corresponding d-spacings can be calculated. For this dissertation, XRD patterns were obtained with the use of two diffractometers; a Rigaku model D/MAX-2BX and a Phillips Xpert both with a Cu $K\alpha$ x-ray source ($\lambda = 1.5406 \text{ \AA}$). The operating voltage and current used were 40 kV and 35 mA, respectively. The scan mode of these diffractometers was θ - 2θ scan, in which only the angle between the incident x-ray and diffracted x-ray was measured when the condition of Bragg's Law was met. Samples for XRD characterization were prepared by dropping several drops of particles dispersed in hexane onto silicon substrates, followed by evaporation of the hexane at room temperature. To remove the silicon peak caused by the substrate, the θ value was offset slightly by usually less than $\pm 1^\circ$. The only difference in the two diffractometers

was the sample size that was measured. In the Rigaku, a large sample size of 1 x 2 cm had to be used while in the Phillips the sample size can be less than 1 x 1 cm.

The values of 2θ were calculated for both the ϵ and τ phases, thus x-ray diffraction patterns were indexed. Samples produced from this research were compared to these XRD patterns. The lattice parameters and structure of both phases were known from literature (Section 1.2), therefore 2θ values were calculated. D-spacings for individual planes were calculated for the hexagonal structured ϵ phase and the tetragonal structured τ phase using equation 2.3 and 2.4, respectively. The parameters for equation 2.2 and 2.3 are as follows: d = d-spacing, hkl = the miller indices for each plane, and lattice parameters a and c . The calculated d-spacings were put into Bragg's Law (equation 2.2) to calculate 2θ . Table 2.3 shows the calculated d-spacings for the ϵ phase, and table 2.4 shows the calculated results for the τ phase.[13,15,29,30]

$$(2.3) \quad \text{Hexagonal equation: } 1/d_{hkl}^2 = 4/3(h^2 + hk + k^2/a^2) + l^2/c^2$$

$$(2.4) \quad \text{Tetragonal equation: } 1/d_{hkl}^2 = (h^2 + k^2)/a^2 + l^2/c^2$$

hkl	d (Å)	sinθ	θ	2θ
002	2.1900	0.3517	20.59	41.19
100	2.3296	0.3307	19.31	38.62
101	2.0568	0.3745	21.99	43.99
102	1.5956	0.4828	28.87	57.73
110	1.3450	0.5727	34.94	69.88
111	1.2857	0.5991	36.81	73.61
103	1.2371	0.6227	38.51	77.02
004	1.0950	0.7035	44.71	89.41
112	1.1461	0.6721	42.23	84.46
200	1.1648	0.6613	41.40	82.80
201	1.1257	0.6843	43.18	86.36

Table 2.3 Calculated d-spacings from the hexagonal ϵ phase

hkl	d (Å)	sinθ	θ	2θ
001	3.5800	0.2152	12.43	24.85
110	2.7860	0.2765	16.05	32.10
111	2.1987	0.3503	20.51	41.02
200	1.9700	0.3910	23.02	46.04
002	1.7900	0.4303	25.49	50.98
201	1.7259	0.4463	26.51	53.01
112	1.5060	0.5115	30.76	61.53
220	1.3930	0.5530	33.57	67.14
202	1.3248	0.5814	35.55	71.10
221	1.2982	0.5934	36.40	72.79
310	1.2459	0.6182	38.19	76.38
003	1.1933	0.6455	40.20	80.41
131	1.1767	0.6546	40.89	81.78
222	1.0993	0.7007	44.48	88.97
113	1.0969	0.7022	44.61	89.21

Table 2.4 Calculated d-spacings from the tetragonal τ phase

For samples of nanoparticles, the width of diffraction peaks can be directly correlated to the average size of the particles by using the Scherrer equation shown in equation 2.5.[10,15,54]

$$(2.5) \quad d = k\lambda/\beta\cos\theta$$

The parameters of equation 2.5 are defined as follows: d is the size of the particles, k is a coefficient (0.9), λ is the wavelength of incident x-ray, β is the full width a half maximum (FWHM) of the largest diffraction peak, and θ is the diffraction angle. In this dissertation, the average XRD scan was from 20 - 60° 2θ .

2.3.2. Transmission Electron Microscopy (TEM)

An FEI TECNAI F20 transmission electron microscope was used to characterize the size, shape, and crystal structure of the nanoparticles. TEM is a technique that uses a beam of electrons transmitted through an ultra thin specimen, interacting with the specimen as it passes through it to create an image.[70] An image is formed from the electrons transmitted through the specimen, magnified and focused by an objective lens, and then appears on a phosphorous imaging screen. The TEM is composed of several components which include an electron emission source, a series of electromagnetic lenses to focus the beam and image, and a vacuum system for the electrons to travel. Electrons are generated by a field emission gun (FEG). The FEG has a tip held at a negative potential relative to a nearby electrode, so this potential gradient at the tip's surface

produces a field emission of electrons. The FEG produces an electron beam that is smaller in diameter, more coherent, and can generate up to three orders of magnitude greater current density (brightness) than a thermionic emission source.

A set of electromagnetic lenses, typically two condenser lens, one objective lens, and a projector lens, manipulate the electron beam as it passes through each lens to create a final image of the specimen. First, the electron beam leaves the FEG and passes through two condenser lenses whose primary function is the formation of the beam. When the electron beam encounters the condenser lenses, they concentrate the beam and bring it to a point of focus well above the specimen plane. Apertures in the condenser lenses are used to control the intensity and angle of convergence of the beam. This process in the initial stage of the TEM forms the brightness of the final image. Next, the beam travels through the specimen and the objective lens. The objective lens is the most important lens in the TEM, since it forms the images and diffraction patterns that will be magnified by all other lenses. Changes to the current flowing through the objective lens constitute the microscope's focus control. The magnified image from the objective lens is further enlarged by two lenses called the intermediate lens and projector lens. Finally, electrons leave the projector lens and strike a screen coated with a fluorescent material which is usually phosphorous.[70] In order for this process to occur and achieve an uninterrupted passage of electrons, the TEM must be held under low pressures typically on the order of 10^{-4} to 10^{-8} kPa. These low pressures must be maintained to ensure that

the TEM remains under proper vacuum conditions. Illustration 2.3 shows the components of a TEM. The virtual source corresponds to the electron gun (FEG).

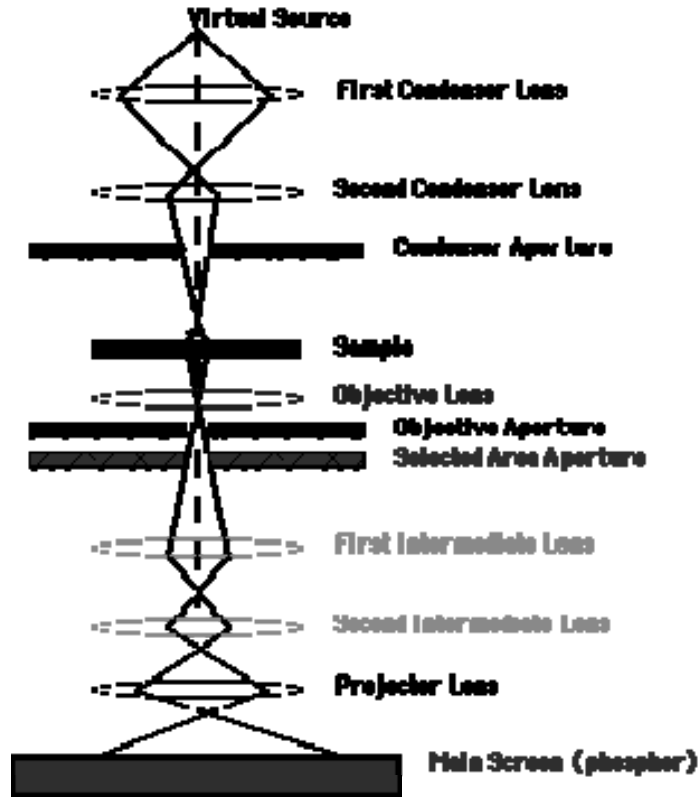


Illustration 2.3 Schematic diagram of TEM components[66]

In this dissertation, the FEI TECHNAI F20 TEM was used for imaging of the particles including high resolution imaging, STEM imaging, EDS spectra, and selected area electron diffraction patterns. The diffraction patterns were taken by a camera on the TEM, and then the film was developed into an image with diffraction rings. Equation 2.6 is used to determine d-spacing from electron diffraction patterns taken on the TEM.

$$(2.6) \quad dR = \lambda L$$

The parameters of equation 2.6 are defined as follows: d -spacing (\AA), R is the radius of the diffraction ring (mm), λ is the wavelength of the electron beam (0.0254 \AA), and L is the camera length (mm).[70] TEM samples were made by placing several drops of very dilute particle dispersion on carbon-coated copper grids followed by a drying period at room temperature.

For basic imaging and electron diffraction patterns no additional procedure was required. To perform high resolution imaging, STEM imaging, and EDS analysis an addition oven heating at 170°C overnight was necessary. This step was done to remove excess surfactants and organics left on the particles even after a cleaning and washing procedure has been performed. If this step is not done, the particles will charge making STEM imaging impossible, and therefore, an EDS spectrum impossible to obtain. A silicon nitride grid must be avoided for single particle EDS analysis due to the Si peak and Al peak overlapping in the spectrum, so it is impossible to obtain accurate atomic percentages of Al and Mn. This step also makes taking a high resolution image much easier due to the removal of all amorphous material left on the particles, which can cause drifting at high magnifications making it difficult to obtain a good quality image showing lattice fringes.

2.3.3. Energy Dispersive Spectroscopy Analysis (EDS)

EDS is a widely used technique for elemental and compositional analysis of materials and is sometimes referred to as EDX or EDAX. EDS is an identification technique that uses characteristic x-rays emitted from a specimen to identify the elemental species.[70] EDS can also be used to determine weight and atomic percentages of the elements in a sample. The fundamental concept that makes EDS capable to determine elemental species is that each element produces a unique characteristic x-ray. During EDS analysis, the sample is bombarded with an electron beam. The characteristic x-rays are produced when the incident electron beam collides with the sample. Initially, the incident electrons strike the specimen creating collisions within the atom's many inner shell electrons. This collision causes the ejection of the specimen's inner shell electrons. Outer shell electrons, which have much higher energy than inner shell electrons, seize the opportunity to reduce their energy by replacing the ejected electron from the inner shell. As the outer shell electron moves to the lower energy inner shell vacancy, a characteristic x-ray is emitted. The x-ray's energy is a function of the atomic number of a specific element. The vacancy created in an inner shell from the collision of incident electrons may be filled by an electron from any shell of greater energy.[70]

Illustration 2.4 shows how a characteristic x-ray is produced and the basis of EDS. The path that the outer shell electron takes to the inner shell characterizes the x-ray. Each x-ray is first named for the shell which was initially vacated, so an x-ray

created by filling a K-shell is called a K x-ray. This is also true for all shells including L, M, etc. The x-ray is further distinguished by the size of the electron jump that created it. A vacancy filled by an electron from an adjacent shell creates an x-ray termed “ α ”. If the difference is two shells it is termed “ β ”, and a difference of three shells is termed “ γ ”. Thus, an electron that jumps from an L-shell to a K-shell creates an x-ray that is labeled $K\alpha$. [70] Illustration 2.5 shows the spectrum of x-rays that can be generated from a single element and how those x-rays are labeled.

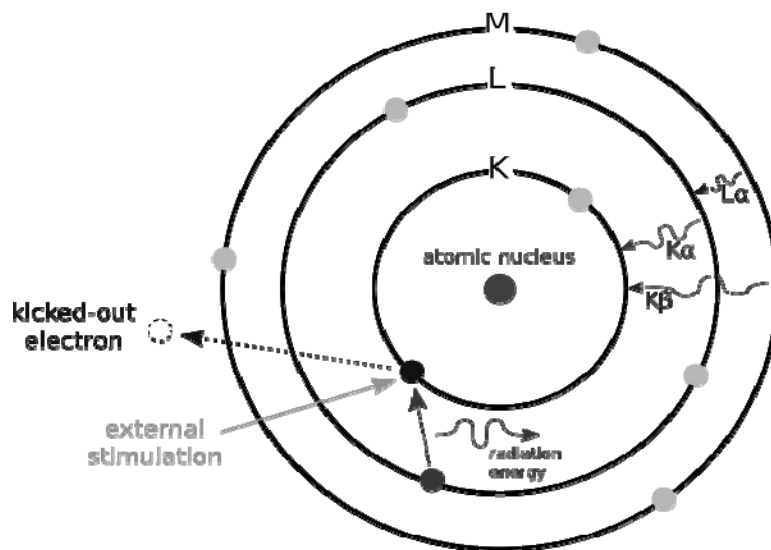


Illustration 2.4

Diagram of the principle of EDS [67]

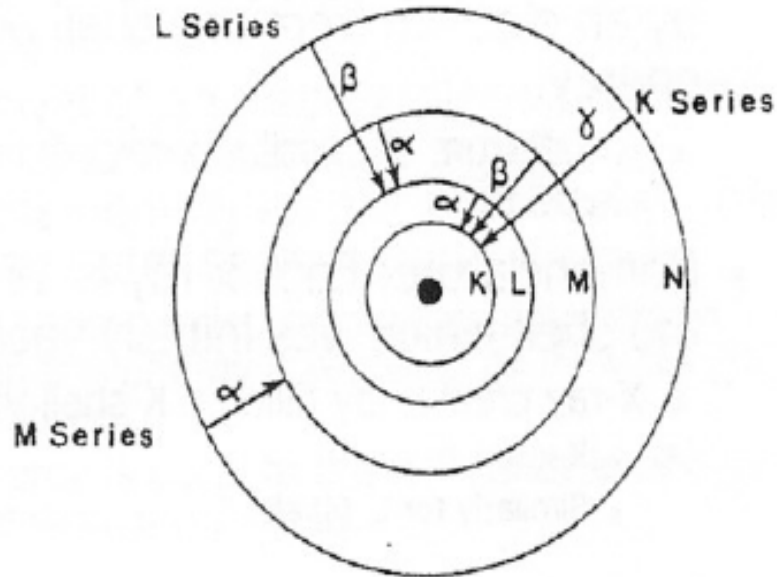


Illustration 2.5 Spectrum of possible x-rays generated from an element [68]

In this dissertation, EDS analysis was used to determine what elements were present along with the average atomic percent compositions of the AlMn nanoparticles. The EDS analysis was performed on a scanning electron microscope (Phillips XL-30). Also, a localized EDS spectrum of single nanoparticles was acquired on a FEI TECNAI S20 transmission electron microscope.

2.3.4. Alternating Gradient Magnetometry (AGM)

AGM is a tool used for characterizing the magnetic properties of a material. The AGM subjects a sample to changing applied field to produce a hysteresis loop that is characteristic of the sample, whereby the magnetic properties of the sample can be extracted. The Princeton Measurement Corporation MicroMag Model 2900 system

(shown in figure 2.3) uses an alternating gradient field to produce a periodic force on a sample placed in a static direct current (dc) field. The sample is mounted on an extension rod attached to a piezoelectric element. Illustration 2.6 shows the setup of the AGM's gradient coil configurations with a sample centered between them. The alternating field gradient exerts an alternating force on the sample proportional to the magnitude of the gradient field and the magnetic moment of the sample. The resulting deflection of the extension is transmitted to the piezoelectric sensing element. The output signal from the piezoelectric element is synchronously detected at the operating frequency of the gradient field. The signal developed by the piezoelectric element is greatly enhanced by operating at or near the mechanical resonant frequency of the AGM assembly. In the Model 2900 assembly, a built-in software function automatically determines mechanical resonance and sets the appropriate operating frequency for the sample under study. By operating near the mechanical resonance frequency, the signal can be amplified, and thus very high sensitivity is achieved. The piezoelectric elements are not sensitive to changing magnetic fields, but they are sensitive to mechanical and acoustic noise sources. To prevent this problem from occurring, the AGM is enclosed in a wood box to prevent outside noise interference.

For characterization in this dissertation, measurements were done using a perpendicular probe at room temperature. Samples were made by dropping a couple drops of particle dispersion onto silicon wafers with approximate size of 3 x 3 mm, and then dried at room temperature. The samples were held in place on the probe with

vacuum grease on the side with no sample. A calibration of the magnetization was performed using a nickel foil with a known magnetic moment before each sample was run. A hysteresis loop was generated for each sample with a maximum applied field of 18 kOe and intervals of 100 Oe to give the magnetic properties of the sample. Also, the AGM was used to perform time dependent remnance measurements to find KV/kT of a sample. For these measurements a series of times (1s, 2s, 5s, 10s, 20s, 50s, 100s, and 200s) were run to pause the applied field for each specific time while it crossed from positive to negative field. A remnant coercivity was measured for each time increment and those values were plotted with the Sharrock equation (equation 1.2) to extract KV/kT data.



Figure 2.3 Picture of the AGM used in this research

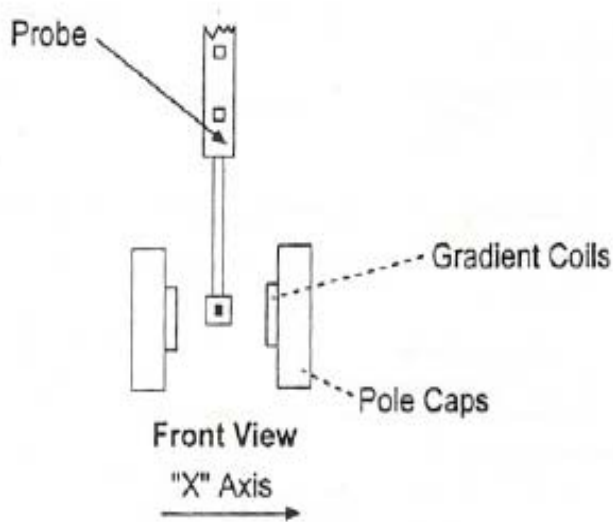


Illustration 2.6 Schematic of the AGM and sample holder

2.3.5. Cyclic Voltammetry (CV)

CV is a simple but convenient tool in electrochemistry used to determine oxidation and reduction potentials of chemicals. Reduction potentials for chemicals can be found in literature, but these values are reported at standard conditions of 25°C, 1 atm, and a pH of 7 in an aqueous solution. Table 2.5 gives the standard reduction potentials for Al and Mn, which are used in the synthesis attempts of AlMn nanoparticles, and reduction potentials of Fe and Pt are given for comparison. The potentials (E) are reported in voltage (V) and the lower the potential value the more difficult it is to reduce, therefore Fe and Pt are much easier to reduce than Al and Mn to their zero valence state. The reaction conditions of synthesis attempts to form AlMn nanoparticles differ from

standard conditions, so the values in table 2.5 most likely are not accurate for use in this research project. Therefore, CV is utilized to experimentally determine reduction

Half Reactions	E (V)
$\text{Pt}^{2+} + 2\text{e}^- \text{ ----> Pt}^0$	1.2
$\text{Fe}^{2+} + 2\text{e}^- \text{ ----> Fe}^0$	-0.44
$\text{Fe}^{3+} + 3\text{e}^- \text{ ----> Fe}^0$	-0.04
$\text{Mn}^{2+} + 2\text{e}^- \text{ ----> Mn}^0$	-1.18
$\text{Al}^{3+} + 3\text{e}^- \text{ ----> Al}^0$	-1.66

Table 2.5 Standard reduction potentials

potentials of Al and Mn precursors under the conditions present during the synthesis attempts of AlMn nanoparticles in this research. Knowing the correct reduction potentials for Al and Mn under the reaction conditions is useful determine which reducing agents are strong enough to work in the AlMn nanoparticle syntheses.

A CV experiment employs a three electrode system to obtain stable voltammograms, and the current along with the change of potential is measured. The three electrodes are a working electrode, a counter electrode, and a reference electrode. The working electrode potential is ramped linearly as scan rate (V/s) vs time (s), then when it reaches a set potential the working electrode potential is reversed and goes back toward the starting potential. The potential is measured between the reference electrode and the working electrode while the current is measured between the working electrode and the counter electrode. This collected data from the described sweep are plotted on a

graph as current (μA) vs potential (V). The forward scan of the sweep produces a current peak for the analyte being reduced in the range of the potential scanned. The current falls off as the concentration of the analyte is depleted. If the redox reactions of the analyte are reversible, then when the potential is reversed the analyte can be reoxidized and peaks are observed on the graph. The oxidation peaks usually have a similar shape to the reduction peaks on the graph. The analyte which is the sample being measured is used as the working electrode, and generally a noble metal is used as a counter electrode. Common reference electrodes are standard hydrogen electrode (SHE), saturated calomel electrode (SCE) and silver chloride electrode. Supporting electrolytes are needed to increase the conductivity of the solution.

In this dissertation, electrochemical characterizations were performed with a biopotentiostat (AFCBP1, Pine Instrument) with a three electrode electrochemical cell. The objective of CV experiments in this research was to determine the reduction potential of aluminum and manganese precursors in an organic solvent. By determining the reduction potential of the precursors in a solvent, an effective reducing agent could be chosen to ensure reduction of the precursors. Diphenyl ether was the solvent used as the medium for the CV experiments. Purification of the solvent by vacuum distillation was performed to ensure removal of all water and other impurities. CaH_2 (5 wt %) was added along with the solvent during distillation to help remove impurities by absorption. Experiments were done with only manganese precursors, only aluminum precursors, and with both aluminum and manganese precursors. A small amount of tetraethylammonium

tetrafluoroborate was added to the solvent as a background electrolyte to provide better conductivity. The experimental setup used a polished glassy carbon (GC) electrode with catalysts on it as the working electrode, and a Pt wire and a SCE were used as the counter and reference electrode, respectively. The solutions prepared for analysis contained 10^{-3} M of the electroactive species (precursor) and 0.1 M of the background electrolyte in 25 mL of solvent. N_2 was bubbled over the solution for 30 minutes before analysis to prevent any O_2 being present. The scan rate was between 10-50 mV/s for the experiments, and the data was expressed on a plot of voltage vs. time.

2.3.6 X-ray Photoelectron Spectroscopy (XPS)

XPS is a quantitative spectroscopic technique that measures the elemental composition, chemical state, and the electronic state of the elements that exist in a material. This analytical technique is important due to the capability of interpreting the surface chemistry of a material. The principle of XPS is based on Einstein's photoelectric effect. XPS requires an ultra high vacuum on the order of 10^{-9} torr, and a spectrum is obtained by irradiating the sample with a beam of either Al $K\alpha$ (1253.6 eV) or Mg $K\alpha$ (1486.6 eV) x-rays while simultaneously measuring the kinetic energy and the number of electrons that escape from the sample's surface. The binding energy of ejected electrons is characteristic of the elements and the oxidation states of the elements. The binding energy can be determined from equation 2.7.

$$(2.7) \quad BE = h\lambda - KE - \Phi$$

The parameters of equation 2.7 are defined as follows: BE is the binding energy of the electron emitted from one electron configuration within the atom, KE is the kinetic energy of the emitted electrons as measured by the instrument, $h\lambda$ is the energy of the incident x-ray photon, and Φ is the work function of the spectrometer.[70] From this equation, the instrument collects a spectrum based on binding energy. For this dissertation, survey scans were performed from 0-1000 eV to determine all of the elements present in the particles. Also, high resolution scans were collected on individual elements to determine their electronic states. An AXIS 165 XPS system was used in this dissertation research for surface analysis of nanoparticles.

CHAPTER 3

RESULTS AND DISCUSSION

This research investigated strategies to develop a wet chemical synthesis to produce ferromagnetic AlMn nanoparticles for use in high density magnetic recording devices. This chapter details the results of attempted particle syntheses and discusses these results including what was learned from each synthesis. During the course of this research hundreds of syntheses were performed, but providing details of each synthesis would be redundant and not beneficial to the reader. Since there are no known synthesis techniques that generate AlMn nanoparticles, the scope of this investigation is broad and cumbersome. The first section of this chapter chronicles successful synthesis techniques of well known transition metal nanoparticle systems of FePt and MnPt. These synthesis techniques were used as a starting point for AlMn nanoparticle synthesis attempts. Next, cyclic voltammetry (CV) experiments were performed to determine reduction potentials of organometallic precursors in organic solvents that were used as reaction mediums for AlMn nanoparticle synthesis attempts. Reduction potentials are useful to help determine a suitable reducing agent for Al and Mn precursors used in AlMn nanoparticle synthesis attempts. The remainder of this chapter details results from attempted synthesis routes of AlMn nanoparticles based on the reducing agent used in the synthesis. The reducing agents that were used during this research endeavor to produce AlMn nanoparticles include lithium triethylborohydride (superhydride, $C_6H_{16}BLi$), potassium (K), hydrogen (H_2), lithium aluminum hydride ($LiAlH_4$), and sodium (Na). The ideas for using these

reducing agents for AlMn syntheses are detailed, and the results from the synthesis attempts are provided followed by an explanation of what worked or what did not work. The next section provides results from synthesis attempts to produce AlMn(X) tertiary nanoparticle systems. Finally, the last section of this chapter details the results of trying to produce a core-shell structured particle with a core of AlMn with an iron oxide shell.

3.1 FePt and MnPt Nanoparticles

Transition metal nanoparticles have been studied extensively with many different synthesis routes and techniques to produce these nanoparticles in solution phase.

Transition metals that exhibited the tetragonal $L1_0$ phase in binary systems of FePt, CoPt, FePd, MnPt, and others which exhibit large uniaxial magnetocrystalline anisotropy and good chemical stability have been produced via wet chemical synthesis

routes.[10,11,53,54,65] This section chronicles synthesis techniques that produced FePt and MnPt nanoparticles because FePt is the most studied and well understood system

while the MnPt system includes Mn precursors that will be used in AlMn nanoparticle

synthesis attempts. FePt nanoparticles have been produced by three main chemical

synthesis routes that includes the reduction of Pt^{2+} and thermal decomposition of

$Fe(CO)_5$, superhydride reduction of Pt^{2+} and Fe^{2+} , and a diol reduction of Pt^{2+} and Fe^{2+} .

The size and composition of FePt nanoparticles can be controlled by several parameters.

Composition can be controlled by adjusting the molar ratio of the Fe and Pt precursors.

FePt synthesis using superhydride to reduce Pt^{2+} and Fe^{2+} yields particles with better

composition distributions due to fast nucleation during the reaction. Particle size can be

tuned from 3-10 nm by first growing 3 nm seed particles in situ then by adding more Fe and Pt reagents the particle size can be increased.[10,11,54,64,69] MnPt nanoparticles have been produced in similar routes as seen with FePt nanoparticles, but the magnetic phase of MnPt is an ordered L1₂ phase with the Mn:Pt stoichiometry of 1:3. MnPt exhibits composition dependent magnetic properties that range from antiferromagnetic (MnPt) to fully ferromagnetic (MnPt₃). MnPt₃ nanoparticles are fully transformed to its ferromagnetic L1₂ phase at an annealing treatment at 580°C.[65] Synthesis techniques of both FePt and MnPt nanoparticles that are detailed in this section are the foundation and starting point to produce a successful synthesis of AlMn nanoparticles.

Several synthesis of FePt nanoparticles were performed during this research project to serve as a guide and to compare to AlMn nanoparticle synthesis attempts, and the results from a synthesis of FePt is provided. This FePt synthesis was produced from the superhydride reduction of Pt²⁺ and Fe²⁺. The synthesis used 0.22 mmols of Fe(Cl)₂ and 0.2 mmols of Pt(acac)₂ as precursors and 15 mL of benzyl ether as the solvent. The precursors and solvent were added to the flask at the start of the reaction. The solution was heated to 100°C and 0.5 mmols of oleic acid and 0.5 mmols of oleylamine were injected as the surfactants. The solution was heated to 200°C and 1 mL of superhydride was injected as the reducing agent. The solution was heated to reflux (~ 260°C) for 30 minutes then cooled to room temperature. An observation that was noted during this synthesis was the solution turning dark black upon the addition of the reducing agent, superhydride, indicating the formation of particles. After the conclusion of the reaction

an isolation and purification process must be done before storing the particles for analysis. For these reactions the standard washing and cleaning technique was used (see section 2.2.1). After ethanol addition to the reaction product, particles immediately began to settle down to the bottom and after several hours most all of the particles settled to the bottom of the beaker. There was a definite separation of a precipitate which was dark black at the bottom of the beaker and the supernatant which was mostly clear above the precipitate. Many particles were re-dispersed using hexane and surfactants which was indicated by the dark black supernatant containing the re-dispersed FePt nanoparticles.

The as-made FePt nanoparticles were analyzed, and then the particles were subjected to a salt annealing at 600°C which prevented sintering while allowing the disordered face centered cubic particles to fully transform to the face centered tetragonal $L1_0$ phase. Figure 3.1 shows a TEM image and an electron diffraction pattern of the annealed particles provided by Dr. Shishou Kang. The TEM image shows monodispersed 8 nm FePt nanoparticles with little to no sintering from the annealing procedure. The electron diffraction pattern taken on the TEM shows the diffraction rings from the particles. Figure 3.2 shows a high resolution TEM image with a histogram and of Fourier transform from the fully transformed 8 nm FePt particle which was also provided by Dr. Shishou Kang. The image clearly shows that no sintering occurred during the salt annealing. The vertical line on the particle is a histogram taken to determine the d-spacings from the visible lattice fringes. The box in the upper right

corner shows the d-spacings generated from the histogram and gives a value of 3.71 nm across 10 peaks. This gives an average d-spacing of 0.3711 nm which corresponds to the {001} plane in the tetragonal FePt structure.

Figure 3.3 shows two XRD spectrums of as made FePt and FePt that was salt annealed at 600°C. The as made scan shows a broad peak around $41^\circ 2\theta$ that corresponds to the {111} plane in the FePt system. This spectrum confirms that the as made FePt nanoparticles have the chemically disordered face centered cubic structure. The XRD scan from the salt annealed FePt shows the superlattice peaks of {001}, {110}, {111}, {200}, {002}, and {201}. This scan confirms the particles were transformed to the face centered tetragonal $L1_0$ phase.

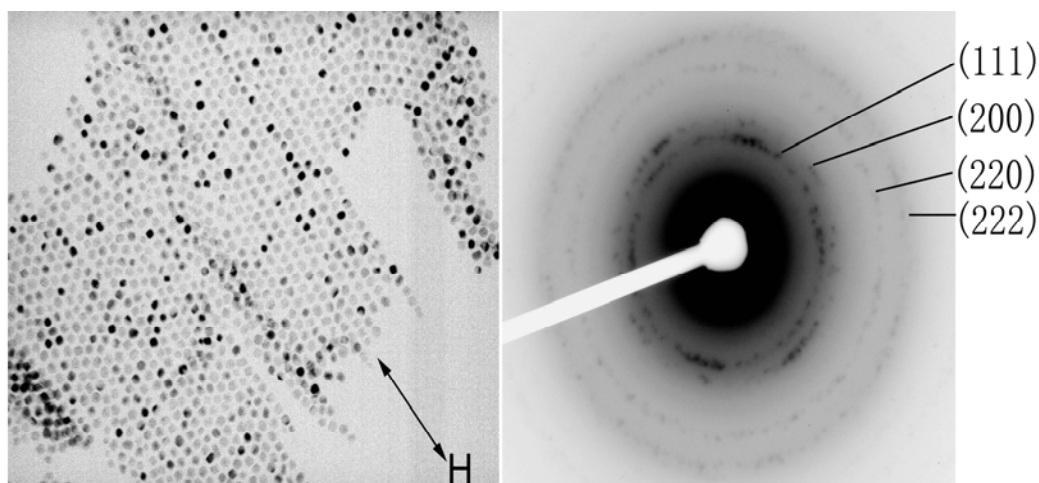


Figure 3.1 TEM image (left) and electron diffraction pattern (right) of FePt nanoparticles

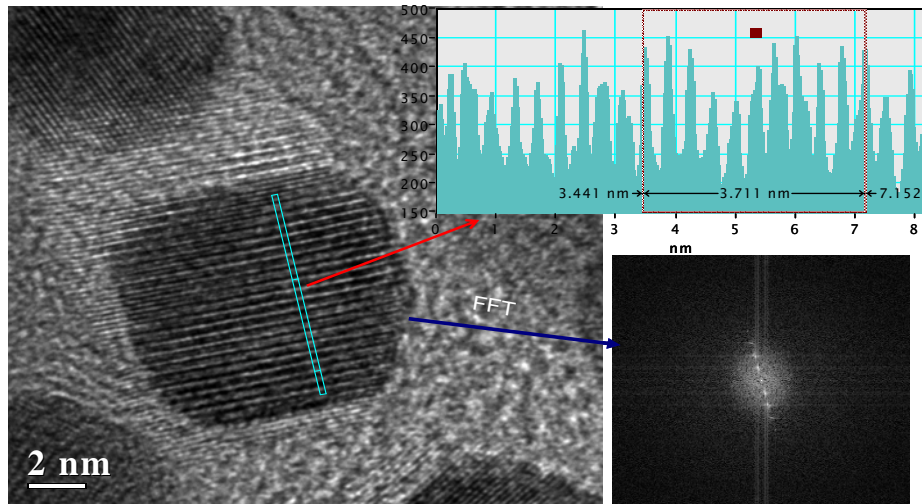


Figure 3.2 High resolution TEM image, histogram, and fourier transform of FePt nanoparticles

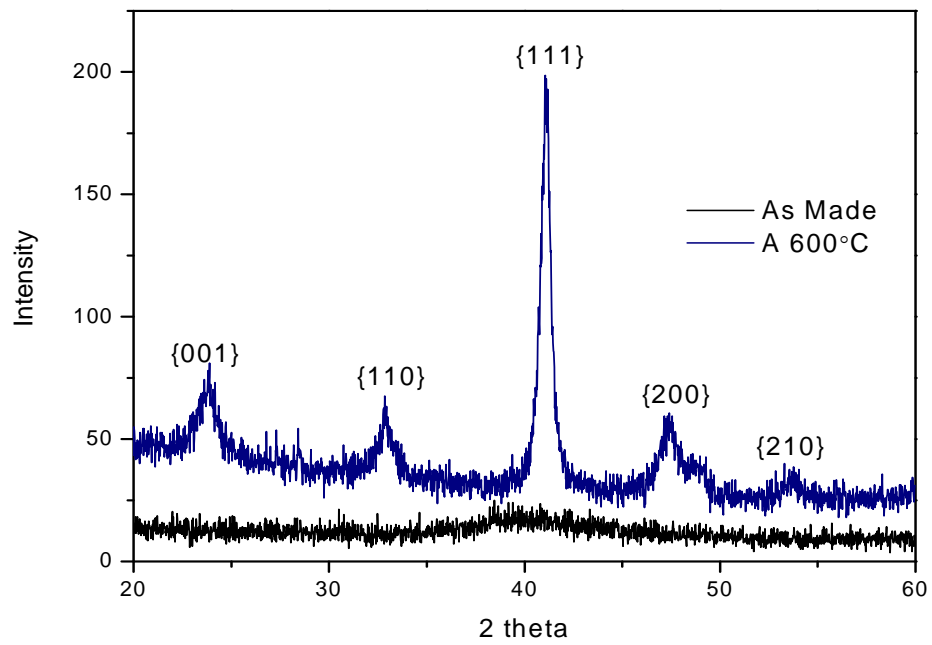


Figure 3.3 XRD spectrum of FePt nanoparticles as made and annealed at 600°C

Scherrer analysis performed on the {111} peak of both spectrum confirms the particle size of approximately 8 nm seen in the TEM images.

MnPt nanoparticles were produced by a high temperature reduction of 0.5 mmols Pt(acac)₂ and 0.5 mmols of Mn(acac)₂ with 1 mmols of 1,2-hexadecandiol in 10 mL of dioctyl ether as the solvent. The solution was heated to 100°C and 0.5 mmols of oleic acid and 0.5 mmols of oleylamine were injected as the surfactants. The solution was heated to reflux (~ 298°C) for 30 minutes then cooled to room temperature. During the reaction the solution turned black around 170°C which indicated that particles had been formed.

The isolation and purification technique from MnPt and MnO reactions was used for the reaction product from this synthesis (see Section 2.2.3). A brown precipitate was formed at the bottom of the centrifuge tube while the supernatant was dark black after the first step of this technique indicating the particles were dispersed in the supernatant. This brown sediment was kept for analysis and the particles which had a dark black color were collected for analysis and both were stored in hexane. Figure 3.4 shows the XRD spectrum from the as made MnPt₃ nanoparticles. The {111} and {200} peaks are indexed and proves that the as made MnPt₃ nanoparticles have the chemically disordered fcc structure as anticipated. Scherrer analysis was performed on the {111} peak to calculate the average particle size which was found to be 5.26 nm. SEM EDS was done to obtain the composition of the particles and the average composition was Mn₂₃Pt₇₇.

This confirms that even though the Mn:Pt precursor ratio was equal, the Mn:Pt particle stoichiometry was approximately 1:3.

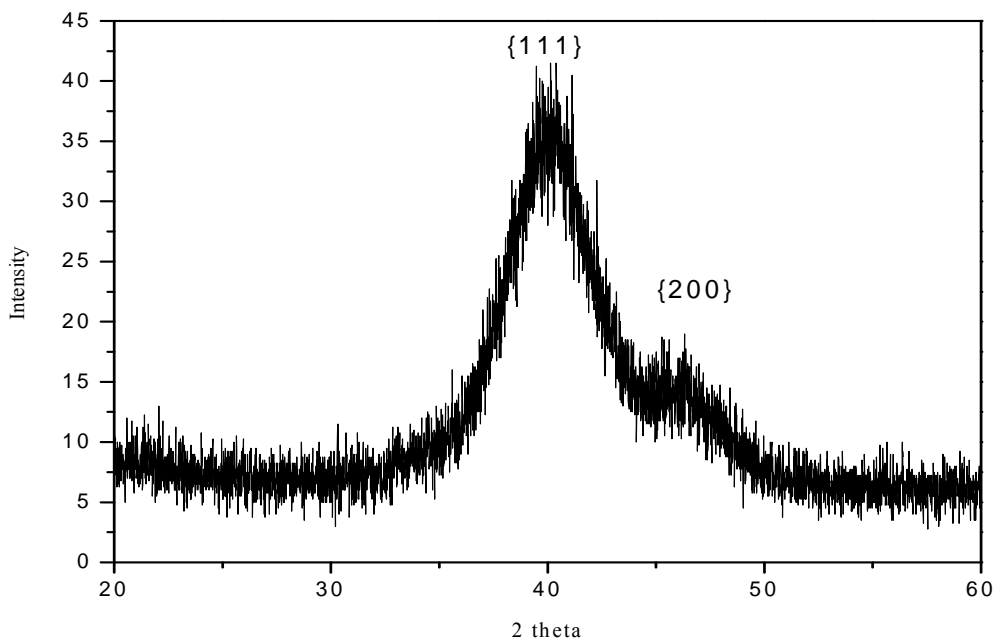


Figure 3.4 XRD spectrum of as made MnPt₃ nanoparticles

Figure 3.5 shows a TEM image of the MnPt₃ nanoparticles which shows that the particles are spherical with broad sizes ranging from about 3-8 nm. This image further corroborated that Scherrer analysis on the XRD spectrum correctly determined that the average particle size was around 5 nm. Figure 3.6 shows a high resolution TEM image and a histogram taken along the lattice fringes of the particle to determine the d-spacing of the plane shown. The value of the d-spacing obtained from the histogram was

approximately 0.227 nm which corresponds the d-spacing from the {111} plane in MnPt₃ nanoparticles. This collection of evidence proved that fcc MnPt₃ nanoparticles with an average size of 5 nm were obtained from this synthesis.

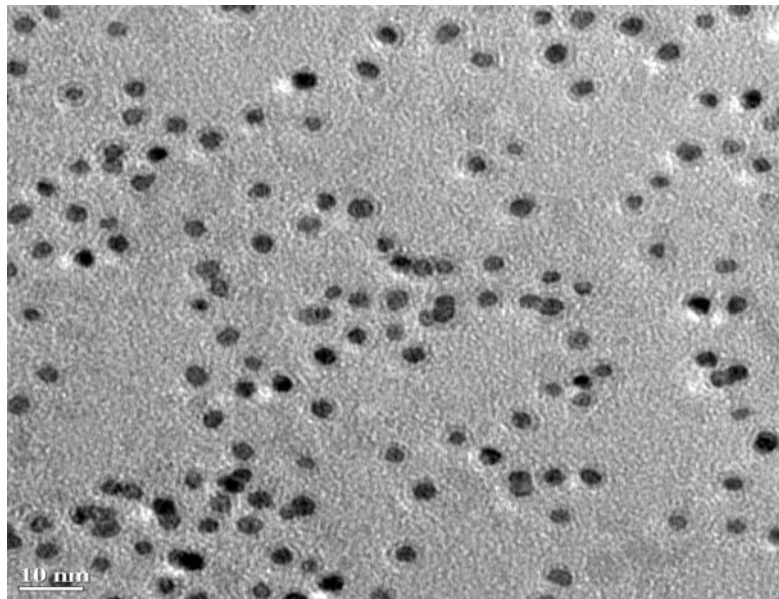


Figure 3.5 TEM image of MnPt₃ nanoparticles

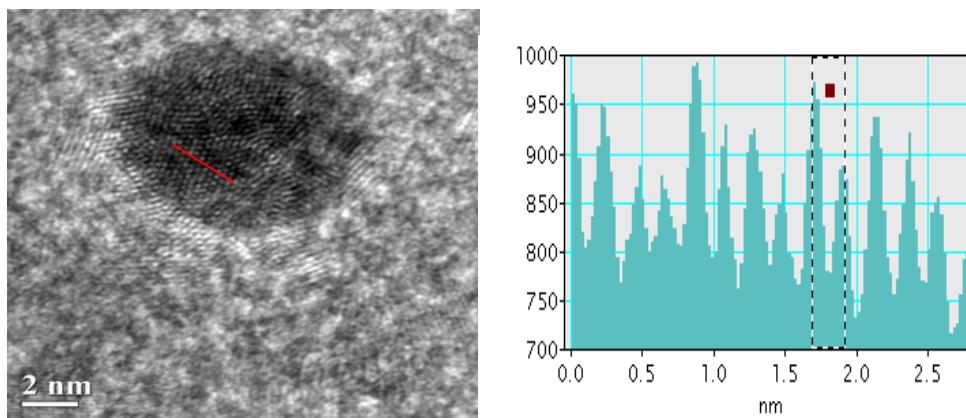


Figure 3.6 TEM image with histogram of MnPt₃ nanoparticles

MnPt nanoparticles have also been synthesized by using $\text{Mn}_2(\text{CO})_{10}$ as the Mn precursor with similar results as the synthesis detailed above. The average diameter of the MnPt nanoparticles depended on the Mn precursor used in the synthesis. $\text{Mn}_2(\text{CO})_{10}$ gave particles with an approximate diameter of 5 nm, while $\text{Mn}(\text{acac})_2$ yielded particles with an approximate diameter of 2 nm. These results proved that both $\text{Mn}_2(\text{CO})_{10}$ and $\text{Mn}(\text{acac})_2$ are suitable to produce nanoparticles via a wet chemical synthesis. Also, $\text{Mn}(\text{acac})_2$ was reduced with a mild reducing agent in 1,2-hexadecandiol.

The syntheses of both FePt and MnPt presented in this section were used as models for AlMn nanoparticle synthesis attempts. Also, general knowledge gained from conducting these reactions such as parameters affecting size and composition were applied to AlMn synthesis attempts. Specifically, the MnPt system provided the fact that Mn precursors are easily reduced and suitable for producing metal nanoparticles. This gives optimism that AlMn nanoparticles can be produced via a wet chemical synthesis.

3.2 Reduction Potentials using Cyclic Voltammetry (CV)

After several attempts to produce AlMn nanoparticles using different combinations of precursors, solvents, surfactants and reducing agents there were no successful synthesis found. Since the AlMn syntheses had been modeled after FePt and MnPt synthesis techniques and literature shows that Al and Mn are more difficult to reduce than Fe or Pt, cyclic voltammetry was used to determine reduction potentials and a suitable reducing agent for Al and Mn. Table 2.5 gives the reduction potentials of Pt^{2+} , Fe^{2+} , Fe^{3+} , Al^{3+} , and Mn^{2+} in an aqueous solution, but these reactions were done using

organic solvents as the medium, thus it would be helpful to know the reduction potentials of organometallic precursors in the organic solvent used in the reaction to better predict an adequate reducing agent. The question that needs to be answered is whether or not superhydride is strong enough to reduce the Al and Mn precursors, most are in oxidized states of either 2^+ or 3^+ , to their zero valence state. It is also possible that superhydride is capable of reducing the precursors to their metal state followed by oxidation upon contact with the atmosphere yielding amorphous oxides. Another possibility is that kinetically Al and Mn nuclei are not compatible to form a crystalline phase under the reaction conditions. To answer the question of finding a strong enough reducing agent, cyclic voltammetry, a tool in electrochemistry that experimentally determines reduction and oxidation potentials of chemicals, was used during this research. Reduction potentials were examined experimentally with CV experiments to determine how strong of a reducing agent is needed to successfully reduce the Al and Mn precursors used in the synthesis attempts to produce AlMn nanoparticles. The CV experiments were done in diphenyl ether as the solvent which was purified by vacuum distillation with 5 wt. % CaH_2 to remove all traces of water prior to use in each experiment. The solutions used in the experiments contained 10^{-3} M of the electroactive species (precursor) and 0.1 M of the background electrolyte (tetraethylammonium tetrafluoroborate) in 25 mL of diphenyl ether. N_2 was bubbled over the solution to ensure an inert atmosphere for the experiments. CV experiments that were performed included diphenyl ether to determine a potential window, $\text{Al}(\text{acac})_3$, $\text{Mn}(\text{acac})_2$, $\text{Pt}(\text{acac})_2$, and $\text{Fe}(\text{acac})_2$.

The first CV experiment was done with only diphenyl ether and no electroactive species to determine the potential window of the solvent. The voltage is driven negatively until the point where the phenyl ether is being reduced and the current falls off dramatically. A potential window must be determined for the solvent because past this point it would be impossible to tell if the electroactive species or the solvent is being reduced. The rest of the CV experiments were done on Al and Mn precursors to help determine reduction potentials and therefore determine the proper reducing agent for AlMn nanoparticle syntheses. Also, CV experiments were done on other metal precursors as a reference when modeling synthesis techniques toward AlMn syntheses. Figure 3.7 shows the data graphed as current (μA) vs. potential (V) of phenyl ether and the electrolyte which shows the potential window to be around -1.7 V. There are no peaks associated with reduction on the negative sweep which makes sense because there is no species that should be getting reduced. This is not a particularly large potential window considering the metals that were used for this research are Al^{3+} and Mn^{2+} which have values from literature of -1.71 V and -1.18 V, respectively. Therefore, it may not be possible to determine a reduction potential for Al precursors in diphenyl ether using CV analysis since the potential window of the solvent and the reduction potential of Al^{3+} are virtually identical. Figure 3.8 show the graph of the CV experiment with $\text{Al}(\text{acac})_3$ and the electrolyte in diphenyl ether. There is no reduction peak observed in the negative sweep which indicates that Al^{3+} was not reduced in the potential window of the solvent.

This confirms the suspicion that it was possible that the Al precursor would not be reduced in the solvent's potential window.

Figure 3.9 shows the graph of the CV experiment with $\text{Mn}(\text{acac})_2$ and the electrolyte in diphenyl ether. This graph shows a broad peak around -1.4 V which indicates reduction of the Mn in the solvent. This experimental value obtained is close to the literature value of -1.18 V, but CV analysis indicates the Mn is slightly more difficult to reduce in diphenyl ether than in water.

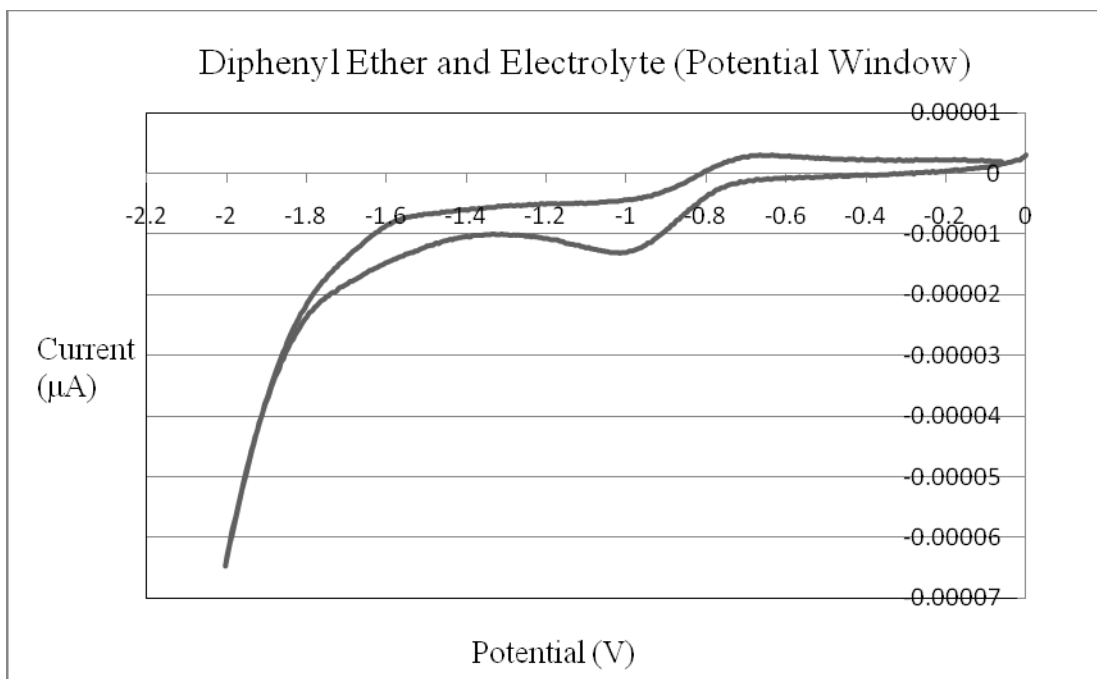


Figure 3.7 Graph to determine the potential window of diphenyl ether

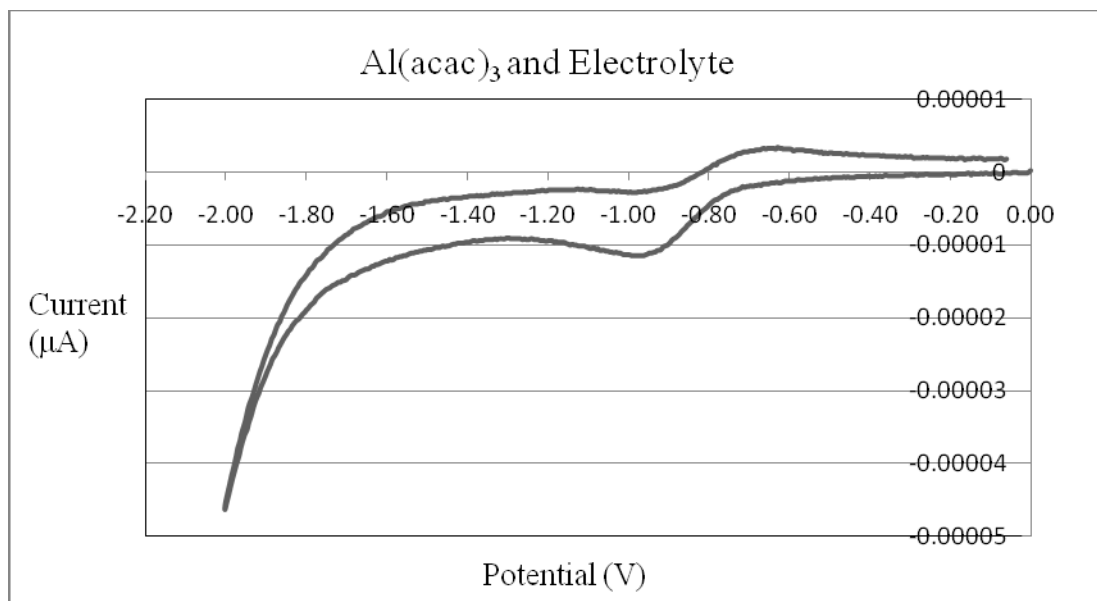


Figure 3.8 Graph of CV analysis of $\text{Al}(\text{acac})_3$ in diphenyl ether

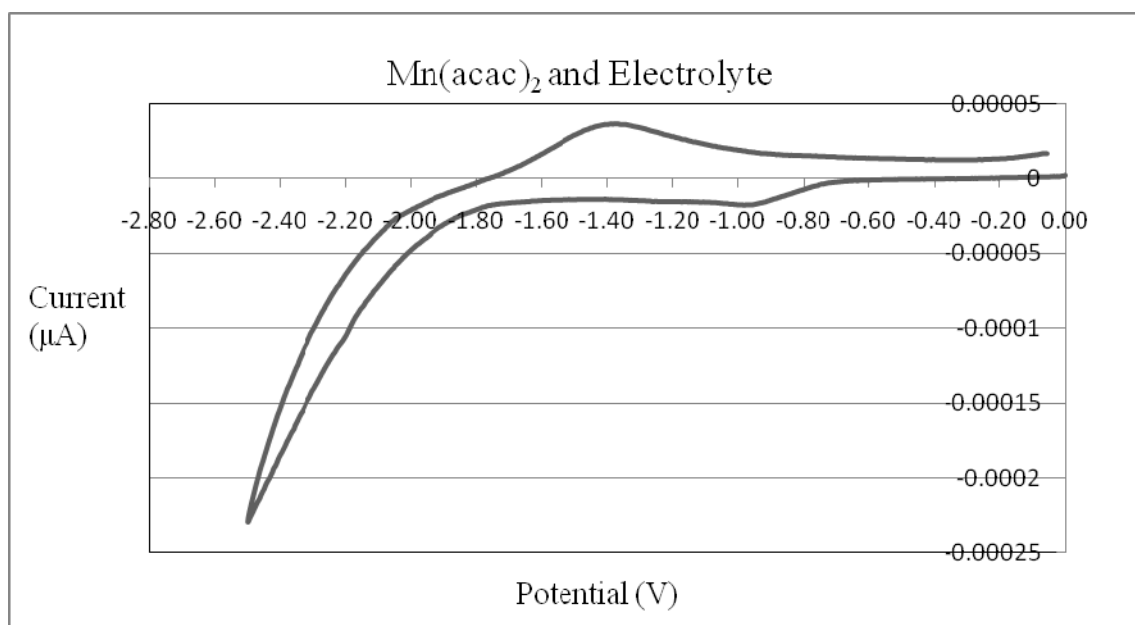


Figure 3.9 Graph of CV analysis of $\text{Mn}(\text{acac})_2$ in diphenyl ether

Figure 3.10 shows the graph of $\text{Pt}(\text{acac})_2$ with the electrolyte in diphenyl ether. There is a reduction peak that occurs around -0.7 V. This value is larger than the value reported in literature and like Mn it is more difficult to reduce in the organic solvent diphenyl ether. The peaks that occur on the bottom sweep back toward zero are oxidation peaks which confirm that indeed the Pt was reduced. Figure 3.11 shows the graph of $\text{Fe}(\text{acac})_2$ with the electrolyte in diphenyl ether. A reduction peak is observed around -0.8 V which is larger than the literature value. The CV analysis yielded reduction potentials larger than literature values for each metal which are reported in aqueous solutions while these values were obtained using diphenyl ether as the medium. This trend was seen consistently throughout the CV analysis.

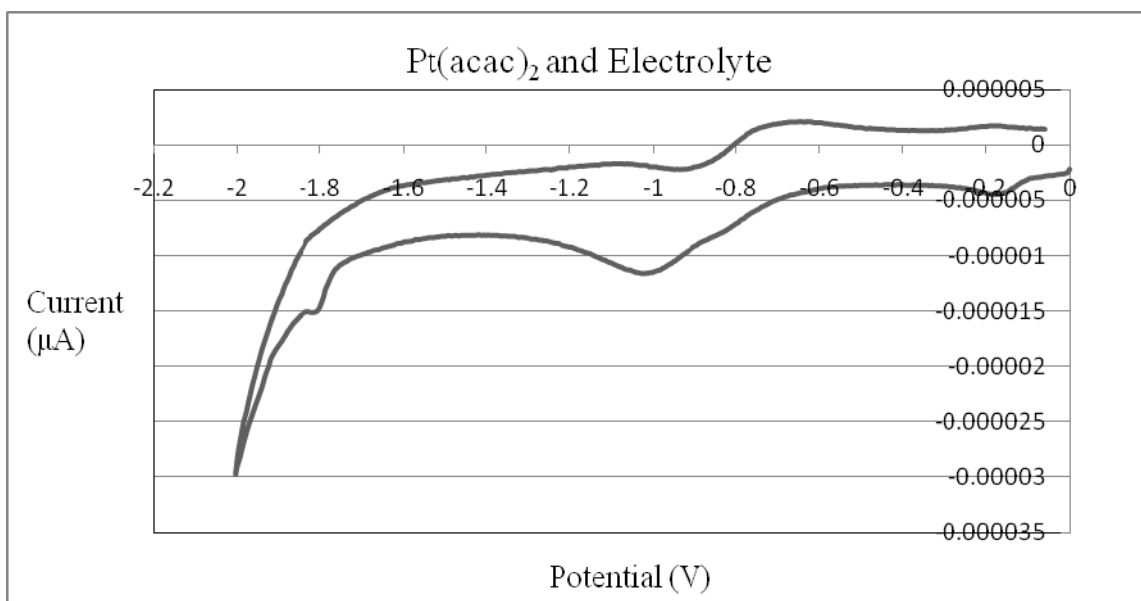


Figure 3.10 Graph of CV analysis of $\text{Pt}(\text{acac})_2$ in diphenyl ether

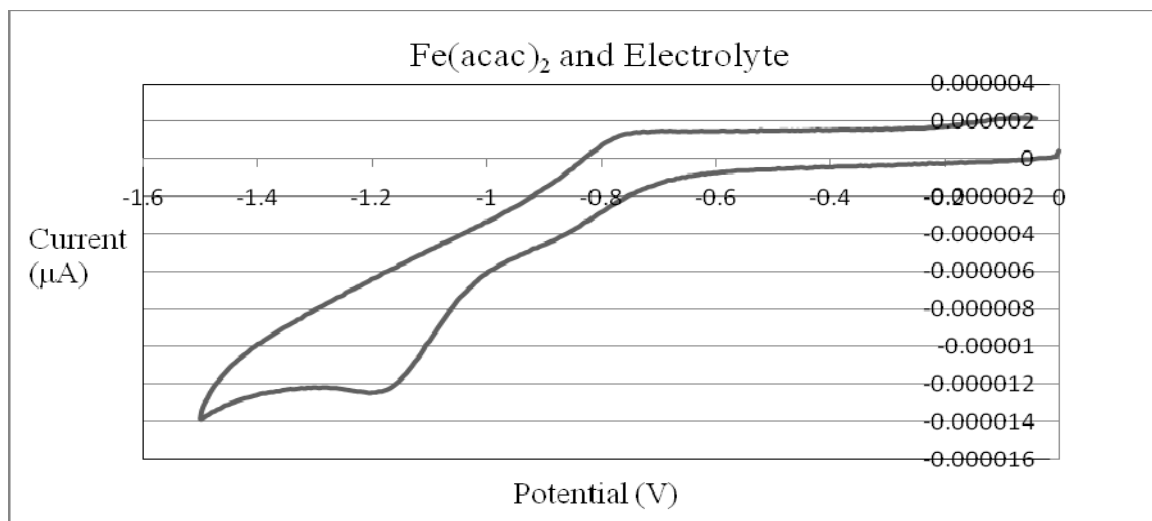


Figure 3.11 Graph of CV analysis of Fe(acac)₂ in diphenyl ether

The results of the CV experiments gave the experimental reduction potentials of all the metal precursors that were analyzed except Al(acac)₃. The most important metals for this research are Al and Mn, and a reduction potential for Mn(acac)₂ was determined to be around -1.4 V. A reduction potential was unable to be determined for Al(acac)₃ because the potential window of the diphenyl ether was too small to reduce the Al. A common theme produced from these experiments was that all of the experimentally determined reduction potentials were larger than their literature values. Based on that logic, the reduction potential of Al will be larger than its literature value of -1.66 V. It can be concluded from the CV experiments that Mn precursors will be able to be reduced in an organic solvent by most all reducing agents including superhydride. Also, it can be concluded that a reducing agent must have a potential greater than -1.70 V to reduce Al

precursors. Strong reducing agents such as Na, K, LiAlH₄, and possibly superhydride will be required to reduce Al precursors.

3.3 AlMn Synthesis Attempts using Superhydride

At the start of this research project, the first synthesis attempts to produce AlMn nanoparticles followed a similar route as a wet chemical synthesis of FePt nanoparticles using organometallic precursors in a high temperature solvent with a strong reducing agent. Superhydride (lithium triethylborohydride) is a fairly strong reducing agent with a reduction potential of approximately +2.2 V, and on paper it was assumed that it would be strong enough to reduce both Al and Mn precursors. Superhydride has been a very successful reducing agent in producing FePt nanoparticles, so it was used in the first synthesis attempts to create AlMn nanoparticles. The synthesis attempts of AlMn nanoparticles using superhydride as the reducing agent are detailed in the following section.

Synthesis 1 using Superhydride

The first synthesis done in this research project used Al(acac)₃ and Mn(acac)₃ as precursors in diphenyl ether as the solvent. The problem with these precursors is the Mn(acac)₃ is black in color and when it is put into the solution, the entire solution turns black. The problem with the solution being black is that it is impossible to observe if particles are formed during the reaction because the indicating factor of particle formation is the solution turning black. After this synthesis Mn(acac)₃ was never used again as a precursor instead Mn(acac)₂ and Mn₂(CO)₁₀ were used as precursors.

Synthesis 2 using Superhydride

Another synthesis used 0.5 mmols of $\text{Al}(\text{acac})_3$ and 0.5 mmols of $\text{Mn}(\text{acac})_2$ as precursors in 25 mL of diphenyl ether as the solvent. The solution was heated to 100°C and 0.5 mmols of oleic acid and 0.5 mmols of oleylamine were injected as the surfactants. The solution was heated to 200°C and 2.5 mL of 2 M superhydride in THF was added as the reducing agent to the solution by injection. The solution started off light brown at the start of the reaction and after the injection of the superhydride the solution turned darker brown but not black. The solution was heated to reflux ($\sim 260^\circ\text{C}$) for 30 minutes but the solution never turned black indicating that no metal nanoparticles had been produced. The solution was cooled to room temperature and ethanol was added to precipitate particles from the reaction product. After allowing the solution to sit overnight, particles had not precipitated out to the bottom. There was no noticeable line between the precipitate and the supernatant as seen during FePt syntheses.

The standard isolation and purification technique was used for this reaction product (Section 2.2.1). No particles were re-dispersed and the precipitate was dried and stored in hexane for analysis. Figure 3.12 show the XRD spectrum from the precipitate formed from the reaction. The large broad peak around $20^\circ 2\theta$ indicates amorphous material in the precipitate. The small broad peaks around 45° and $66^\circ 2\theta$ were indexed as the {400} and {440} peaks of Al_2O_3 , respectively. SEM EDS was done to determine composition of Al and Mn present in the reaction precipitate which was $\text{Al}_{11}\text{Mn}_{89}$. XPS was done on this sample to determine the oxidation states on the surface of the particles.

Figure 3.13 shows the survey scan done on the sample which shows all the elements that are present in the sample which includes C, O₂, Mn, Si (from the substrate), and Al. Figure 3.14 shows the high resolution scan of the Al 2p peak. The peak was present around 76 eV which indicates the presence of Al in the Al₂O₃ form. Figure 3.15 shows the high resolution scan of the Mn 2p peaks. The peaks were present at 654 and 642 eV which suggests the presence of various oxide states of the Mn. The presence of Al in the Al₂O₃ form from XPS analysis confirms the XRD results which had peaks indicating Al₂O₃ present in the reaction product from this synthesis confirming that this synthesis was unsuccessful in producing AlMn nanoparticles.

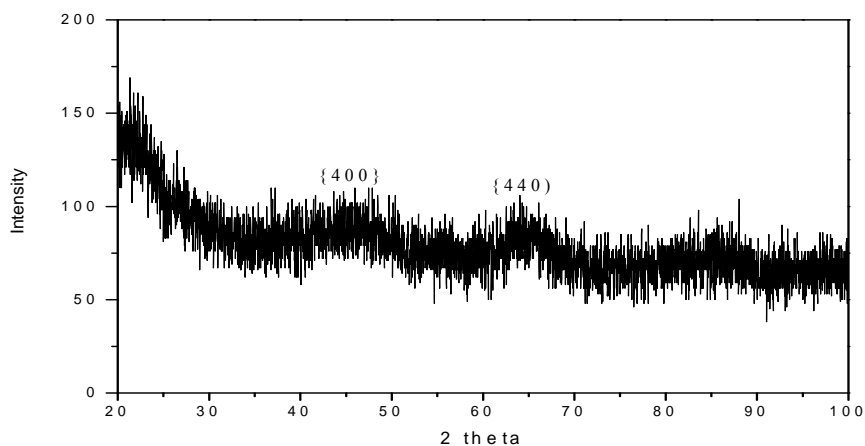


Figure 3.12 XRD spectrum from AlMn synthesis using superhydride indexed as Al₂O₃ and amorphous material

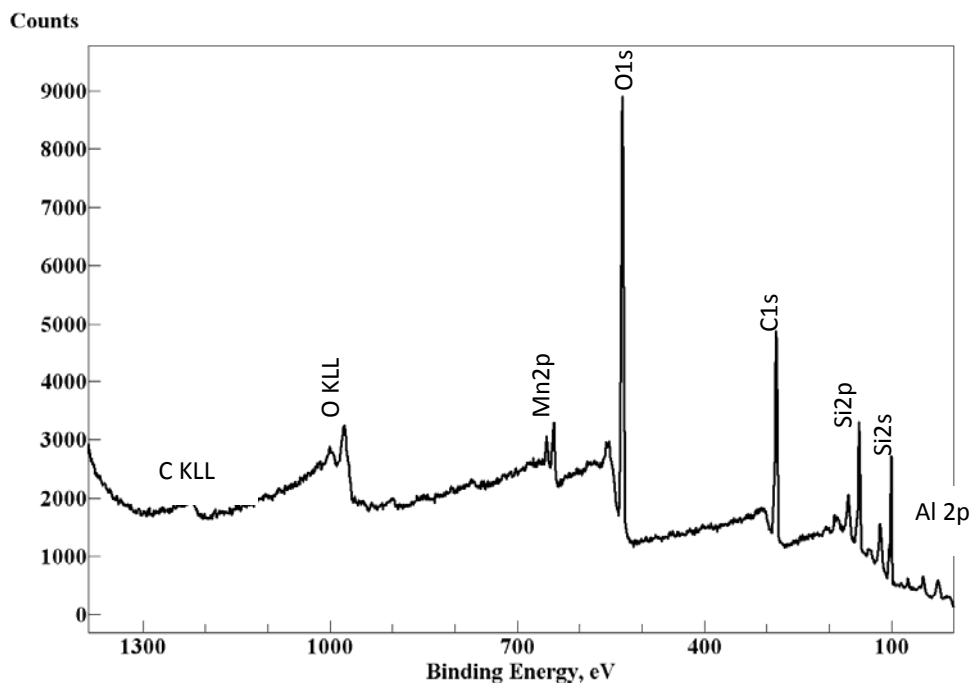


Figure 3.13 XPS survey scan of the particles generated from AlMn synthesis using superhydride

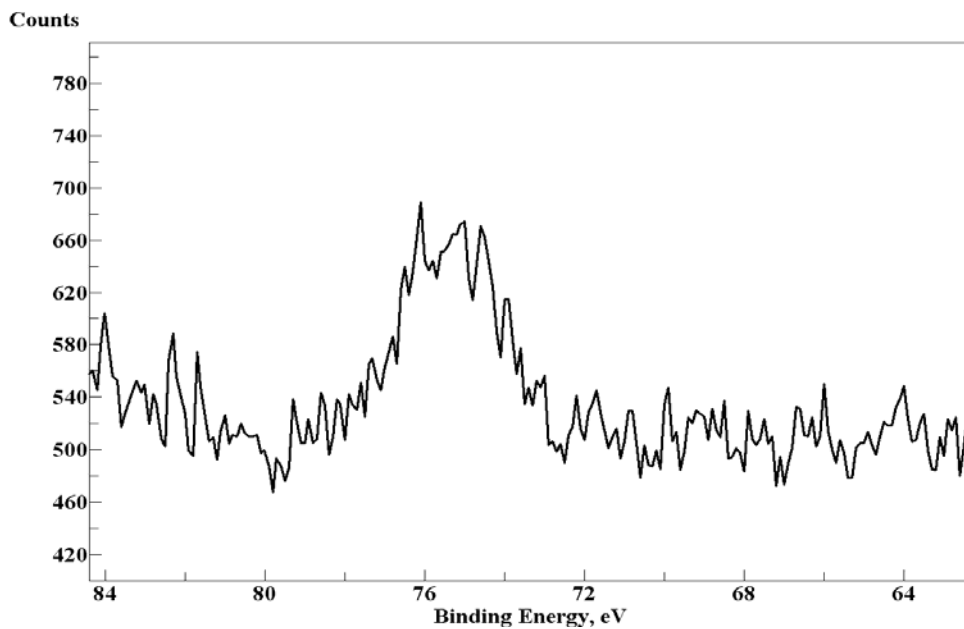


Figure 3.14 High resolution XPS scan of Al 2p and the peaks indicate the presence of Al_2O_3

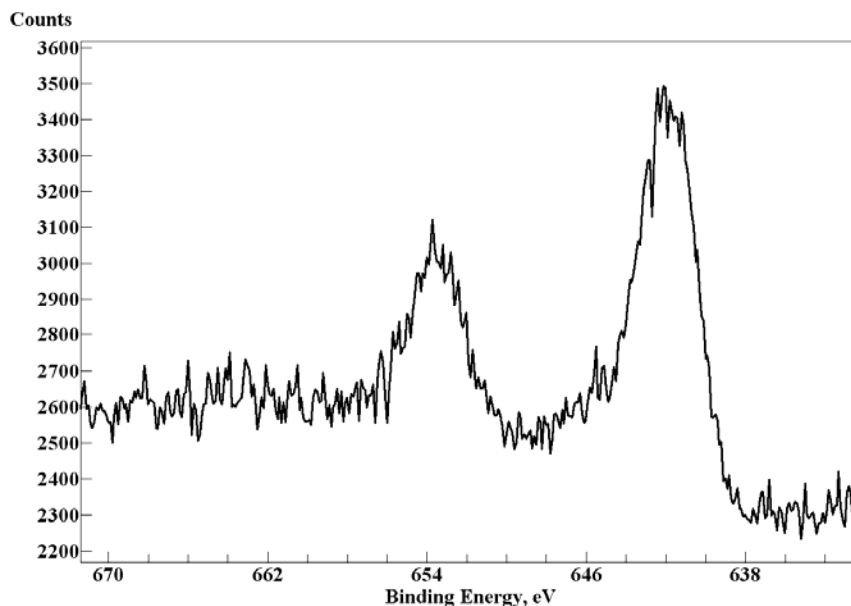


Figure 3.15 High resolution XPS scan of Mn 2p. Position of the peaks suggest the presence of various oxide states.

Several other synthesis attempts were done using superhydride as the reducing agent with different solvents such as TOA, benzyl ether, and dioctyl ether with different combinations of precursors of Al and Mn but all were unsuccessful. The common observation that was noticed from these syntheses is that the solution never turned black during the reaction which means that no metal particles were formed. The resulting precipitates from these reactions were all brown in color and not black most likely indicating the formation of oxides. It was found that using equimolar amounts of Al and Mn precursors always resulted in an overwhelming percentage of Mn according to SEM EDS. Since the τ phase occurs around $\text{Al}_{50}\text{Mn}_{50}$ the amount of precursors was varied to

try and achieve compositions in the “sweet spot” in the range of 50-59 at % Mn in AlMn particle compositions. The conclusion from these synthesis attempts was that superhydride was not strong enough to reduce the Al and Mn precursors properly to form AlMn nanoparticles. A stronger reducing agent must be employed to ensure the reduction of the Al and Mn precursors such as LiAlH_4 , Na, or K.

3.4 AlMn Synthesis Attempts using Potassium (K)

Potassium (K) was used as a reducing agent for synthesis attempts to produce AlMn nanoparticles. K is a strong reducing agent with a potential of +2.92 V which is strong enough to reduce all of the Al and Mn precursors. K must be handled carefully, because it is a strong irritant, reacts violently with water, and is flammable. K is like Na because they both are in solid form and using a solid reducing agent presents mass transfer issues in the reaction. All the precursors are dissolved in the solution before the reducing agent is added into the reaction, so the solid reducing agent must be soluble with the solvent and have a melting point below the solvent's boiling point. K has a melting point of 64°C and is soluble in most organic solvents. Also, K is highly reactive with organic materials and organometallic compounds. Attempted synthesis to produce AlMn nanoparticles using K as the reducing agent is reported in this section.

Synthesis 1 using K

The first synthesis to note used 1 mmol $\text{Al}(\text{acac})_3$ and 0.2 mmols of $\text{Mn}_2(\text{CO})_{10}$ as precursors in 20 mL of diphenyl ether as the solvent with 2.5 mmols K as the reducing agent. The K visibly melted in the solution around 65°C. The solution was heated to

100°C and 0.2 mL of oleic acid was injected as the surfactant. Then, the solution was heated to reflux (~260°C) for 30 minutes. The solution started out yellow in color and turned red around 200°C, and right before reflux the solution turned orange. During reflux the solution remained dark reddish orange and never turned black during reflux. This indicated that no particles were formed during this reaction. The solution was cooled to room temperature and ethanol was added to see if anything would precipitate out. No precipitate ever formed in the beaker containing the reaction product and ethanol, so it was determined that this reaction was a failure.

Synthesis 2 using K

The next attempted synthesis used 1 mmols Al(acac)₃ and 0.2 mmols Mn₂(CO)₁₀ in 20 mL of TOA as the solvent with 2.5 mmols K as the reducing agent. Again, the K visibly melted in the solution around 65°C. The solution was heated to 100°C and 0.2 mL oleic acid and 0.2 mL oleylamine was injected as the surfactants. Then, the solution was heated to reflux (~368°C) for 30 minutes. The reaction proceeded similarly to the first reported synthesis. The solution started out yellow in color and turned red around 200°C. During reflux the solution turned dark reddish orange but the solution was transparent, and it was obvious that no particles were formed. The solution was cooled to room temperature and ethanol was added to the reaction product but no precipitate was formed. This synthesis was also a failure.

Several other reactions were done using K as the reducing agent with the parameters being changed to try and find a compatible synthesis with K. The solvents

that were tried included octyl ether, benzyl ether, DMF, and pyridine along with diphenyl ether and TOA reported in this section. None of the reactions using K generated any indication of particles during the synthesis or no precipitate after the reaction. For this reason there is no analysis reported for any of the reactions. It is unknown why K is not a compatible reducing agent for an organometallic AlMn nanoparticle synthesis. K melted around 65°C in every reaction and appeared to be soluble in the organic solvents. K is one of the strongest reducing agents and is definitely strong enough to reduce all Al and Mn precursors, but it is not useful in synthesizing AlMn nanoparticles.

3.5 AlMn Synthesis Attempts using Hydrogen (H₂)

After many failed synthesis attempts to produce AlMn nanoparticles a new approach was taken by producing oxide particles from a wet chemical synthesis and then subjecting the particles to H₂ in a tube furnace to try and reduce the particles to AlMn. The wet chemical synthesis techniques were modeled after a cobalt ferrite synthesis and an iron oxide synthesis. These synthesis yielded particles in a powder form and then they were placed in a tube furnace and subjected to H₂ in hopes of reducing the particles to AlMn. The synthesis attempts and subsequent heat treatments are detailed in the following section.

Synthesis 1 using H₂

The first synthesis attempt to produce a precursor of a form of Al_xMn_xO_x used 0.25 mmols of Al₂O₃ and 0.25 mmols of Mn(acac)₂ as precursors with 1 mmol of 1,2-hexadecandiol as the reducing agent in 20 mL of diphenyl ether as the solvent. The

solution was heated to 100°C and 0.5 mmols of oleic acid and 0.5 mmols of oleylamine were injected as the surfactants. The solution was heated to reflux (~ 260°C) but as the temperature got to approximately 200°C the solution turned reddish orange in color and began to solidify into a gel like substance. Formation of this gel like substance is an indication of aluminates or other forms of aluminum oxides. The reaction was aborted and no particles were obtained. Several other reactions were attempted with different solvents and reducing agents, but the results were similar to the synthesis detailed above. After these failed synthesis attempts, a different synthesis route was employed which was modeled after synthesis techniques used to produce cobalt ferrites and iron oxides. This synthesis used 10 mmols of Al₂O₃ and 10 mmols of Mn(acac)₂ as precursors with 20 mmols of 1,2-hexadecadiol as the reducing agent in 250 mL of ethanol as the solvent. The precursors, reducing agent, and solvent were added to a 1000 mL beaker with a magnetic stir bar. The beaker was placed onto a hot plate for the heat source. The solution was stirred for 20 minutes at room temperature to ensure a homogenous mixture, then 1 mL of oleic acid and 1 mL oleylamine was added as surfactants. The solution was heated slowly to reflux (~ 78°C) for 20 minutes. The solution started out light brown in color and during reflux it turned dark brown indicating a reaction occurred. The solution was cooled to room temperature. The particles were separated from the solution by vacuum filtration and the precipitate was allowed to dry overnight under atmosphere conditions. The particles obtained were in powder form and analyzed before being subjected to any heat treatments.

Figure 3.16 shows the XRD spectrum of the particles before heat treatment. The particles were indexed to Mn_3O_4 and figure 3.16 shows the peaks of {112}, {103}, {211}, {004}, {220}, {105}, {312}, {303}, {321}, {224}, {314}, and {413}. Scherrer analysis performed on the most intense peak {211} in the XRD spectrum resulted in approximately 50 nm particles of Mn_3O_4 . This was not the outcome that was expected from the reaction. There were no peaks from any form of $Al_xMn_xO_x$ or Al_xO_x which was the goal from the synthesis, but SEM EDS showed the presence of both Al and Mn in the precipitate yielded from the synthesis. SEM EDS showed the presence of both Al and Mn in the ratio of 47:53 at %, respectively. This evidence combined with the XRD spectrum concludes that the precipitate contains crystalline Mn_3O_4 and other amorphous Al and/or Mn oxides. Even though the precipitate was not the ideal precursor to try and produce AlMn particles by using H_2 as the reducing agent, experiments were performed using the precipitate. By performing experiments using H_2 as the reducing agent on this precipitate, it can be concluded if this technique is a viable option to reduce Mn_3O_4 and therefore possibly $Al_xMn_xO_x$ to produce AlMn particles.

The tube furnace reactor setup is shown in illustration 3.1. Samples (~ 0.5 g) of the powder precipitate yielded from the solution phase synthesis was placed into a quartz tube furnace and sealed from atmospheric conditions. N_2 was run through the furnace for 20 minutes to flush out O_2 and other gases that could be present and ensure an inert atmosphere. The temperature was increased to $450^\circ C$ and the gas was switched to ultra high purity H_2 for 1 hour as the reduction step. Then, the temperature was cooled to

50°C and the gas was switched to N₂ contained 1000 ppm of O₂ for 2 hours as a passivation step. A passivation step was done to prevent possible oxidation when the sample became exposed to atmospheric conditions. The sample was cooled to room

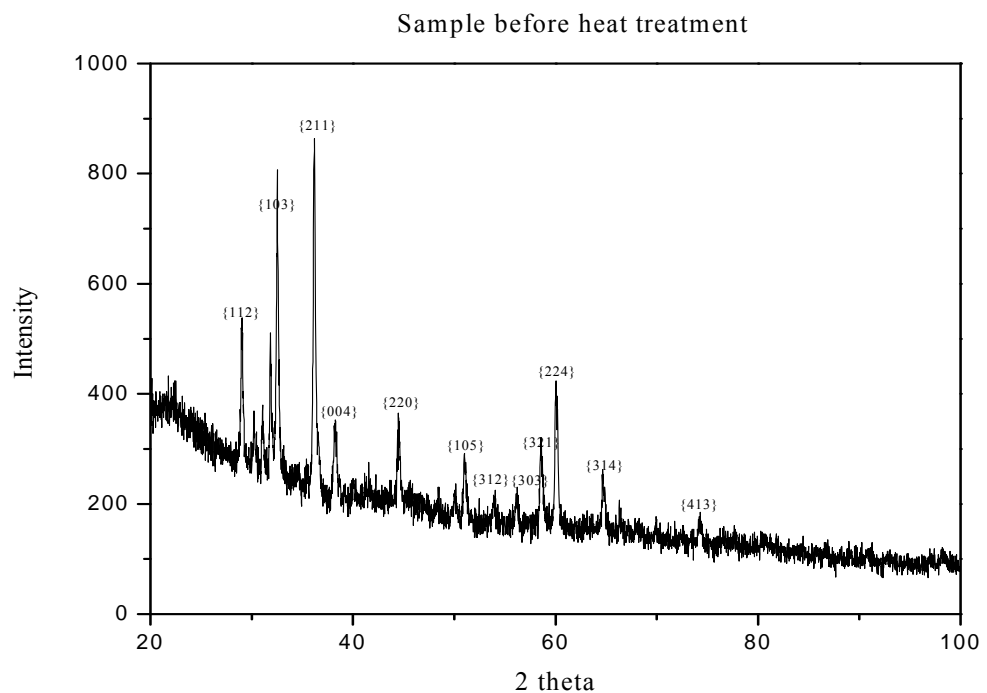


Figure 3.16 XRD spectrum of the precursor sample before heat treatment

temperature and collected. The sample had a notable color change from dark brown to a dark grayish color with a hint of black when collected out of the furnace. The sample was analyzed and the XRD spectrum after the heat treatment is shown in figure 3.17.

The scan shows two crystalline phase present after the heat treatment. The majority of the sample was indexed to MnO with the following peaks present: {111}, {200}, {220},

{311}, {222}, {400}, and {331}. There are two small peaks present in the scan at 30.6° and 37.8° 2θ that were indexed as the {220} and {222} planes of MnAl_2O_4 , respectively. Scherrer analysis performed on the most intense peak {200} of MnO resulted in a grain size of approximately 55 nm.

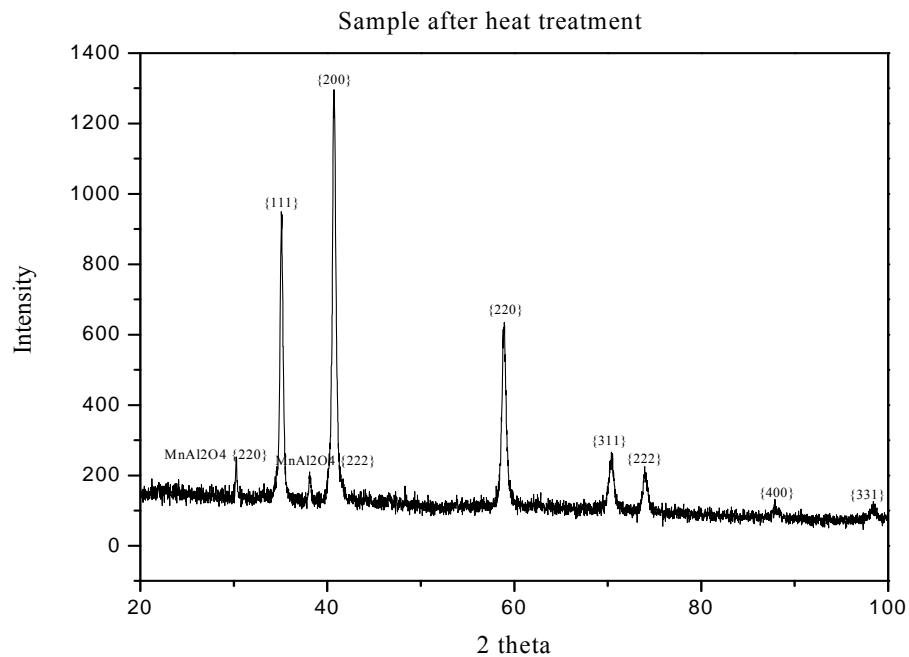


Figure 3.17 XRD spectrum of the sample after heat treatment in the tube furnace

After several synthesis attempts trying a different method to produce ferromagnetic AlMn nanoparticles, it was concluded that this technique was unsuccessful. The resulting particles from these synthesis techniques were all oxides indicating that using H_2 to reduce the particles in a tube furnace was not successful.

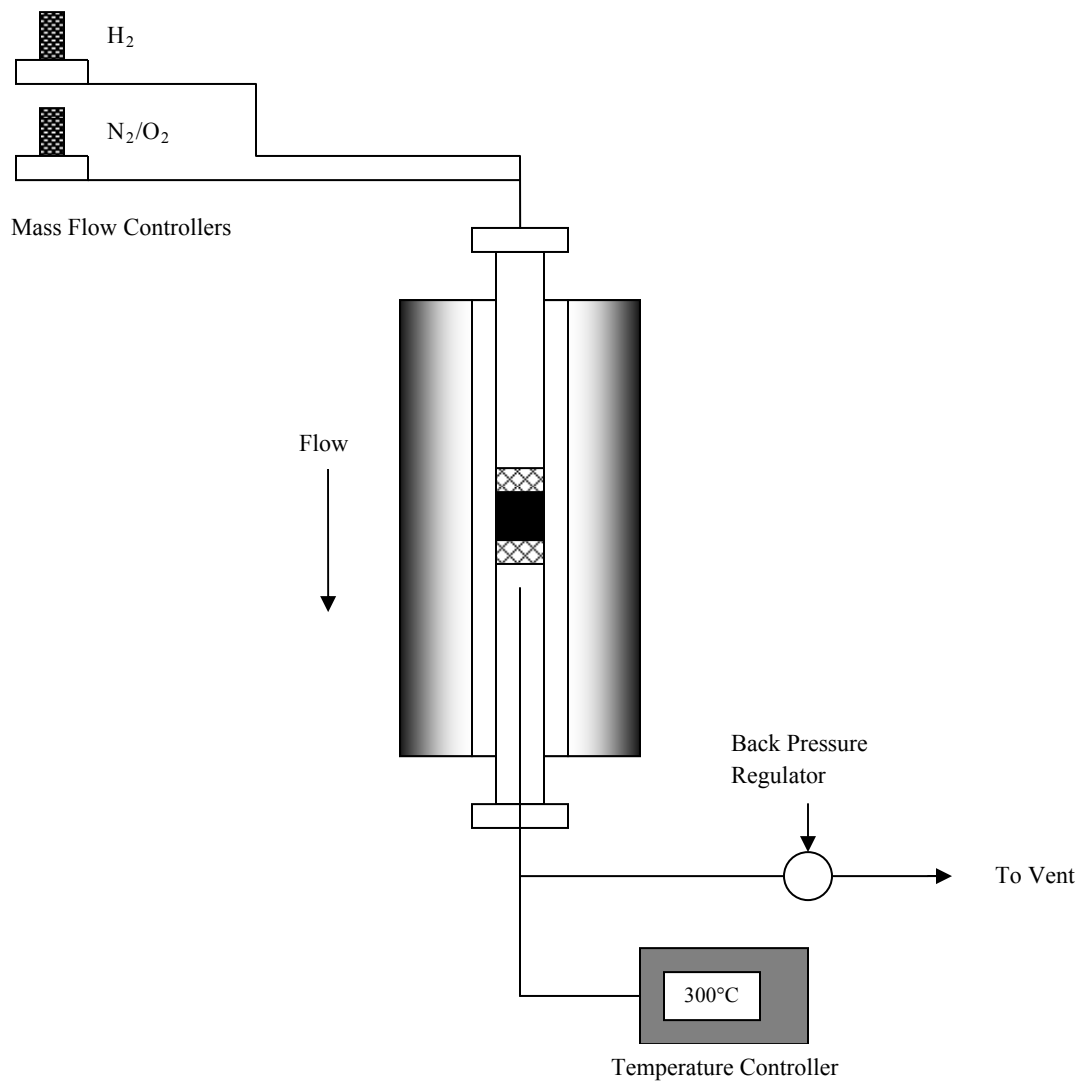


Illustration 3.1 Schematic of the tube furnace reactor setup

3.6 AlMn Synthesis Attempts using LiAlH₄

LiAlH₄ was used as a reducing agent for AlMn nanoparticle synthesis attempts during this research endeavor. LiAlH₄ is a very powerful reducing agent with a potential around +2.6 V which is adequate to reduce both Al and Mn precursors to their zero valence states. LiAlH₄ occurs in powder form or in liquid form dissolved in an organic solvent such as THF, and all forms of LiAlH₄ are soluble in most organic solvents. LiAlH₄ thermally decomposes at high temperatures above 170°C into LiH₂, Al, and H₂, so it is possible that this reducing agent could also provide a source of Al for the reaction. The LiAlH₄ used in this research was in liquid form as a 2 M solution in THF because it could easily be injected into the reaction with a syringe. The attempted syntheses using LiAlH₄ as the reducing agent are detailed in this section.

Synthesis 1 using LiAlH₄

The first synthesis attempt used 0.5 mmols of Al(acac)₃ and 0.5 mmols of Mn(acac)₂ as precursors in 20 mL of dioctyl ether as the solvent. The solution was heated to 100°C and 0.5 mmols of oleic acid and 0.5 mmols of oleylamine were injected as the surfactants. The solution was heated to 200°C where 2 mL of LiAlH₄ was injected as the reducing agent. The solution dropped in temperature from 200°C to around 150°C after the reducing agent was injected due to the low boiling point of the THF (66°C). The THF was distilled off over a period of about 30 minutes and the reaction proceeded to reflux at 287°C for 30 minutes. The solution started out light brown and turned darker

brown around 155°C. The solution turned black upon the addition of the reducing agent. After 30 minutes at reflux, the solution was cooled to room temperature and ethanol was added to precipitate the particles. After allowing the solution to sit for several hours, it was observed that particles did not settle out to the bottom of the beaker and the supernatant was still dark. The solution was isolated and purified by the standard procedure. No particles were re-dispersed in hexane and surfactants, so the precipitate was kept and stored in hexane for analysis. XRD analysis on the precipitate showed no peaks in the spectrum indicating that only amorphous material was yielded from this synthesis.

Synthesis 2 using LiAlH₄

The next synthesis attempt to report used 0.5 mmols of trioctylaluminum and 0.5 mmols of Mn₂(CO)₁₀ as precursors in 20 mL of dioctyl ether as the solvent. Also, 1 mmol of 1,2-hexadecandiol was added to the flask at the start of the reaction. The solution was heated to 100°C and 0.5 mmols of oleic acid and 0.5 mmols of oleylamine were injected as the surfactants. The solution was heated to 200°C where 1 mL of LiAlH₄ was injected as the reducing agent. The solution started out yellow and a noticeable reaction occurred around 150°C when the Mn₂(CO)₁₀ thermally decomposed. After injection of the reducing agent, the solution turned black which indicated particle formation. Also, the solution dropped in temperature from 200°C to around 150°C after the reducing agent was injected due to the low boiling point of the THF (66°C). The THF was distilled off over a period of about 30 minutes and the reaction proceeded to

reflux at 287°C for 30 minutes. After 30 minutes at reflux, the solution was cooled to room temperature and ethanol was added to precipitate the particles. After two hours the particles had settled out in the beaker and the supernatant was almost clear which had not been observed in previous reactions. The standard isolation and purification technique was used for this synthesis. There was a large yield of re-dispersed particles which were stored in hexane for analysis. The precipitate or sediment was kept for analysis, and it contained two noticeably different colored layers of grey and black. When ethanol was added to re-precipitate the particles, the solution turned grayish-brown, but then the particles turned back to black when hexane was added to store them. This observation could have indicated oxidation occurred during re-precipitation step. SEM EDS gave a composition of $\text{Al}_{38}\text{Mn}_{62}$ for the particles.

Figure 3.18 shows the XRD spectrum generated from these particles. The large broad peak at $32.9^\circ 2\theta$ was indexed as the $\{222\}$ plane and the small broad peak around $21^\circ 2\theta$ was indexed as the $\{211\}$ plane from cubic Mn_2O_3 . Since Al was seen in the SEM it was concluded that Al was present as an amorphous material and most likely an oxide. The addition of ethanol which turned the particles grayish-brown could be an indication of oxidation, but it was strange that they turned black after hexane addition. The sediment was also kept from the washing and cleaning procedure. Figure 3.19 shows the XRD spectrum of the sediment generated from this synthesis which shows only a large broad peak around $20^\circ 2\theta$ which confirms only amorphous material present in the

sediment. Figure 3.20 shows TEM images of the particles produced by this synthesis. The particles obtained are approximately 5-8 nm in diameter.

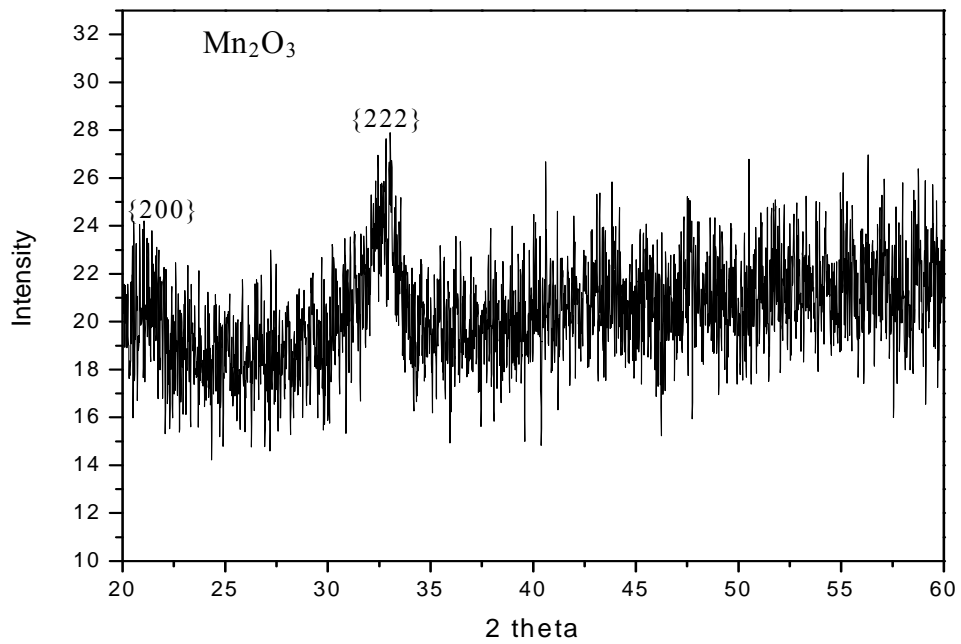


Figure 3.18 XRD spectrum from particles obtained from an AlMn synthesis using LiAlH_4

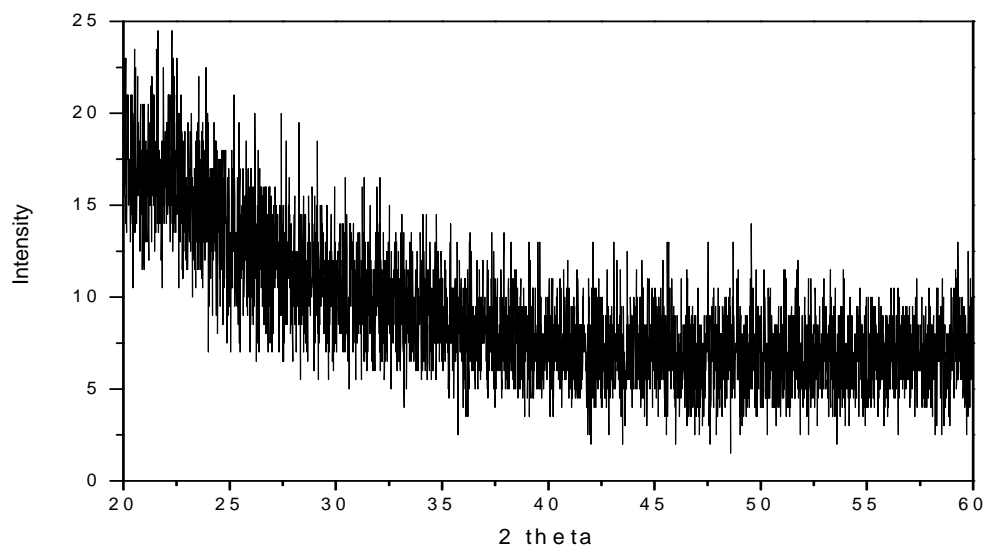


Figure 3.19 XRD spectrum from the sediment obtained from an AlMn synthesis using LiAlH_4

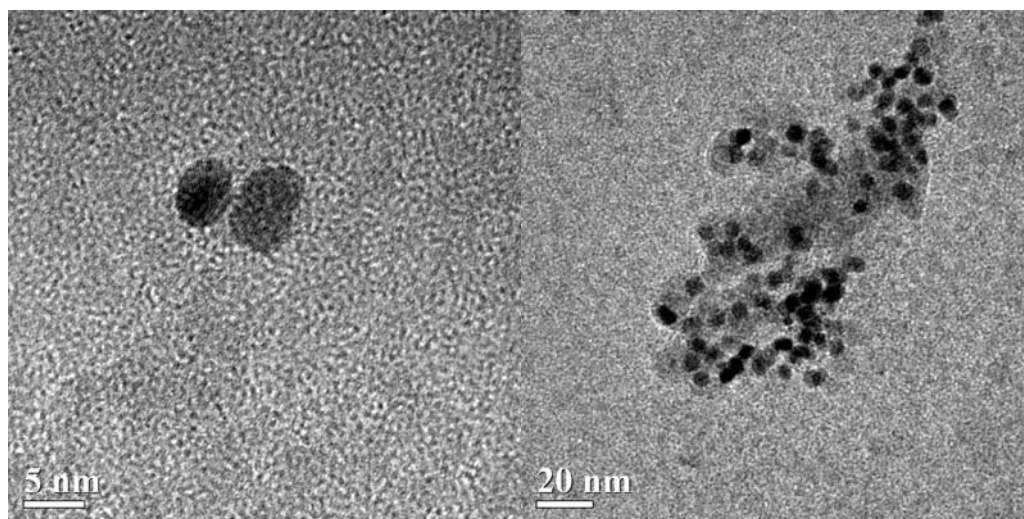


Figure 3.20 TEM images of Mn_2O_3 particles produced from the synthesis using LiAlH_4

Synthesis 3 using LiAlH₄

Another synthesis attempt used 1.2 mmols of Al(acac)₃ and 0.2 mmols of Mn₂(CO)₁₀ as precursors in 20 mL of benzyl ether as the solvent. The solution was heated to 100°C and 0.5 mmols of oleic acid and 0.5 mmols of oleylamine were injected as the surfactants. The solution was heated to 200°C where 2 mL of LiAlH₄ was injected as the reducing agent. The solution immediately turned black upon the addition of the reducing agent which indicated particle formation. Also, the solution dropped in temperature from 200°C to around 150°C after the reducing agent was injected due to the low boiling point of the THF (66°C). The THF was distilled off over a period of about 30 minutes, but when the solution was heating up toward reflux the solution suddenly turned red around 230°C and remained red up to reflux at 298°C. The solution was at reflux for 30 minutes where the solution remained red and transparent. After 30 minutes at reflux, the solution was cooled to room temperature and ethanol was added but no precipitate was obtained, therefore no particles were obtained via this route.

Synthesis 4 using LiAlH₄

Another synthesis attempt used 0.5 mmols of Al(acac)₃ and 0.5 mmols of Mn(acac)₂ as precursors in 20 mL of TOA as the solvent. The solution was heated to 100°C and 0.5 mmols of TOP was injected as the surfactant. The solution was heated to 200°C where 2 mL of LiAlH₄ was injected as the reducing agent. The solution dropped in temperature from 200°C to around 150°C after the reducing agent was injected due to

the low boiling point of the THF (66°C). The THF was distilled off over a period of about 30 minutes then heated up to reflux. The solution started out light brown and remained light brown until the reducing agent was injected. After the LiAlH₄ was injected, the solution turned light green then turned back brown around 310°C to reflux at 368°C. During reflux the solution turned reddish purple in color and became slightly transparent. This indicates that no particles were formed and the previous combinations of precursors, surfactants, and solvents did not work with LiAlH₄ as the reducing agent.

Several reactions were done using LiAlH₄ as the source of Al for the synthesis of AlMn nanoparticles. LiAlH₄ decomposes at high temperatures around 150-170°C into LiH₂, Al, and H₂. In these synthesis attempts Mn₂(CO)₁₀ was used as the Mn precursor which does not need a reducing agent because it thermally decomposes around 150°C. The idea was that the Mn₂(CO)₁₀ would thermally decompose and Mn seeds would be present in solution. Then, the LiAlH₄ would be injected and decompose yielding a source of Al, and the Al nuclei would grow with the Mn seeds in solution to form AlMn nanoparticles.

Synthesis 5 using LiAlH₄

The first synthesis attempt used 0.5 mmols of Mn₂(CO)₁₀ and 1.0 mmols of LiAlH₄ as the precursors in 20 mL of dioctyl ether as the solvent. The solution was heated to 100°C and 0.5 mmols of oleic acid and 0.5 mmols of oleylamine were injected as the surfactants. The solution was heated to 200°C where 2 mL of LiAlH₄ was injected as the reducing agent and the source of Al. Immediately upon the LiAlH₄ being injected,

the solution turned black which indicated particle formation. Also, the solution dropped in temperature from 200°C to around 150°C after the reducing agent was injected due to the low boiling point of the THF (66°C). The THF was distilled off over a period of about 30 minutes and the reaction proceeded to reflux at 287°C for 30 minutes. After 30 minutes at reflux, the solution was cooled to room temperature and ethanol was added to precipitate the particles. The particles settled out in the beaker after several hours with the supernatant mostly clear. The standard isolation and purification technique was used for this synthesis. There was a large yield of re-dispersed particles which were stored in hexane for analysis. The precipitate or sediment was kept for analysis, and it contained two noticeably different colored layers of grey and black. XRD analysis was done on both the sediment and particles obtained from this synthesis. Figure 3.21 shows the XRD spectrum from the particles obtained from this synthesis. The large broad peak at 32.9° 2θ was indexed as the {222} plane and the small broad peak around 21° 2θ was indexed as the {211} plane of cubic Mn₂O₃. Figure 3.22 shows the XRD spectrum from the sediment obtained from this reaction and the only peak present is a large broad peak around 20° 2θ which indicates the presence of amorphous material.

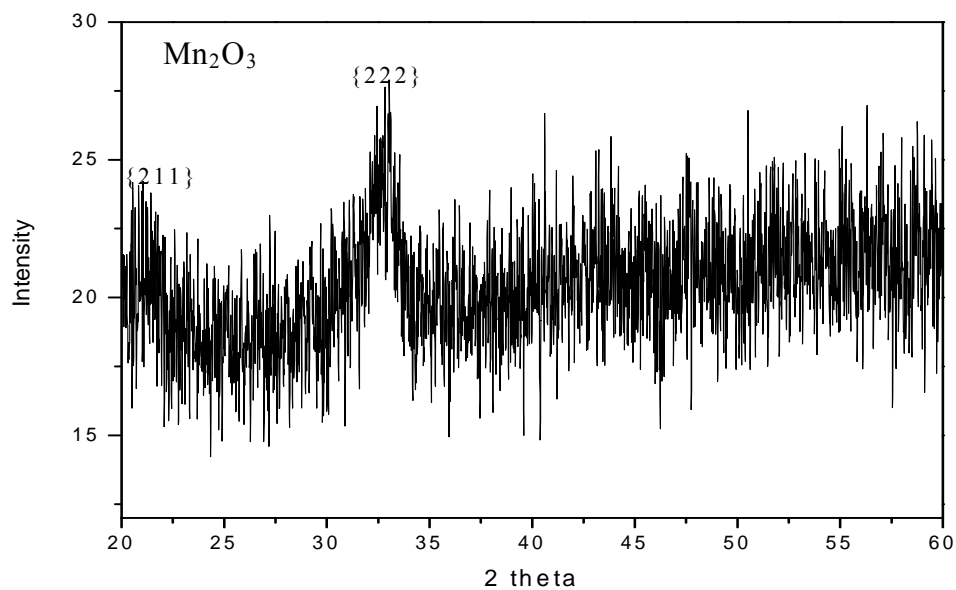


Figure 3.21 XRD spectrum from the particles generated from an AlMn reaction using LiAlH_4

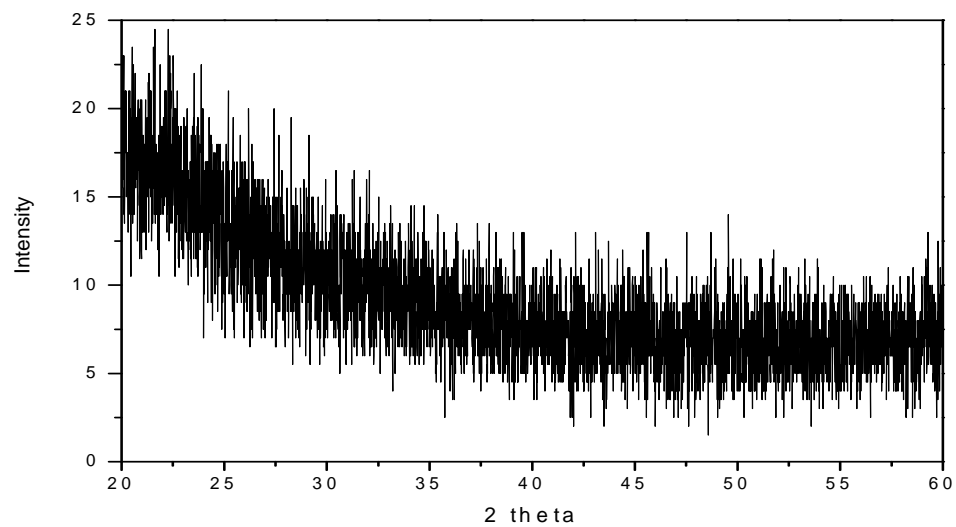


Figure 3.22 XRD spectrum of the sediment from an AlMn reaction using LiAlH_4

Samples of the particles and sediment generated from these reactions were annealed for 1 hour in a furnace with gas comprised of 95% Ar and 5% H₂ at temperatures of 500°C, 600°C, 700°C, 800°C, and 950°C to see if any AlMn would form or if any sample showed ferromagnetism. None of these samples showed any signs of the ferromagnetic τ phase or the ϵ phase of AlMn after annealing. All of the reactions that were done using LiAlH₄ as the source of Al yielded particles of Mn₂O₃ with a minor phase of β -Mn, but no form of AlMn was present.

The synthesis attempts using LiAlH₄ to produce AlMn nanoparticles were overall unsuccessful. These synthesis attempts were the most disappointing during this research due to the solutions turning black upon addition of the reducing agent which indicated particle formation. However, the particles that formed during these reactions were Mn oxides and not AlMn nanoparticles. These reactions looked the most like FePt or MnPt reactions than any other reactions during this research. A solution turning black was the main observation to determine when particles form in a transition metal nanoparticle synthesis such as FePt or MnPt. The analysis of the products from these synthesis routes yielded Mn oxide particles mostly Mn₂O₃ with amorphous Al oxides present. It was not possible to determine if AlMn particles formed during these reactions and then oxidized upon contact with the atmosphere, or if the resulting oxide particles were synthesized during the reaction. These syntheses gave speculation that oxidation was a major concern of the AlMn system which was contradictory to literature on AlMn bulk alloys where oxidation was never reported as a concern. This could be evidence that oxidation was a

factor for the AlMn system on the nanoscale and that measures would have to be taken to prevent oxidation. Ultimately, the goal of producing AlMn nanoparticles was not achieved using LiAlH_4 as the reducing agent.

3.7 AlMn Synthesis Attempts using Sodium (Na)

Sodium (Na) is a very powerful reducing agent, and it was used for synthesis attempts to produce AlMn nanoparticles. Na is an alkali metal that is silvery white and is a solid at room temperature but can easily be cut with a knife. Na has a melting point of 97°C and is soluble in most organic solvents. Na has a potential of around +2.6 V which should be capable to reduce both Al and Mn precursors to their zero valence state. The Na metal that was used in this research was in solid form and stored in kerosene to prevent oxidation. Na quickly oxidizes with contact to the air and reacts violently with water; therefore it must be handled with care. Using a solid reducing agent in a wet chemical synthesis can create mass transfer issues during the reaction. The precursors and surfactants were dissolved in the solvent, so solid Na must be dissolved in the solution or the only reaction would take place on the surface of the solid Na. This could be an issue because most every other reducing agent was in liquid form, so reaction can take place immediately upon being added to the solution. Finding a compatible solvent for Na was critical or it may not be a feasible reducing agent for a wet chemical metal nanoparticle synthesis. Na was used for a majority of the reactions performed during this research project. The Na chunks used in each reaction was washed with hexane to remove all the kerosene before addition to the reaction. Also, the Na was added as

quickly as possible from the time of weighing the sample to addition into the flask to prevent oxidation. When Na was first used as the reducing agent for synthesis attempts, several reactions were done at room temperature then the temperature was gradually increased to determine that Na was safe to use for these reactions. Many different combinations of precursors, surfactants, and solvents were utilized with Na as the reducing agent for AlMn synthesis attempts. It was quickly learned that MnCl_2 and AlCl_3 were not compatible precursors with Na as the reducing agent because the reaction produced NaCl particles. Many lessons were learned during the AlMn reactions because over half of the synthesis attempts of AlMn nanoparticles used Na, and those lessons along with the reaction procedures are chronicled in this section. The following section highlights several AlMn synthesis reactions using Na as the reducing agent and the results are described in detail.

Synthesis 1 with Na

The first synthesis attempt discussed used 0.5 mmols of trioctylaluminum and 0.5 mmols of $\text{Mn}_2(\text{CO})_{10}$ as precursors in 20 mL of diphenyl ether as the solvent. The precursors were added to the flask with the solvent at the start of the reaction. The solution was heated to 100°C and 0.2 mL of oleic acid and 0.2 mL of oleylamine were injected as the surfactants. The solution was heated to 200°C where 2.5 mmols of Na was added as the reducing agent. The solution started out dark yellow in color and remained that way until the Na was added at 200°C . The solution turned dark black around 220°C which indicated particle formation. The solution was heated to reflux at

260°C for 30 minutes. The standard isolation and purification method was used for this reaction, but no particles were separated from the reaction precipitate. Figure 3.23 shows the as made and annealed at 500°C particles analyzed by XRD. The as made spectrum was difficult to index to a crystalline material and the broad most intense peak around 20° 2θ indicated the sample contained amorphous material, but the sample annealed at 500°C was indexed to Mn oxides. The sample contained both cubic MnO and cubic Mn₃O₄. Cubic MnO was indexed by the following peaks: {001} at 36.4° 2θ, {200} at 41.4° 2θ, {220} at 59.6° 2θ, {311} at 71.4° 2θ, {222} at 74.6° 2θ. Cubic Mn₃O₄ was indexed by the following peaks: {101} at 31.1° 2θ, {103} at 32.5° 2θ, {211} at 36.2° 2θ, {220} at 45.5° 2θ, {321} at 58.8° 2θ, {224} at 60° 2θ, {314} at 64.6° 2θ.

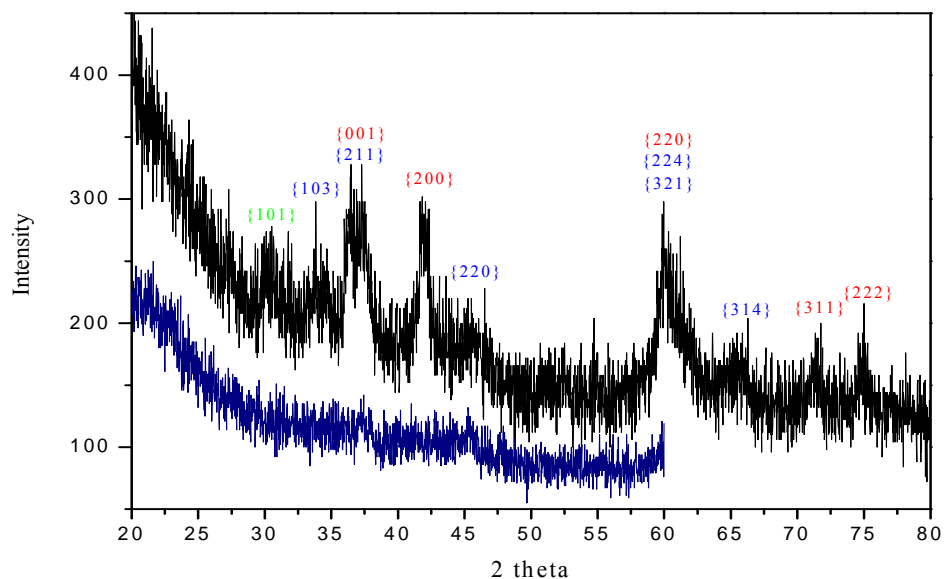


Figure 3.23 XRD spectrum of particles from an AlMn synthesis using Na as made and annealed at 500°C

Figure 3.24 shows TEM images from the particles generated by this reaction. The image on the left shows what the majority of the sample looked like. It appeared to be large areas of amorphous material with very small areas of crystalline particles shown in the picture on the right. This agreed with the XRD of the as made particles which showed no discernable peaks from a crystalline material but just one large peak corresponding to amorphous material.

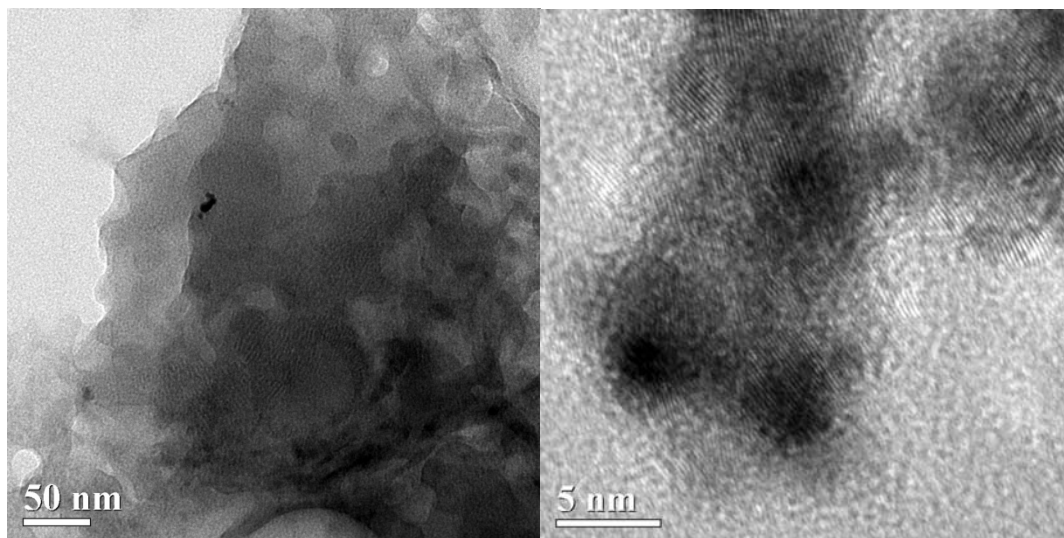


Figure 3.24 TEM images from an AlMn synthesis using Na

Synthesis 2 with Na

The next synthesis attempt discussed used 0.5 mmols of $\text{Al}(\text{acac})_3$ and 0.5 mmols of $\text{Mn}_2(\text{CO})_{10}$ as precursors in 20 mL of diphenyl ether as the solvent. The precursors were added to the flask with the solvent to begin the reaction. The solution was heated to 100°C and 0.2 mL of oleic acid and 0.2 mL of oleylamine were injected as the surfactant. The solution was heated to 200°C where 2.5 mmols of Na was added as the reducing agent. The solution started out dark yellow and remained that way until the Na was added at 200°C . The solution turned white after the Na addition and the Na appeared to be dissolved in the solution. Around 230°C the solution turned dark red-orange and a white cloud emerged above the solution in the flask. This white cloud looked like the result of a reaction that occurred in the flask. The solution was heated to reflux at 260°C for 30 minutes. The solution turned black around the start of reflux indicating particle

formation. The standard isolation and purification method was used for this reaction, but no particles were separated from the reaction precipitate. SEM analysis of the particles gave a composition of $\text{Al}_{19}\text{Mn}_{81}$. XRD analysis was performed on the as made and annealed at 400°C particles and shown in figure 3.25. The as made spectrum has two weak peaks visible around 35° and $41^\circ 2\theta$ which were indexed to the $\{111\}$ and $\{200\}$ peaks of cubic MnO. Figures 3.26 and 3.27 shows TEM analysis of the particles and a histogram from the lattice fringes gave a d-spacing of 2.48\AA which matches the $\{111\}$ plane of cubic MnO. The TEM images from this synthesis seemed to have less areas of what appeared to be amorphous material and more areas of particles. The sample annealed at 400°C showed more intense peaks but it was also indexed to cubic MnO by the $\{111\}$ peak at $35.2^\circ 2\theta$, the $\{200\}$ peak at $41.4^\circ 2\theta$, and the $\{220\}$ peak at $59.6^\circ 2\theta$. Magnetic measurements performed on the as made and annealed samples yielded nothing ferromagnetic.

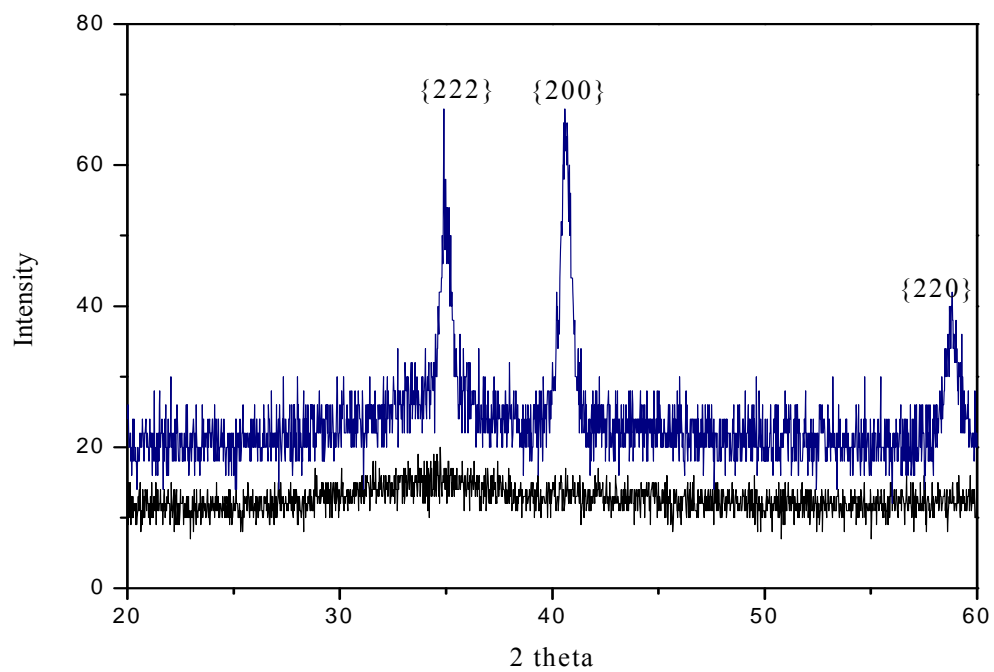


Figure 3.25 XRD spectrum of the particles as made and annealed at 400°C

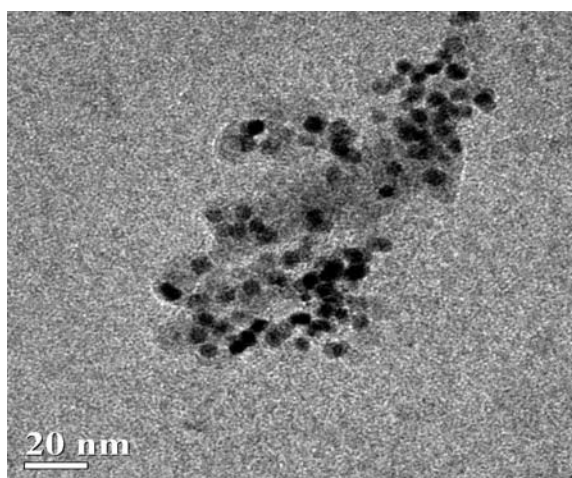


Figure 3.26 TEM image of particles from an AlMn synthesis using Na

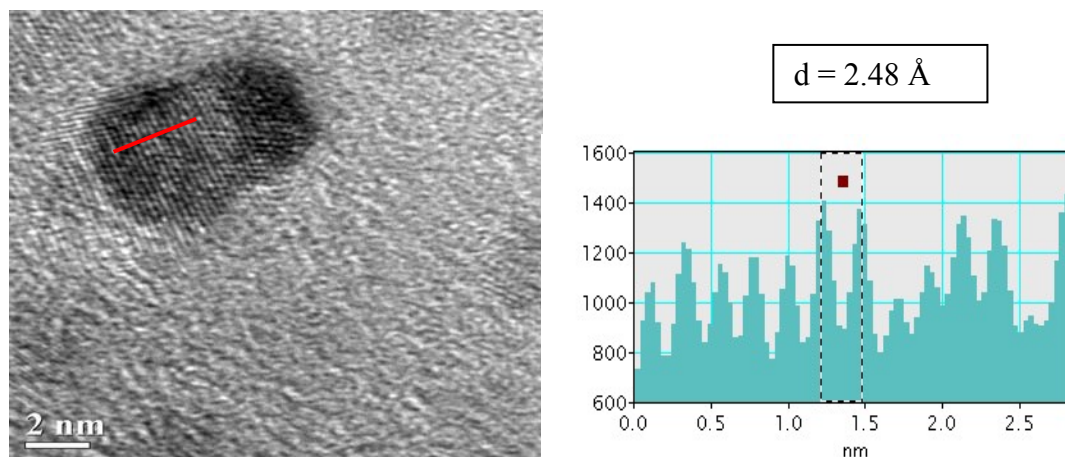


Figure 3.27 High resolution TEM image with a histogram and d-spacing

After many synthesis attempts to produce AlMn nanoparticles using various combinations of precursors and surfactants with diphenyl ether as the solvent which yielded poor results, the solvent was changed to different organic solvents. This agrees with the CV experiments which used diphenyl ether and showed that its potential window was not large enough to reduce Al precursors. By using Na with diphenyl ether, it was possible that the Na actually reduced the solvent before the Al precursor. The results showed that this was what happened due to the formation of Mn oxide particles along with amorphous Al oxides.

Synthesis 3 with Na

The next synthesis attempt discussed used 0.5 mmols of $\text{Al}(\text{acac})_3$ and 0.5 mmols of $\text{Mn}(\text{acac})_2$ as precursors in 25 mL of TOA as the solvent. The precursors were added to the flask with the solvent to begin the reaction. The solution was heated to 100°C and

0.25 mL of TOP was injected as the surfactant. The solution was heated to 200°C where 2.5 mmols of Na was added as the reducing agent. The solution started out light brown and remained that way until the Na was added at 200°C. The solution turned white after the Na addition and the Na appeared dissolve in the solution. Around 285°C the solution turned dark red-orange and a white cloud emerged above the solution in the flask. This white cloud looked like the result of a reaction that occurred in the flask. The solution was heated to reflux at 368°C for 30 minutes. The solution turned black around the start of reflux which indicated particle formation. The standard isolation and purification method was used for this reaction, but only a very small portion of particles were re-dispersed and separated from the sediment which was not enough for thorough analysis. The resulting sediment was dark black, but the consistency was thicker than a normal FePt nanoparticle dispersion. The resulting as made particles were analyzed from this reaction, and samples from this reaction were annealed for 1 hour at 950°C in a tube furnace under an atmosphere of 5% H₂ and 95% Ar. Figure 3.28 shows the XRD analysis from the as made particles and the particles annealed at 950°C. The large broad peak at 33.4° 2θ was indexed as the {222} plane and the small broad peak around 22° 2θ was indexed as the {211} plane from Mn₂O₃. The sample that was annealed at 950°C was also indexed to Mn₂O₃, but the peaks were more intense and a couple more peaks became present in the XRD spectrum. The {211} and {222} peaks remained present in the same location as the as made particles, but the {332} peak was present at 44.5° 2θ and the {422} peak was present at 47° 2θ. SEM EDS was performed on the sediment to

get the composition of Al and Mn present which was 12% and 88%, respectively. Figure 3.29 shows a high-resolution TEM image of the particles with a histogram and a calculated d-spacing of 2.68Å which corresponds to the most intense peak {222} of Mn₂O₃. Magnetic measurements were performed on the samples as shown in figure 3.30, and the results were quite unexpected. The as made loop shows a coercivity of 1.2 kOe indicating that the sample showed signs of ferromagnetism. The annealed sample loop shows an even larger hysteresis loop with a coercivity of approximately 5.2 kOe. The top right area of the annealed hysteresis loop has an open area where the loop does not come back together which indicates that the sample was not fully saturated at 18 kOe, the maximum applied field of the AGM. The loop also showed a bend when it crossed the y-axis in both directions. This could indicate that the sample was made up of two components which included a hard magnetic component and a soft magnetic moment. Also, remnance measurements were performed on the annealed sample to extract KV/kT data. Figure 3.31 shows the graph of remnant coercivity as a function of time at field and plotted with Sharrock's equation (equation 1.2) to extract KV/kT which was 41.2. This KV/kT number was low compared to ferromagnetic FePt nanoparticles, and the recording industry would prefer a KV/kT to be 60 or greater. The results from this reaction were unusual. XRD and TEM indicated that the particles were Mn₂O₃, and while Mn itself can be magnetic, Mn oxides were not known to be ferromagnetic. The only phase of AlMn that was ferromagnetic was the τ phase which would give magnetic measurements similar to the results from this reaction, but there was no evidence that points to any

phase of AlMn present or specifically the τ phase. Furthermore, other possible combinations of

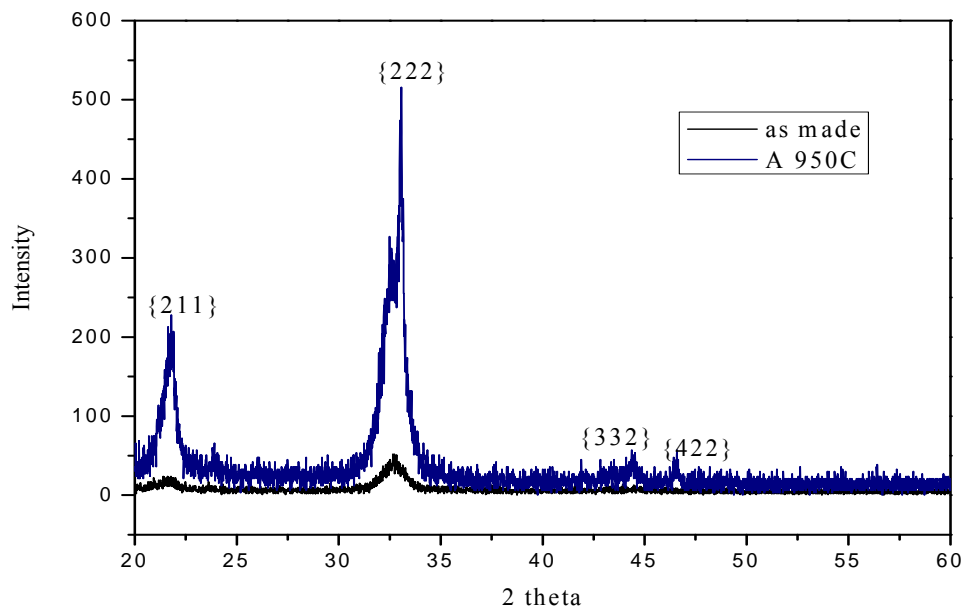


Figure 3.28 XRD spectrums of the sample as made and annealed at 950°C

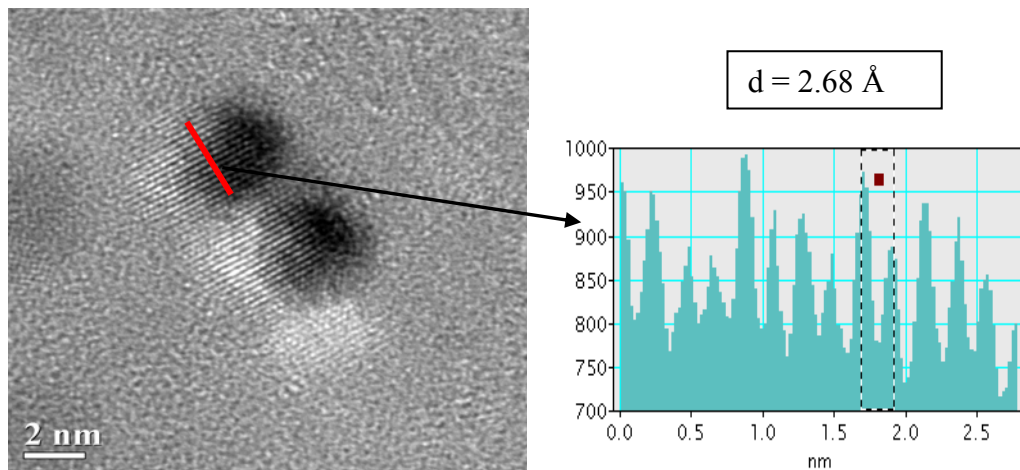


Figure 3.29 High resolution TEM image with histogram

elements present during this reaction that could have formed crystalline particles leading to misidentification of the results given were explored but no other possible scenarios existed.

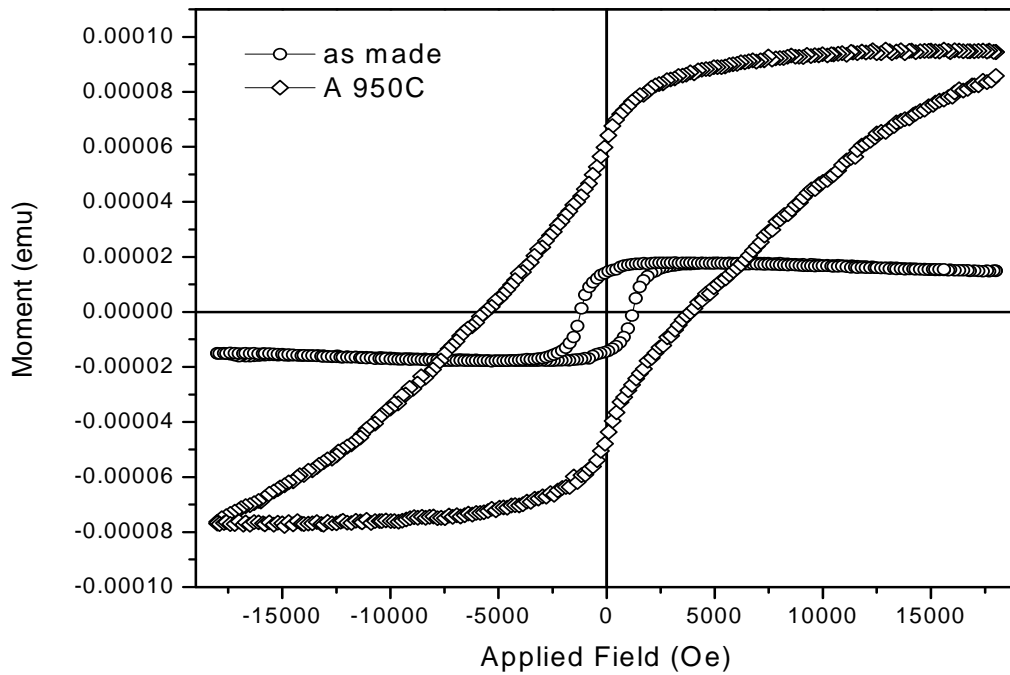


Figure 3.30 Hysteresis loops of as made and annealed at 950°C particles

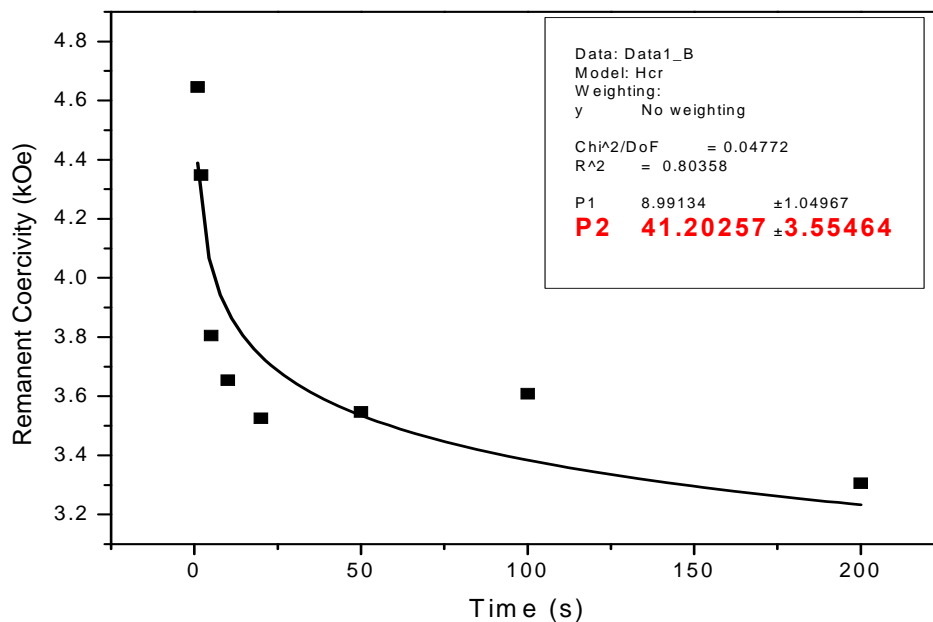


Figure 3.31 Graph of remnant coercivity as a function of time at field and plotted with Sharrock's equation to provide KV/kT

Similar results were seen in other reactions that followed similar routes as this one, but none were identified as being any phase of AlMn specifically the ferromagnetic τ phase. At this point this research was in a position with too many variables to reasonable explore attached with the development and characterization of AlMn nanoparticles. The focus shifted on completely identifying the particles that had been produced from these synthesis attempts and the variables just associated with the wet

chemical phase reaction, and not the variables associated with heat treatments and annealing post-synthesis.

After many AlMn reactions using Na as the reducing agent a trend was emerging of difficulty to separate the particles from unwanted reaction byproducts using the standard isolation and purification technique. Even using different combinations of precursors, surfactants and solvents with Na as the reducing agent for synthesis, the standard procedure was not effective. Deviations of the standard isolation and purification technique were tried during the course of this research that used different organic solvents such as 2-butanone, cyclohexanone, DMF, toluene, and pyridine along with different surfactants such as TOP, TOPO, and TOA to find a combination to separate the particles with no success. Finally, the phase transfer isolation and purification technique was implemented for AlMn reactions that used Na as the reducing agent. This method was discussed in detail in section 2.2.2. TMAOH was used as the surfactant to stabilize the particles in an aqueous solution, and the remaining unwanted organics specifically Na ions can be removed from the particles. This procedure was utilized often with reactions using Na, and an example of using the phase transfer technique is discussed along with the results of implementing this procedure on an AlMn nanoparticle synthesis.

Synthesis 4 with Na

An AlMn reaction that employed the phase transfer technique used 2.10 mmols of $\text{Al}(\text{acac})_3$ and 0.3 mmols of $\text{Mn}_2(\text{CO})_{10}$ as precursors in 25 mL of TOA as the solvent. The precursors were added to the flask with the solvent to begin the reaction. The solution was heated to 100°C and 0.5 mL of TOP was injected as the surfactant. The solution was heated to 200°C where 2.5 mmols of Na was added as the reducing agent. The solution started out transparent with a light yellow color and remained that way until the Na was added at 200°C. The solution turned white after the Na addition and the Na appeared to dissolve in the solution. Around 290°C the solution turned dark yellow, then the solution turned dark orange at 330°C along with a white cloud that emerged above the solution in the flask that indicated a reaction occurred. The solution was heated to reflux at 368°C for 30 minutes. The solution turned dark black a few minutes into reflux which indicated particle formation. The solution was cooled to room temperature and methanol was added to precipitate the particles and the phase transfer isolation and purification method was implemented. When methanol was added to the reaction product, excess Na chunks were observed being neutralized. A small part of the precipitate or sediment was collected for analysis before the phase transfer method started. It was observed that the sediment had layers of different colors of gray and dark black. The particles that were separated by this method were dark black in color with no gray left which indicated that something had been successfully removed. The particles were transferred back to an organic solvent (hexane) from the aqueous solution to make analysis easier. Both the

sediment and particles were analyzed from this reaction and isolation and purification method. SEM EDS analysis was performed on the sediment and the particles collected after the phase transfer technique. The sediment yielded a composition of $\text{Al}_{58}\text{Mn}_{42}$ and a fairly large Na peak was observed which indicated that Na was still present after the reaction. The particles collected yielded a composition of $\text{Al}_{63}\text{Mn}_{37}$ but there was not a Na peak observed which proved the phase transfer method successfully removed the Na from the particles.

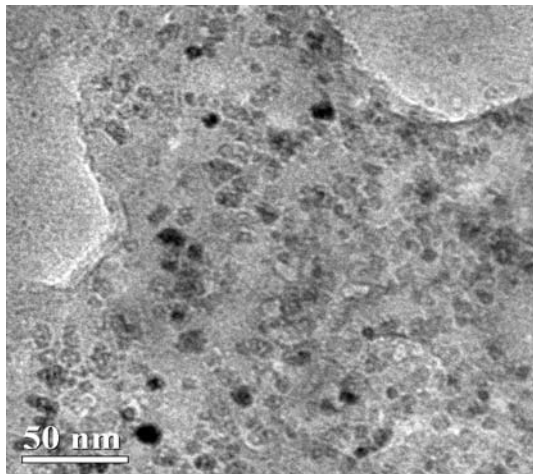


Figure 3.32 TEM image of the sediment from the AlMn synthesis

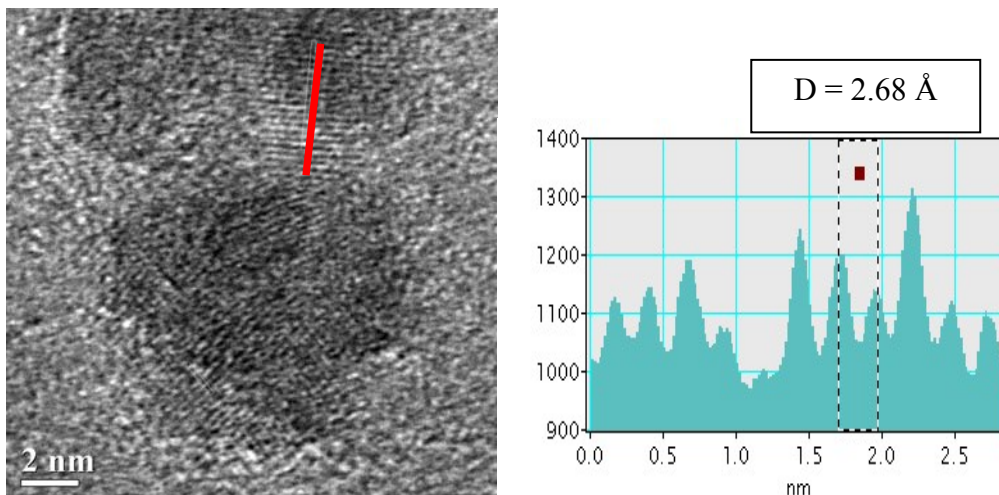


Figure 3.33 High resolution TEM image of the sediment with histogram and d-spacing

Figure 3.32 shows a TEM image taken of the sediment from this AlMn reaction before the phase transfer method was applied. The image shows a large particle size distribution ranging from about 5-20 nm, and the particles appeared to be enclosed by a shell or some form of matrix which was probably amorphous. Figure 3.33 shows a high resolution TEM image from the sediment along with a histogram and a d-spacing from the lattice fringes. The particle has a sphere-like shape but lacks a definitive shape. The d-spacing from the lattice fringes was 2.68 Å which was indexed to the {222} plane of cubic Mn_2O_3 . Figure 3.34 shows the XRD analysis of the sediment from this reaction. There was multiple phases present in this sediment. The peak at $30^\circ 2\theta$ was from the {101} plane of the reducing agent Na. The peaks at 21° , part of the doublet peak at 34° , and the peak at $37.7^\circ 2\theta$ were from a disordered phase MnO_2 . Another phase was characterized and indexed as cubic MnO by the following peaks: {111} at $34.9^\circ 2\theta$, {001} at $38.5^\circ 2\theta$,

{200} at $41.4^\circ 2\theta$, and {332} at $46^\circ 2\theta$. Figure 3.35 shows a TEM image taken of the particles after the phase transfer technique was performed. The image shows the particles were agglomerated in small groups, but the particles after the phase transfer method did not appear to have a shell or some form of amorphous matrix encapsulating them like the sediment. Also, the particle size distribution appeared to narrow ranging from approximately 10-15 nm after this method was applied. Figure 3.36 shows a high resolution TEM image with a histogram taken along the lattice fringes to get a d-spacing. The particles had the shape between a sphere and a cube as indicated by figure 3.36. The d-spacing generated from the lattice fringes of the particle was 2.68 Å and was indexed as the {222} plane of cubic Mn_2O_3 .

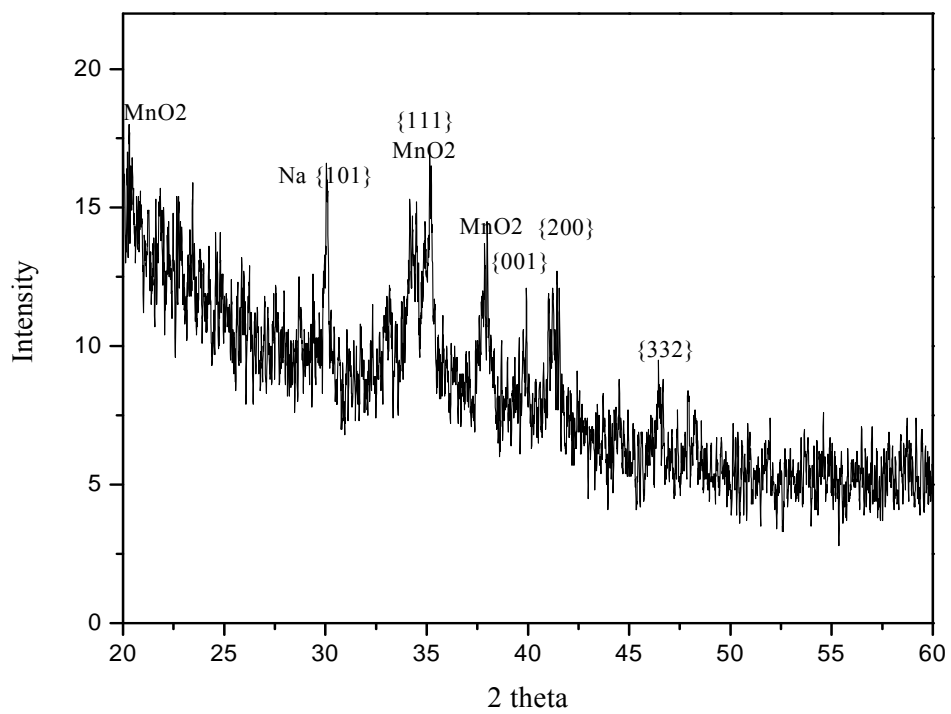


Figure 3.34 XRD spectrum of the sediment before the phase transfer technique

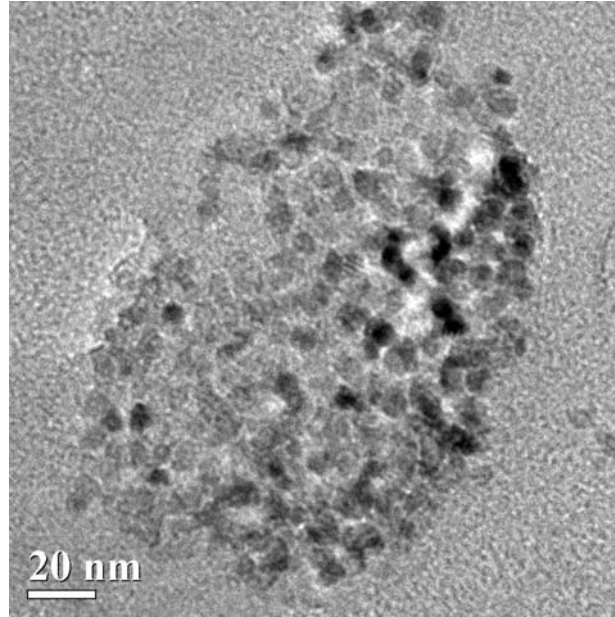


Figure 3.35 TEM image from the particles after the phase transfer technique

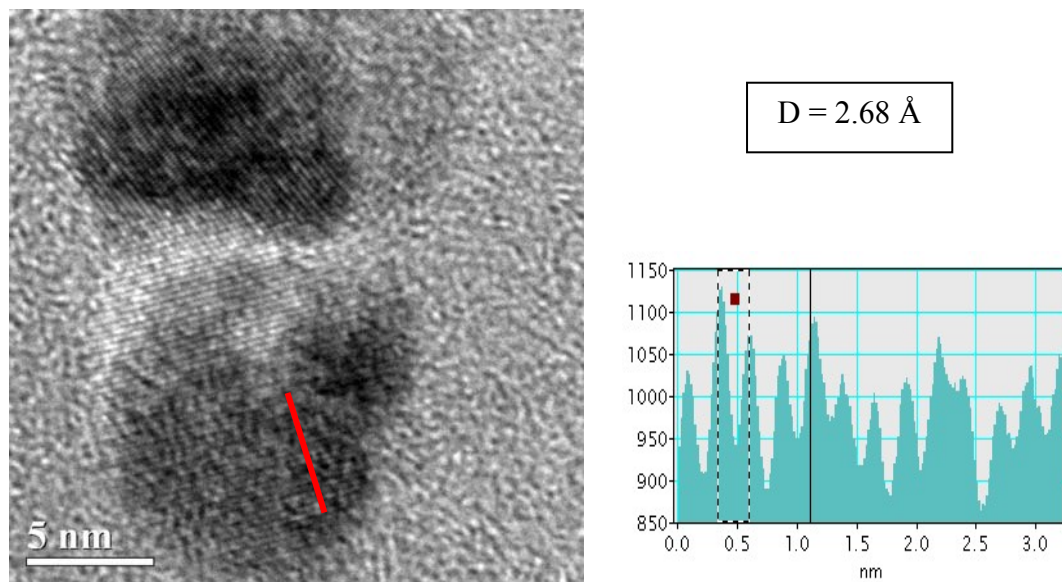
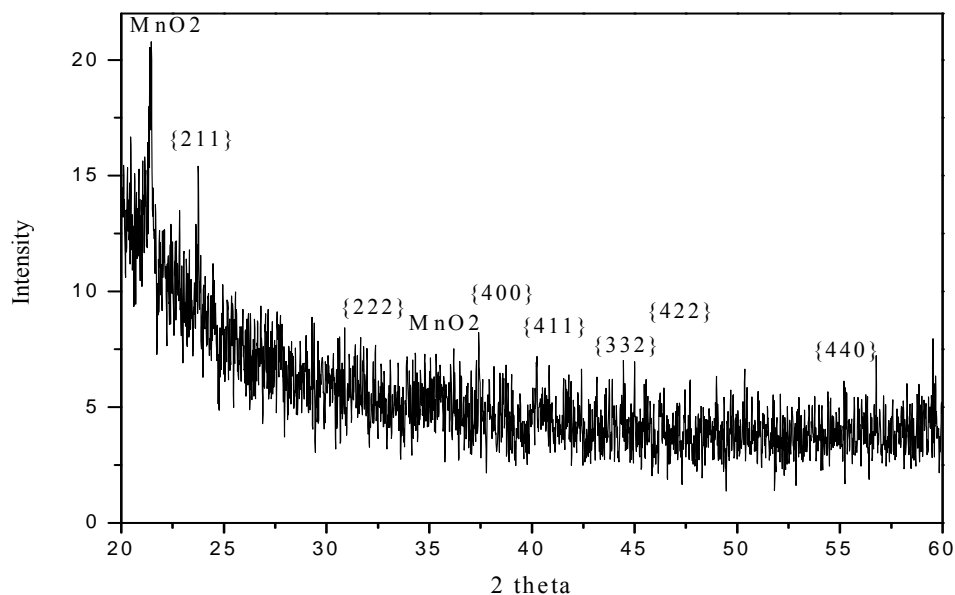


Figure 3.36 High resolution TEM image with histogram and d-spacing of the particles after the phase transfer technique

Figure 3.37 shows the XRD spectrum from the analysis of the particles after the phase transfer procedure was utilized. The intensity of the peaks was extremely low which caused difficulty in distinguishing some of the peaks from the background. This also made the identification of the particles difficult, so all of the information collectively from the particles' analysis was used to determine the phase or phases that were present. The sample used for XRD analysis was not uniformly spread over the wafer because of the agglomerates of particles. Two crystalline phases were present in the product that was collected after the phase transfer procedure, and they were cubic Mn_2O_3 and a disordered intermediate phase of MnO_2 . The peaks at 21° and 34° 2θ were indexed



Fi

Figure 3.37 XRD spectrum of the particles after the phase transfer procedure

As an intermediate phase of MnO_2 with a disordered structure, and the miller indices of the planes have not been characterized. Another phase was characterized and indexed as cubic Mn_2O_3 by the following peaks: $\{211\}$ at $23.1^\circ 2\theta$, $\{222\}$ at $32.9^\circ 2\theta$, $\{400\}$ plane at $38.3^\circ 2\theta$, $\{411\}$ plane at $40.6^\circ 2\theta$, $\{332\}$ plane at $45.1^\circ 2\theta$, $\{422\}$ plane at $47.3^\circ 2\theta$, and the $\{440\}$ plane at $55.2^\circ 2\theta$.

The results of using the phase transfer procedure on AlMn reactions using Na as the reducing agent had similarities to the other isolation and purification methods. Both methods separated particles that were dark black similar to FePt nanoparticles from the

sediment which had multiple phases and unwanted byproducts present. The phase transfer method resulted in a much larger yield of particles than other methods, but the resulting particles were difficult to analyze. Particles kept in an aqueous solution did not make a good sample on a Si wafer or a TEM grid for analysis. The Si wafer was not particularly receptive to water, the drying period was much longer than hexane, and the particles did not dry uniformly on the wafer which hindered analysis. TEM samples prepared with the particles in an aqueous solution were not effective for analysis. This was the reasoning for transferring the particles back to hexane from the aqueous solution, but problems arose with this procedure as well. During the phase transfer, the regular surfactants were stripped off the particles and replaced with TMAOH, then re-precipitated with ethanol and the regular surfactants were added back to the particles. The results of this procedure yielded particles that were severely agglomerated while particles produced from the standard method were nicely dispersed. The standard method was mostly unsuccessful on AlMn reactions using Na due to the large size and size distribution of the particles created by these syntheses. The average particle size was approximately 8-10 nm which was close to the upper limit of the size selective isolation and purification separation techniques like the standard method. The large size distribution of the particles which ranged from approximately 5-20 nm assisted in the difficulty of the size selective separation techniques. These size issues associated with the particles generated with Na as the reducing agent was most likely linked to the use of a solid reducing agent in the reaction. Most all of the reduction reaction between the

precursors and reducing agent took place in the liquid phase, so there was mass transfer issues associated with the solid reducing agent. It was assumed that there could possibly be some reaction that occurred on the surface of the solid upon addition into the solution at high temperature, but this type of reaction should have been minimal. The Na was added as multiple chunks of solid into the solution at a temperature where the precursors had been dissolved and become basically homogeneous throughout the liquid phase. Each chunk of solid must melt and dissolve into the liquid phase reaction medium for the reaction to begin, and there was a length of time associated with this step. This step was a function of the chunk's size, shape, and surface area, and each piece of Na had a different length of time for this step. Since the reduction reaction of the precursors occurred at different times, particle nucleation and formation occurred at different times which caused the particles to form in many different sizes.

Synthesis 5 with Na

The next synthesis attempt discussed used 2.16 mmols of $\text{Al}(\text{acac})_3$ and 0.3 mmols of $\text{Mn}(\text{acac})_2$ as precursors in 25 mL of TOA as the solvent. The precursors were added to the flask with the solvent to begin the reaction. The solution was heated to 100°C and 1 mL of TOP was injected as the surfactant. The solution was heated to 200°C where 2.5 mmols of Na was added as the reducing agent. The solution started out light yellow in color and transparent and remained that way until the Na was added at 200°C. The solution turned white after the Na addition and the Na appeared to start dissolving in the solution. Around 285°C the solution turned dark red-orange and a white

cloud emerged above the solution in the flask. This white cloud looked like the result of a reaction that occurred in the flask. The solution was heated to reflux at 368°C for 30 minutes. At the beginning of reflux the solution was dark red but proceeded to turn dark black approximately 10 minutes into reflux. The solution was cooled to room temperature and 40 mL of methanol was added to precipitate the particles from the reaction product in a 100 mL beaker. Leftover Na was noticed after the reaction by observing small silver solid pieces floating in the reaction product and the quick dissolution upon adding methanol. After sitting overnight, there was a noticeable partition between the precipitate and the supernatant, but the supernatant was still dark black. The standard washing and cleaning procedure was implemented for the reaction product. Only a small amount of particles re-dispersed in hexane and surfactants from this reaction. The particles were visibly dark but they still were not as dark or thick as FePt nanoparticles to which every synthesis was compared. The sediment that did not re-disperse during the washing and cleaning procedure was kept for analysis. The sediment had two noticeable layers present with one being black and the other was gray. XRD was performed on the sediment from this reaction and the spectrum was shown in figure 3.38. The large broad peak at 32.9° 2θ was indexed as the {222} plane and the small broad peak around 21° 2θ was indexed as the {211} plane from Mn₂O₃. SEM EDS was performed on the sediment to get the composition of Al and Mn present which was 43% and 57%, respectively. There is Al present and the composition is in the range of the sweet spot for the τ phase, but Al is not present as crystalline particles according to XRD.

This result seems to implicate the $\text{Al}(\text{acac})_3$ as the problem in the reaction because 2.1 mmols was used in this reaction which was seven times more than $\text{Mn}(\text{acac})_2$. This could be the reason for the small yield of particles because of the small amount of Mn precursor used. The Al precursor could end up as unreacted and dissolved in the supernatant from the reaction product, and it could also end up as the gray section of the sediment collected. The Al precursor was white so that could account for the gray color in the sediment. TEM images were taken of the sediment from this reaction and they were shown in figure 3.39. The picture on the left showed a group of particles agglomerated together but they appear to have a cube-like shape. The picture on the right was taken at a lower magnification and showed a large particle size distribution ranging from about 10-35 nm in the sediment. Figure 3.40 shows a high resolution TEM image with a histogram and calculated d-spacing. The d-spacing from the lattice fringes was 2.72 Å which matched the {222} plane of cubic Mn_2O_3 which supports the XRD analysis of the sediment.

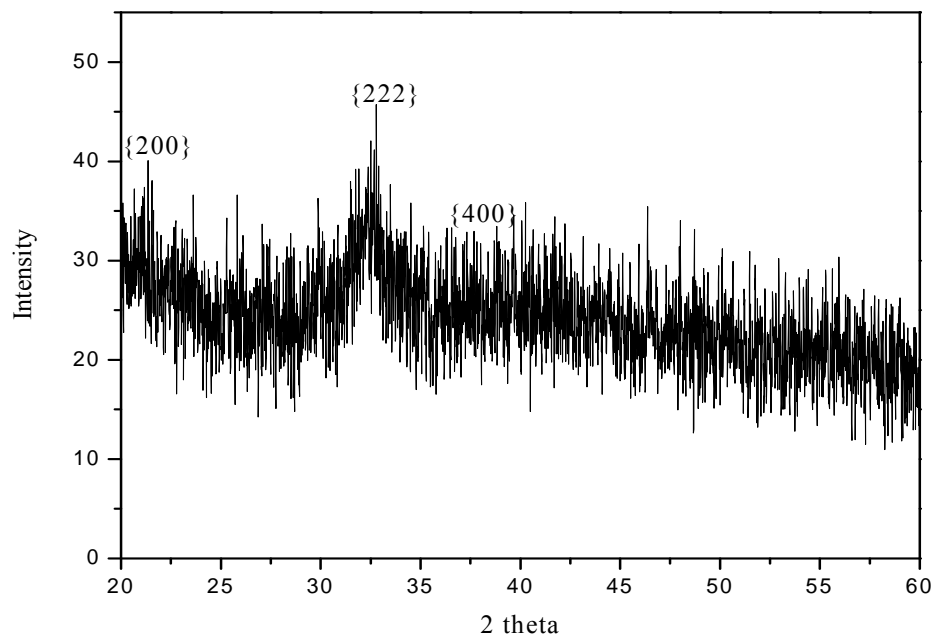


Figure 3.38 XRD from the sediment of the AlMn reaction using Na and indexed as Mn_2O_3

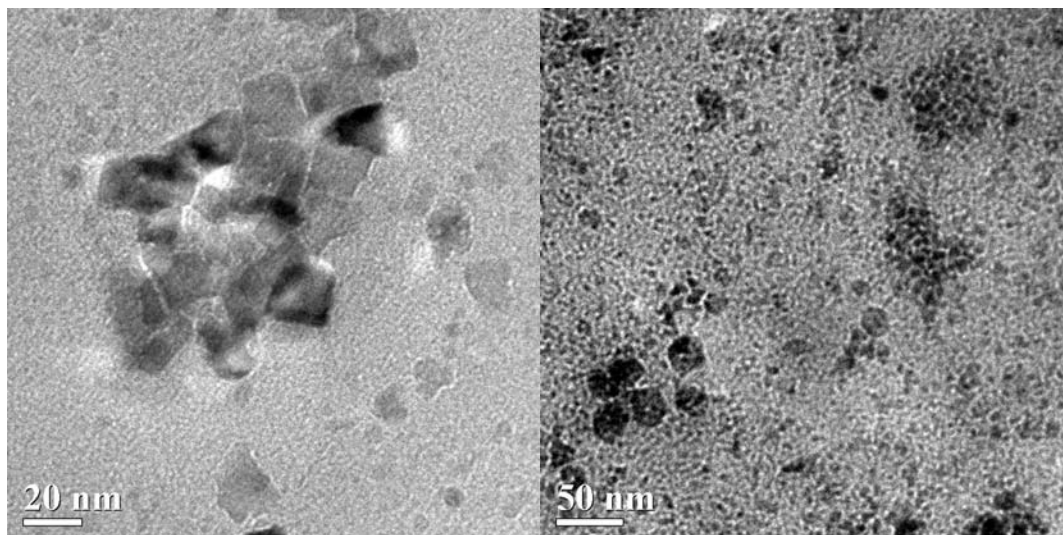


Figure 3.39 TEM images of the sediment generated from the AlMn synthesis using Na

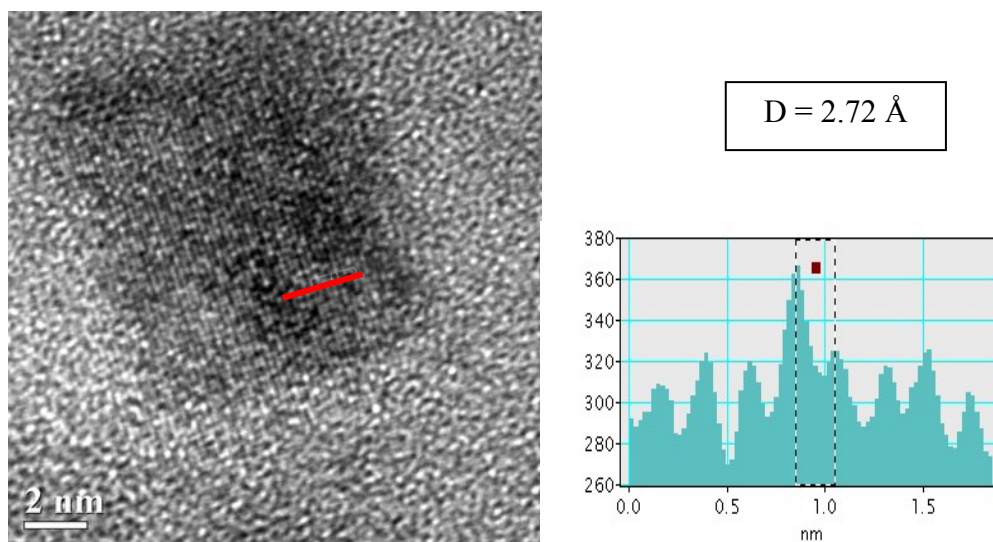


Figure 3.40 High resolution TEM image with histogram and d-spacing

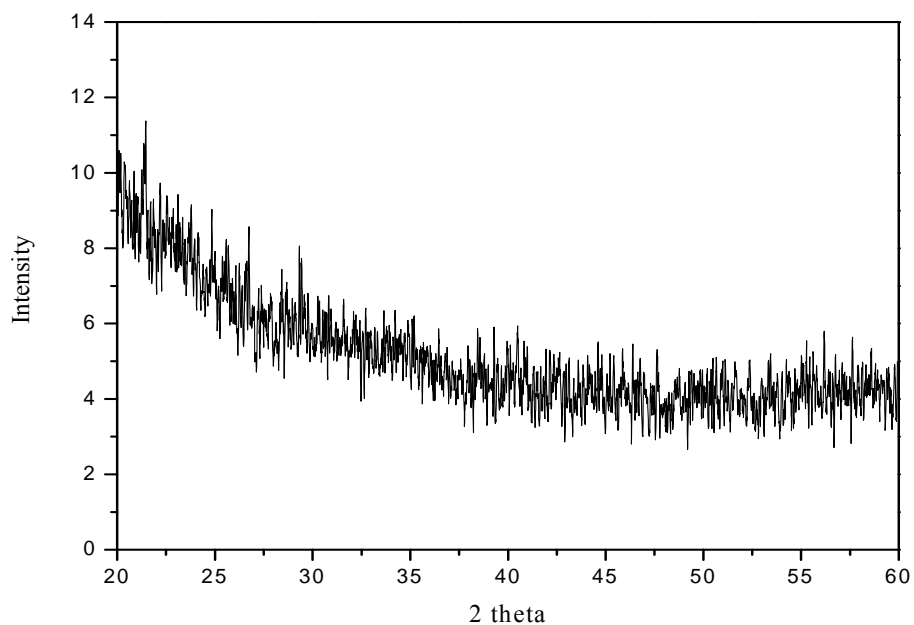


Figure 3.41 XRD spectrum from the re-dispersed particles from the AlMn synthesis

XRD analysis was done on the re-dispersed particles generated from this AlMn synthesis and the results are shown in figure 3.41. The spectrum had no peaks and the intensity was very low for this scan. The reason for this sample to produce an XRD spectrum like this was because of how small the yield was for the particles from this reaction. The particles stored in hexane were dilute compared to an FePt particle dispersion and there was not enough sample to prepare an XRD sample on a 1 x 1 cm Si wafer to get good analysis. Therefore, the XRD sample contained a dilute sample of particles which yielded an extremely low intensity in the spectrum and no visible peaks.

The particles were proven to be crystalline from TEM analysis, so TEM was used for complete analysis of the particles including imaging to get d-spacings, electron diffraction patterns, and single particle STEM-EDS to determine composition. TEM images were taken of the re-dispersed particles and an exciting discovery was made that the particles had a cube structure. Figure 3.42 shows two TEM images of the particles. The image on the left was taken a high magnification and lattice fringes are seen in the particles which are approximately 8-10 nm. The lattice fringes confirm that these particles are crystalline and since XRD analysis did not provide help in identifying the particle and its structure. The TEM image on the right in figure 3.42 shows a group of the cubic particles. This result was exciting because of the cube shaped particles that were produced. Cubic particles would be ideal for the use in magnetic tape because alignment in a magnetic field would be easier to obtain than with spherical particles. This was the first and only time to see cubic particles during this research. SEM EDS was done on the re-dispersed particles to provide the composition of Al and Mn which was found to be in the range of 43.6% and 56.4%, respectively.

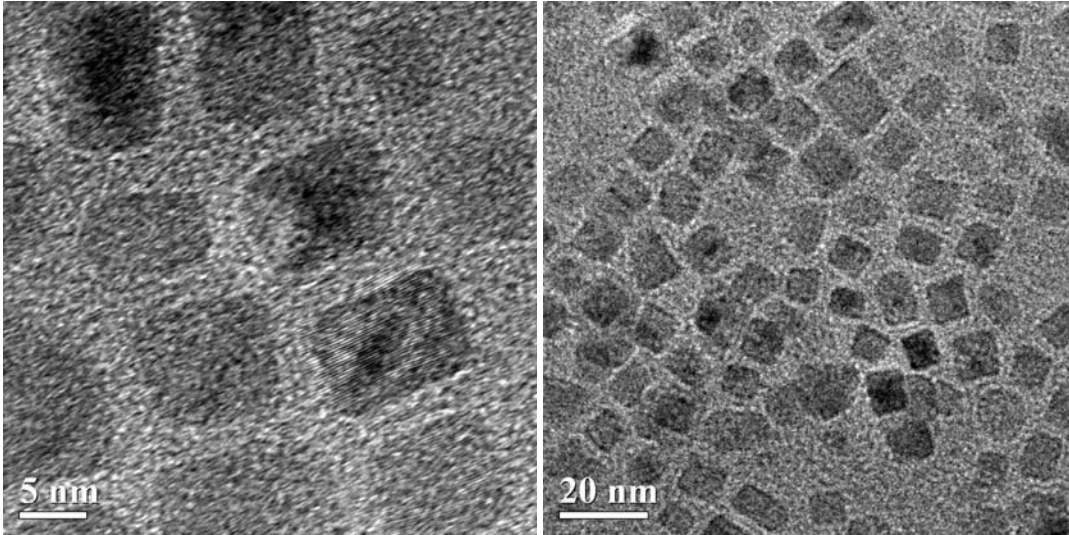


Figure 3.42 TEM images of the particles from the AlMn synthesis using Na

A hysteresis loop was performed on the AGM on a sample of the as made particles to see if the particles were magnetic, and it was shown in figure 3.43. The sample was saturated at 18 kOe, and the loop produced was smooth. The sample had a coercivity of around 100 Oe and a low moment. The hysteresis loop confirms the sample was superparamagnetic which was expected for as made particles that have not been subjected to any form of heat treatment.

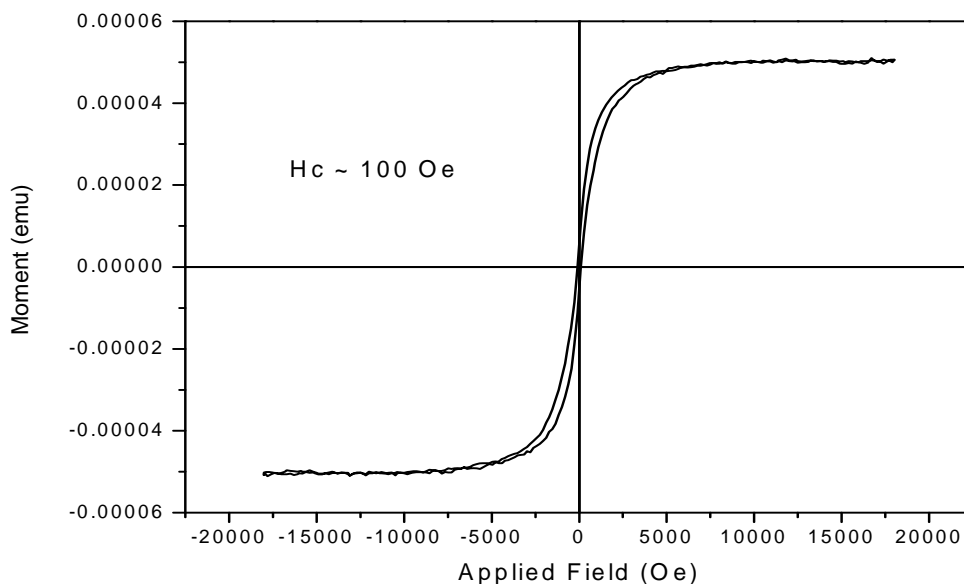


Figure 3.43 Hysteresis loop from the as made re-dispersed particles

Figure 3.44 shows two high resolution TEM images with histograms and d-spacings correlating to the lattice fringes shown in each image. The top image's histogram yielded a d-spacing of 2.18 Å which matched the {200} plane of cubic MnO. The bottom image's histogram yielded a d-spacing of 2.48 Å which matched the {001} plane of cubic MnO. SEM EDS was proved to not be accurate for the particles produced in this research, so single particle STEM-EDS on the cubic particles was performed on the TEM to determine actual composition. Figure 3.45 shows the results from single particle STEM-EDS analysis performed on the particles by the TEM. The STEM image which

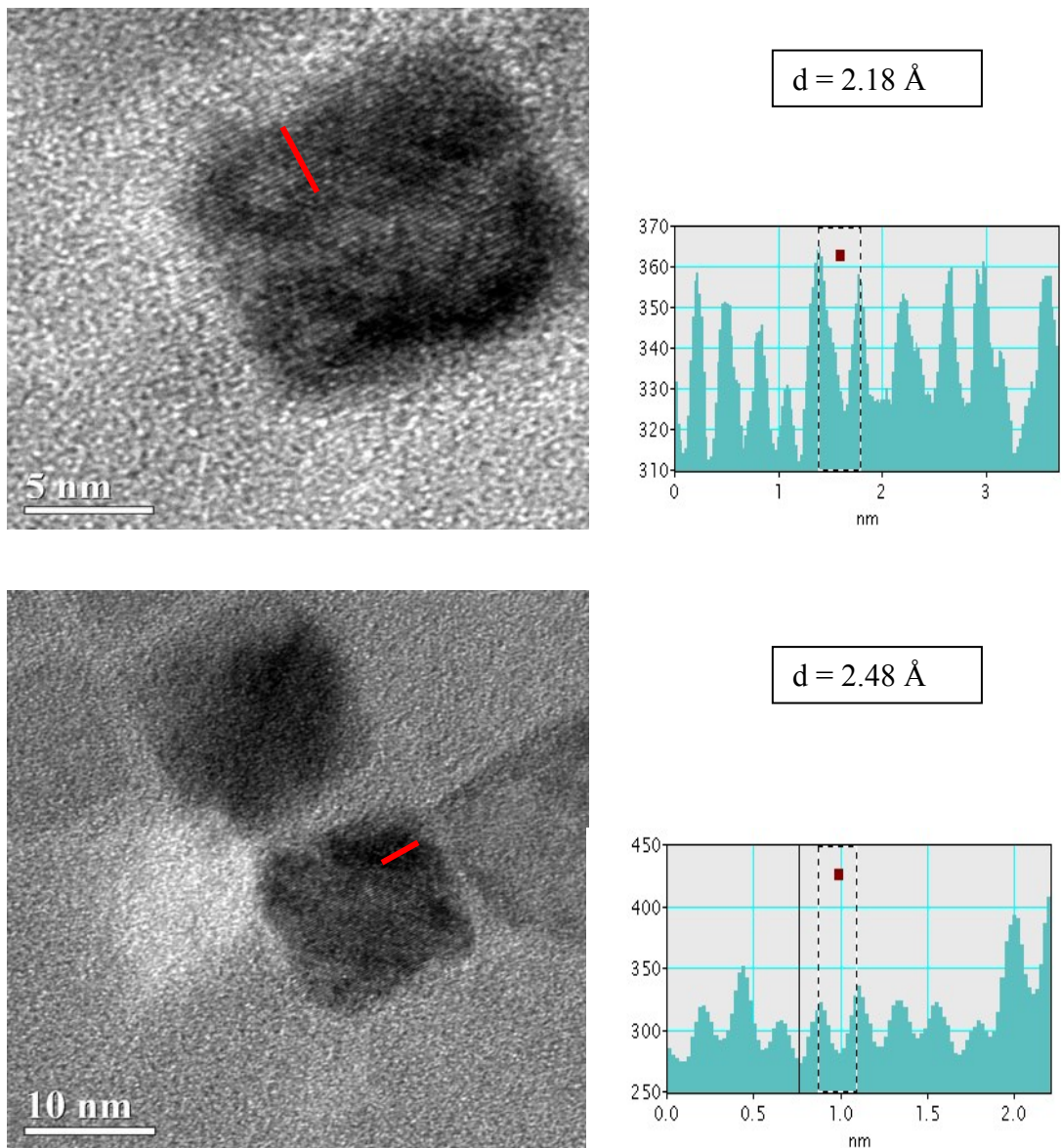


Figure 3.44 High resolution TEM images with histograms and d-spacings

was shown on the left showed a small group of the cubic particles and a circle highlighted the particle which was analyzed. The spectrum on the right in figure 3.45 was the EDS analysis results from the particle highlighted in the STEM image on the right. The peaks

that were present are labeled on the spectrum and included O₂, Na, Cu, Al, P, and Mn. The large Cu peaks were present due to the TEM grid used for analysis which was a carbon coated Cu grid. The Na, P, and Al peaks were small compared to the Mn and O₂ peaks which indicated that O₂ and Mn were the dominant elements present. Only Al, Mn, and O₂ were quantified to determine the particle's composition because it had already been determined that the structure of the particles was cubic MnO. Al was added just to see if any was present or if it was possible the particles had been misidentified. STEM-EDS analysis gave a composition of 2.4 % Al, 49.7 % Mn, and 47.9 % O₂. This confirmed that the Mn and O₂ were present in approximately a 50/50 ratio and supported the conclusion that the particles were MnO. The small amount of Al present was most likely from leftover from the reaction and not present in the crystalline matrix of the particles. Figure 3.46 shows an electron diffraction pattern taken on the TEM of a group of the cubic particles. The picture was developed and d-spacings were calculated from the diffraction rings using equation 2.5. The TEM camera length was calibrated using a known diffraction ring of fcc Al {111} and determined to be 629 mm. The exposure time for the picture was 0.1 s. The first ring in the diffraction pattern yielded a d-spacing of 2.58 Å which was indexed to the {111} plane of MnO. The second ring yielded a d-spacing of 2.48 Å which corresponded to the {001} plane of MnO.

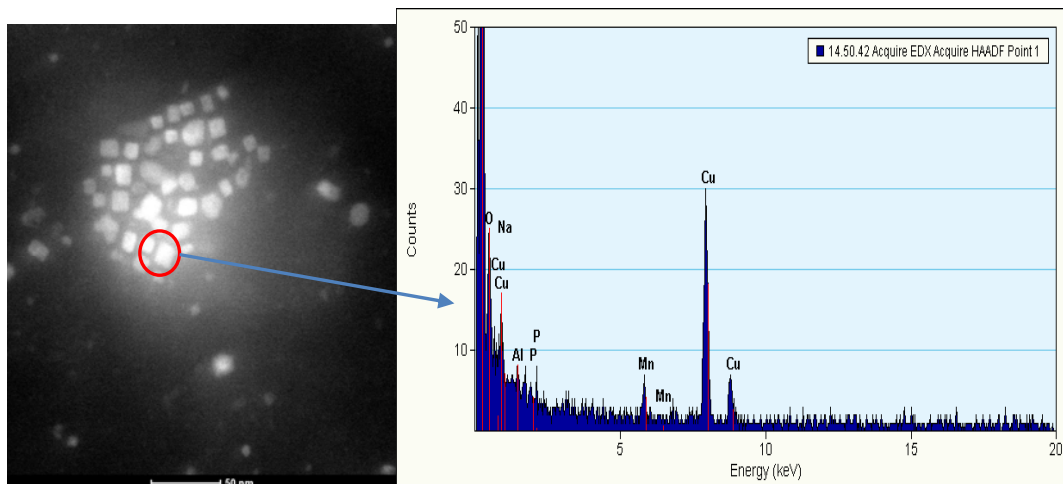


Figure 3.45 STEM-EDS of re-dispersed particles from AlMn synthesis

The third ring yielded a d-spacing of 2.18 Å which corresponded to the {200} plane of MnO. The fourth ring yielded a d-spacing of 1.55 Å which corresponded to the {220} plane of MnO. Figure 3.47 shows two more TEM images taken of the cubic particles. The image on the left shows a large group of the cubic particles which were assembled together nicely as compared to other particles generated during this research. The size distribution of the particles was not quite as narrow as hoped for the cubic particles, and there were some particles present that were lacking cubic structure as seen in figure 3.47. These issues were tried to be resolved by adjusting the amount of surfactant during the reaction, but the results remained very similar to this reaction that was chronicled. After all the analysis on the cubic particles generated from the reaction described above, it was conclusive that the particles were cubic MnO.

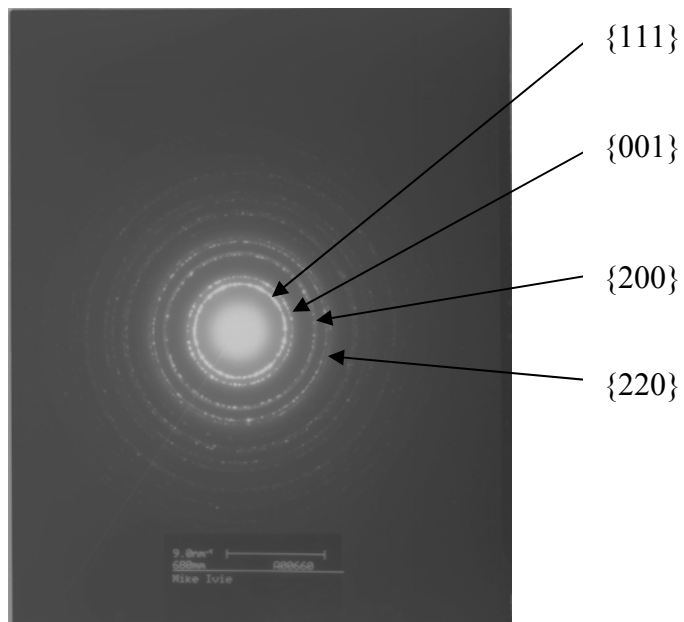


Figure 3.46 Electron diffraction pattern of the re-dispersed particles taken on the TEM

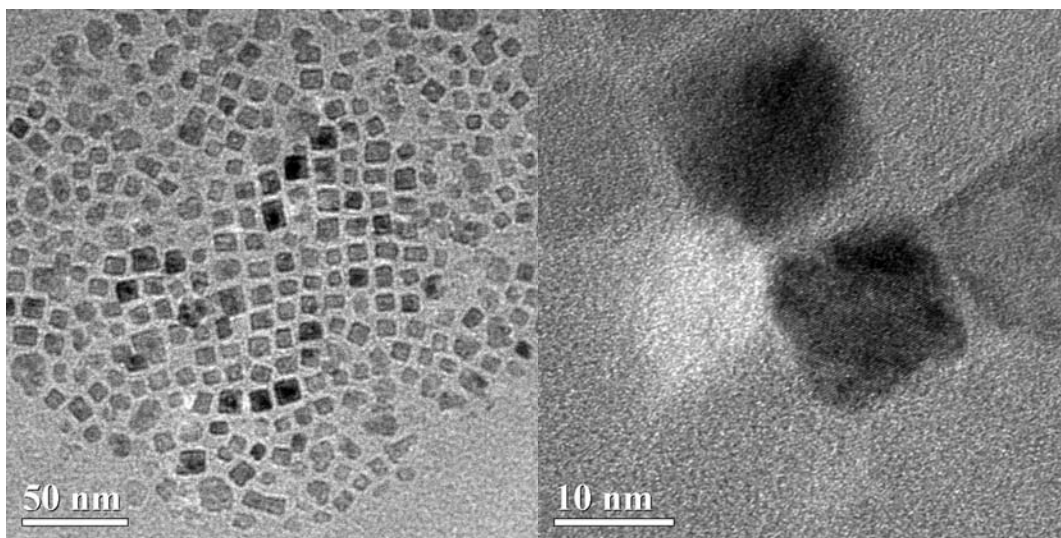


Figure 3.47 TEM images of the re-dispersed cubic particles

It was concluded that using Na to produce ferromagnetic AlMn nanoparticles was unsuccessful. Every combination of precursor, solvent, and surfactant was utilized with Na as the reducing agent to make AlMn nanoparticles. However, the reactions that were detailed in this section were the most promising of all the reaction produced during this research. The cubic particles and the ferromagnetic particles that were generated from the reactions using Na were stimulating and showed promise for this research to be successful, but all of the particles were characterized to a form of Mn oxide. Although, in the end it was determined that the goal to produce AlMn nanoparticles was not achieved using Na as a reducing agent.

3.8 AlMn(X) Tertiary Nanoparticle Syntheses

There are several tertiary alloy systems which exist that include AlMn combined with another transition metal and this section details attempts to produce nanoparticles of these systems. The idea of these synthesis attempts was to try and find a compatible transition metal that was easily reduced and could help nucleate a reaction with Al and Mn in solution. The thinking behind this type of synthesis was to use a small amount of a transition metal that could be easily reduced and early in the reaction process to form nuclei of this metal in solution. Then, later in the reaction when the Al and Mn precursors were reduced the nuclei of the added metal would help or assist the formation of a nanoparticle containing Al and Mn in solution. Research has found that the FePt system can be coupled with several transition metals such as Au, Ag, Mn, Co, etc. to

successfully create a tertiary nanoparticle system. When tertiary alloys containing FePt and another transition metal are subjected to a heat treatment, the additional transition metal departs from the system and leaves ferromagnetic L1₀ FePt nanoparticles. It is possible that a similar situation could occur with tertiary alloys containing AlMn.

Tertiary systems of AlMn exist with the following transition metals: Ni, Fe, Pt, Au, Ag, and Cu. All of these tertiary systems have a cubic structure with the exception of AlMnPt and AlMnAg which have a hexagonal structure. None of these systems exhibit a magnetic phase or possess a tetragonal phase like the binary AlMn system, but it could be possible to exploit their cubic and hexagonal structures as a precursor to the τ phase. A cubic phase is the precursor to the L1₀ phase of FePt, CoPt, and FePd, while a hexagonal phase is the precursor to the L1₀ metastable τ phase of AlMn. If Al and Mn are present in the tertiary alloy in equiatomic amounts that results in a 50:50 Al to Mn composition, then heat treatments on the cubic or hexagonal tertiary structure could result in obtaining the ferromagnetic τ phase. The attempts of creating these tertiary systems as nanoparticles by a wet chemical synthesis are documented in this section.

AlMn(X) Synthesis 1

The first synthesis attempts of this nature involved Cu as the tertiary metal. Cu was chosen because a phase of AlMnCu exists, Cu(acac)₂ is easily reduced, and Cu and Mn atoms are similar in size which may help nucleate a particle. Al and Mn precursors were added in a 1:1 molar ratio to try and yield a stoichiometry of Al₅₀Mn₅₀ to be in the

compositional range where the τ phase occurs. The Cu precursor was added in a 0.1 molar ratio (10%) to the Al and Mn precursors. Different approaches of adding the precursors were tried in these synthesis attempts. One way was to add all of the precursors at the beginning of the reaction before heating began. The idea behind this approach was that when the reducing agent was added to the reaction that all the precursors would be reduced simultaneously and the small amount of Cu would help facilitate nucleation of the Al and Mn to form a nanoparticle of AlMnCu. Another way was to add the Cu first and heat up to the nucleation point (200°C) then add the reducing agent to the solution so the Cu would be reduced and form nuclei in solution. Then, the Al and Mn precursors were added into the solution slowly to grow onto the Cu nuclei to form an AlMnCu nanoparticle.

AlMn(X) Synthesis 2

The next synthesis attempt detailed used 0.5 mmols of Al(acac)₃, 0.5 mmols of Mn(acac)₂, and 0.1 mmols of Cu(acac)₂ as precursors in 20 mL of diphenyl ether as the solvent. Also, 1 mmol of 1,2-hexadecandiol was added to the flask to initially reduce the Cu(acac)₂. The solution was heated to 100°C and 0.5 mmols of oleic acid and 0.5 mmols of oleylamine was injected as the surfactants. The solution was heated to 200°C where 2 mL of LiAlH₄ was injected as the reducing agent. The solution started out light brown in color and stayed this color until the injection of LiAlH₄ where the solution immediately turned black. The solution was heated to reflux (~260°C) for 30 minutes, and then

cooled to room temperature followed by addition of ethanol to precipitate the particles. After several hours to allow the particles to settle out, it was observed that no particles had settled out. The entire solution in the beaker was dark black with no distinction between a precipitate and the supernatant. The standard isolation and purification technique was employed for this synthesis. No particles were re-dispersed and separated using the standard procedure for this reaction product. The precipitate was kept and stored in hexane for analysis. Figure 3.48 shows the XRD spectrum from the precipitate of this synthesis. The large broad peak around $20^\circ 2\theta$ indicates that an amorphous phase is present. The small broad peaks around $45^\circ 2\theta$ and $66^\circ 2\theta$ are indexed to the {400} and the {440} planes of Al_2O_3 . The cubic AlMnCu phase has one distinct peak that occurs at $41.8^\circ 2\theta$ and none of the results from these syntheses matched. Other synthesis attempts at making AlMnCu yielded similar results of either exactly like the results of the synthesis reported or only an amorphous phase was present.

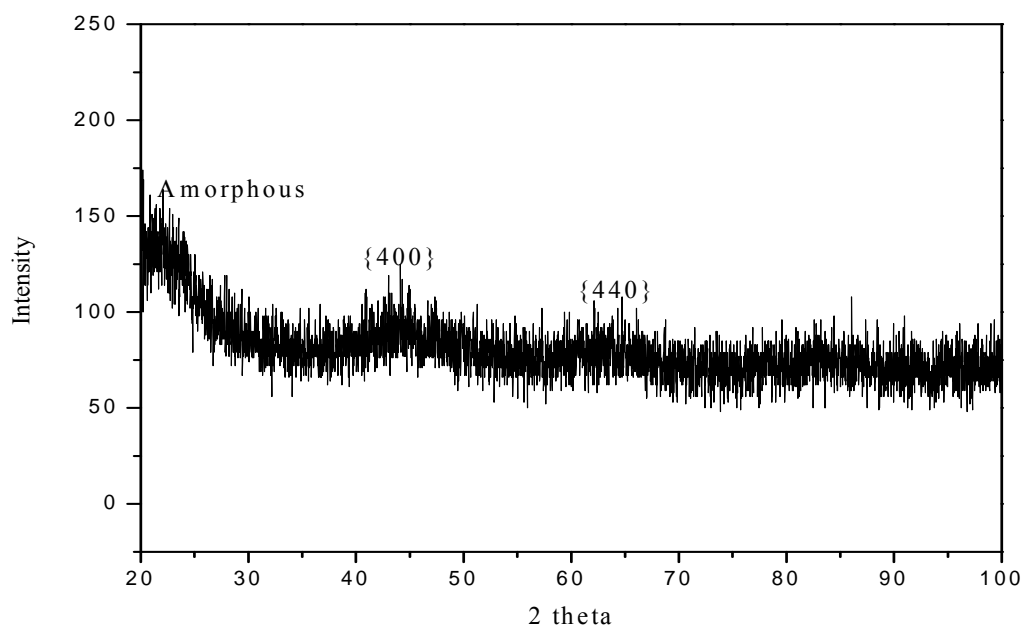


Figure 3.48 XRD spectrum of as made AlMnCu synthesis

The next synthesis attempts to produce an AlMn(X) tertiary nanoparticle used Pt as the tertiary metal. Pt is a metal that is widely used in synthesizing many binary nanoparticle systems. Pt is easily reduced and has been shown to form nuclei in solution for other metals to grow on to form binary or tertiary nanoparticle systems.

AlMn(X) Synthesis 3

The first synthesis attempt of AlMnPt nanoparticles discussed used 0.5 mmols of Al(acac)₃, 0.5 mmols of Mn(acac)₂, and 0.5 mmols of Pt(acac)₂ as precursors in 20 mL of dioctyl ether as the solvent. Also, 1 mmol of 1,2-hexadecandiol was added to the flask to initially reduce the Pt(acac)₂. The solution was heated to 100°C and 0.5 mmols of

oleic acid and 0.5 mmols of oleylamine were injected as the surfactants. The solution started out a yellowish-white color but began to turn dark brown around 140°C. After the LiAlH_4 was injected the solution turned black. The solution was heated to reflux ($\sim 287^\circ\text{C}$) for 30 minutes, then cooled to room temperature followed by the addition of ethanol to precipitate the particles. After several hours, particles settled out in the beaker but the supernatant was still dark, and the yield of particles that precipitated to the bottom of the beaker appeared extremely low. The standard isolation and purification procedure was implemented for this synthesis. A small amount of dark black particles were re-dispersed, collected, and stored in hexane for analysis. The sediment from this step was kept, and it had layers of different colors in it from gray to dark black which indicated the presence of multiple substances in the sediment. The particles were analyzed by XRD and figure 3.49 shows the results. There was one peak present around $38^\circ 2\theta$ which was indexed as the $\{111\}$ plane of Pt. This indicated that only Pt nanoparticles were produced from this synthesis. This was why there was such a low yield of particles from the reaction and the dark supernatant and the sediment leftover was most likely Al and Mn amorphous oxides. The Pt nanoparticles most likely formed before the Al and Mn were reduced and this could have helped prevent AlMn particle formation.

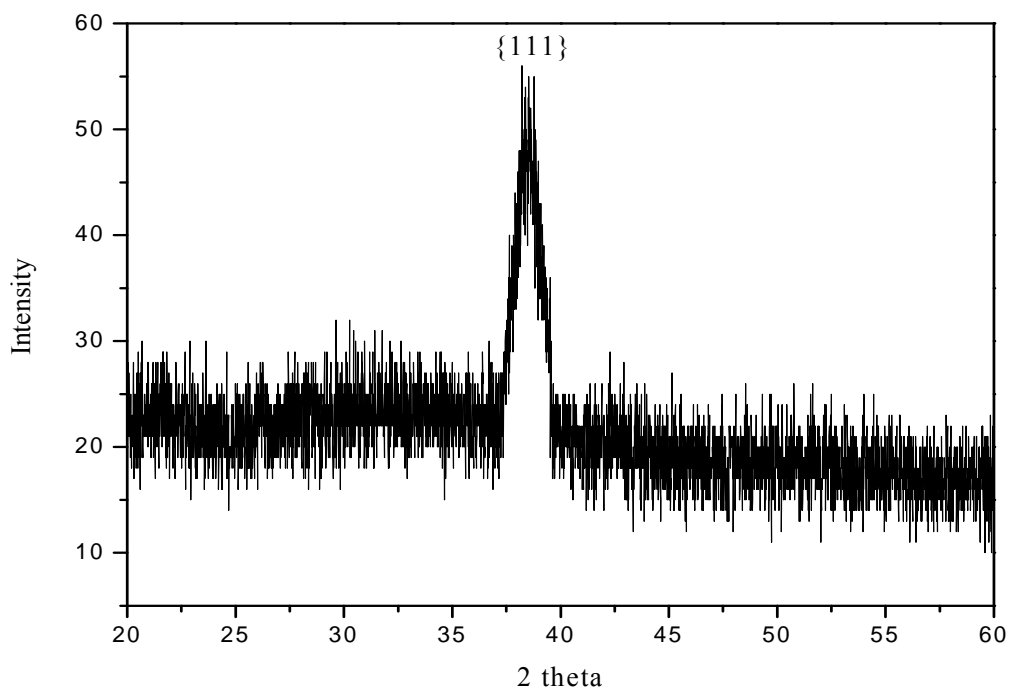


Figure 3.49 XRD spectrum of an as made AlMnPt synthesis

AlMn(X) Synthesis 4

The next discussed synthesis attempt of AlMnPt nanoparticles used 0.5 mmols of triocetylaluminum, 0.5 mmols of $\text{Mn}_2(\text{CO})_{10}$, and 0.1 mmols of $\text{Pt}(\text{acac})_2$ as precursors in 15 mL of dioctyl ether as the solvent. Also, 1 mmol of 1,2-hexadecandiol was added to the flask to initially reduce the $\text{Pt}(\text{acac})_2$. The solution was heated to 100°C and 0.5 mmols of oleic acid and 0.5 mmols of oleylamine were injected as the surfactants. The solution started out a yellowish-brown color but turned black around 130°C . The LiAlH_4

was injected at 200°C. The solution was heated to reflux (~287°C) for 30 minutes, then cooled to room temperature followed by the addition of ethanol to precipitate the particles. The standard isolation and purification procedure was used for this reaction. After several hours, there was a noticeable settling out of particles in the beaker and the supernatant was not too dark. There was a large yield of dark black particles that were re-dispersed, collected, and stored in hexane for analysis from this reaction. The sediment was kept and stored in hexane for analysis, but it was grayish-brown in color which most likely indicated the presence of oxides and/or amorphous material. The particles were analyzed by XRD and figure 3.50 shows the results. The as made particles were indexed to MnPt nanoparticles. The peak at 41° 2θ and the peak at 47° 2θ were indexed to the {111} and {200} planes, respectively of MnPt. Scherrer analysis on the {111} peak yielded an average particle size of 5.2 nm. Figure 3.51 shows a TEM image from the particles produced from this synthesis. The image showed a fairly narrow size distribution with an average particle size around 5-7 nm which confirmed the Scherrer analysis. None of the synthesis attempts produced tertiary AlMnPt nanoparticles. AlMnPt can occur in a hexagonal phase which is characterized by XRD peaks at 28°, 40.6°, 41.6°, 51.5°, 53.8°, 59.6°, and 68.2° 2θ. It can also occur in a cubic phase characterized by XRD peaks at 28.5°, 40.8°, 59°, and 66.8° 2θ.

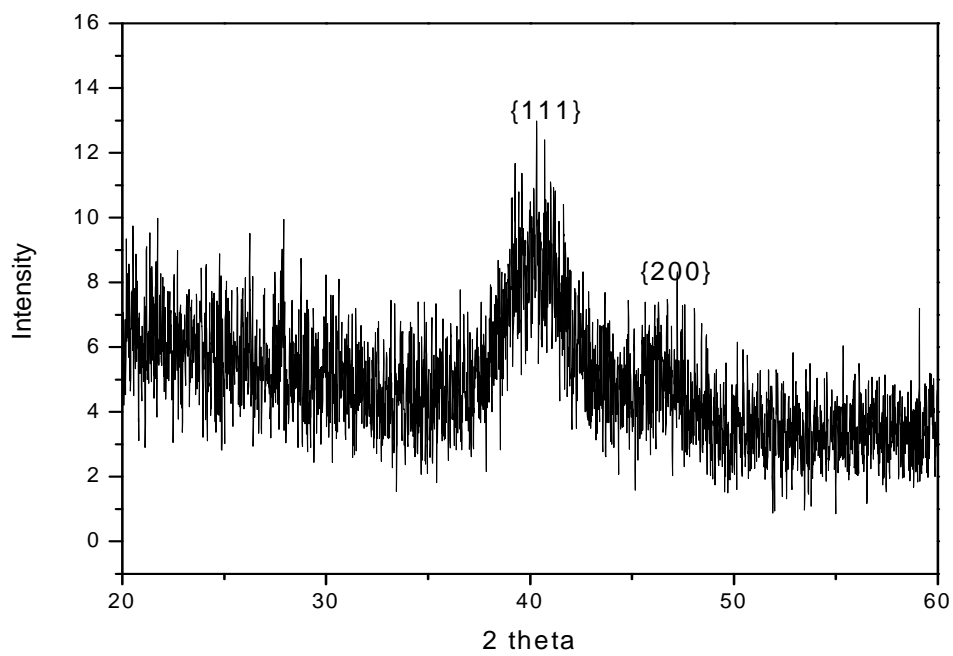


Figure 3.50 XRD spectrum of an as made AlMnPt synthesis

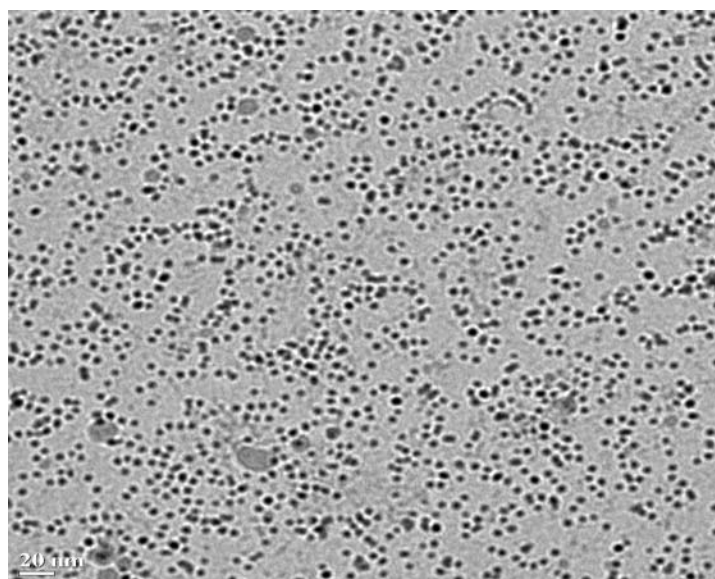


Figure 3.51 TEM images from an AlMnPt synthesis

None of the results from any of the synthesis attempts of AlMnPt could be identified as either of these phases. A few synthesis attempts were tried using Au, Ag, Ni, and Fe as the third metal for a tertiary AlMn(X) nanoparticle. These attempts were unsuccessful and yielded similar results to the synthesis routes detailed in this section.

It was concluded that using another transition metal to try and produce a tertiary AlMn(X) nanoparticle system was unsuccessful. These syntheses would not be practical for use in magnetic tapes, but it was a different idea to try and produce some form of AlMn nanoparticles. Use of Pt, Au, and Ag for making a tertiary AlMn nanoparticle would be contradictive to the purpose of AlMn nanoparticles for magnetic tape due to the high cost of those metals. Tertiary systems which including Ni, Fe, and Cu would be beneficial to produce because these metals are inexpensive and these systems exist in a cubic phase. With the lack of success in creating binary AlMn nanoparticles, the cubic phase of the tertiary AlMn(X) systems could yield a starting point for heat treatments or other techniques to transform to the metastable ferromagnetic τ phase.

3.9 Core-Shell Structured AlMn Nanoparticles

Core-shell structures of nanoparticles have been produced with transition metal nanoparticles and also metal oxides. FePt nanoparticles have been successfully coated with a shell of iron oxides, silica, and manganese oxides. The precursors to form these shells are typically added in a 2:1 molar ratio to the core nanoparticle precursors. The

idea of placing a shell around an AlMn nanoparticle is to hope that the shell could prevent oxidation and provide stability. Oxidation is not mentioned as a problem for bulk alloys and sputtered films of AlMn, but since Al and Mn prefer to exist in an oxidative state, it could play a factor on the nanoscale. Also, as seen in the results in section 3.6 that when using LiAlH_4 as a reducing agent oxidation could be a factor in producing AlMn nanoparticles. An iron oxide shell is the material chosen for these syntheses. The following section describes the attempts to produce a core-shell structure with a core of an AlMn nanoparticle and an iron oxide shell.

Core-shell Synthesis 1

The first reaction described used 0.5 mmols of $\text{Mn}_2(\text{CO})_{10}$ and 0.5 mmols of $\text{Al}(\text{acac})_3$ in 25 mL of diphenyl ether as the solvent with 2.5 mmols of Na as the reducing agent. The Al and Mn precursors along with the Na were placed in the flask with a magnetic stir bar at room temperature to begin the synthesis. The solution was heated to 100°C and 0.2 mL of oleic acid was added as the surfactant. The solution was heated to reflux ($\sim 260^\circ\text{C}$) for 30 minutes. The solution was a reddish orange color at the start of reflux, but the solution turned dark approximately 7 minutes into reflux. After 30 minutes of reflux, the solution was cooled to 100°C and 1 mL of $\text{Fe}(\text{CO})_5$ was injected into the solution. The solution was then heated to 200°C for 1 hour to allow the $\text{Fe}(\text{CO})_5$ to thermally decompose to create an iron oxide shell. The solution was cooled to room temperature and the solution was dark black. Ethanol was added to the reaction product

and after leaving overnight, but no particles precipitated. There was no distinction between the supernatant and the precipitate in the beaker because everything was dark black. The standard isolation and purification technique was used for this synthesis. No particles were re-dispersed and separated in this reaction product. The precipitate was kept and stored in hexane for analysis. The precipitate from this synthesis contained areas that were black and areas that were grey indicating the presence of multiple materials. From this result, it was inferred that this synthesis was unsuccessful and XRD analysis of the precipitate confirmed that indeed the synthesis did not produce AlMn nanoparticles. Figure 3.52 shows a broad peak at the edge of the scan at $20^\circ 2\theta$ which indicates the presence of amorphous material. A small broad peak was observed around $35^\circ 2\theta$ that corresponds to iron oxide and/or Mn oxide. There was no evidence of AlMn nanoparticles in the precipitate of this reaction.

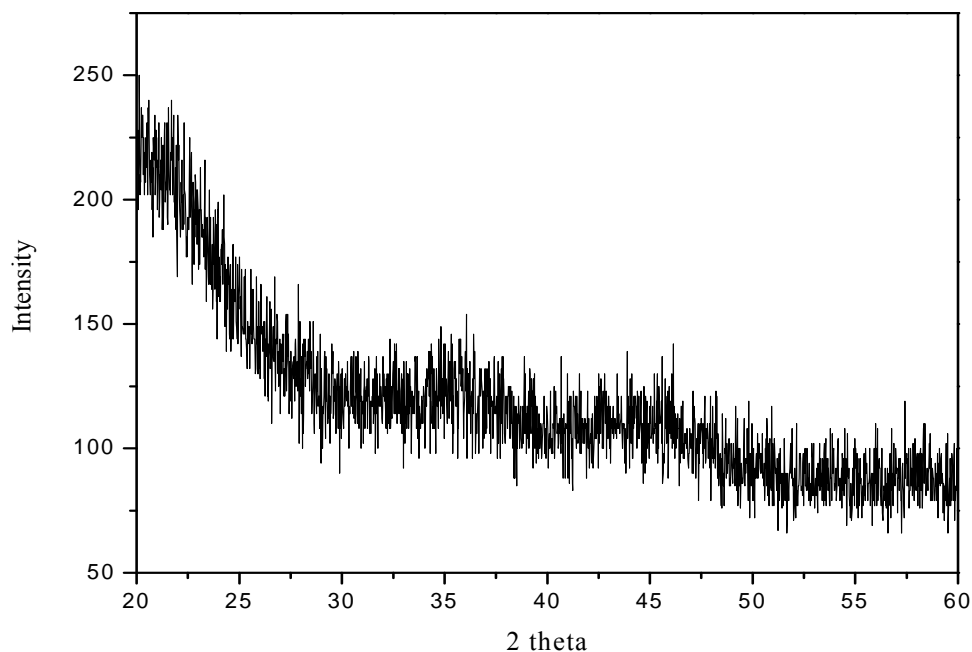


Figure 3.52 XRD spectrum of particles from a synthesis attempt of core-shell AlMn nanoparticles

Core-shell Synthesis 2

The next synthesis chronicled used were 0.5 mmols $\text{Mn}_2(\text{CO})_{10}$ and 0.5 mmols trioctylaluminum as precursors in 20 mL of diphenyl ether as the solvent with 2.5 mmols of Na as the reducing agent. These chemicals were placed into the flask at the beginning of the reaction. Another solution was prepared in a 50 mL beaker that contained 1 mmol $\text{Fe}(\text{acac})_2$ and 3 mmol 1,2-hexadecandiol in 20 mL of hexane. The initial solution was heated to 100°C and 0.2 mL of oleic acid was added as the surfactant. Then, the solution was heated to reflux ($\sim 260^\circ\text{C}$) for 30 minutes. The solution turned dark during reflux

similar to the previous reaction. The solution was cooled to 100°C and the second prepared solution was injected into the reaction flask. The hexane was distilled off, and then the solution was heated to 200°C for 1 hour followed by an additional heating to reflux for 30 minutes. The solution was cooled to room temperature and ethanol was added to precipitate the particles. Again after leaving overnight, no precipitation was observed. The standard washing and cleaning technique was used for this synthesis. No particles were re-dispersed and separated in this reaction product. The precipitate was kept and stored in hexane for analysis. The precipitate from this reaction was analyzed on the XRD and figure 3.53 shows the spectrum from this reaction. Again, there was a peak at the edge of the scan at 20° 2θ that corresponds to amorphous material in the sample. Two other peaks are observed at 34° 2θ and 68° 2θ. Both of these peaks are indexed as iron oxide.

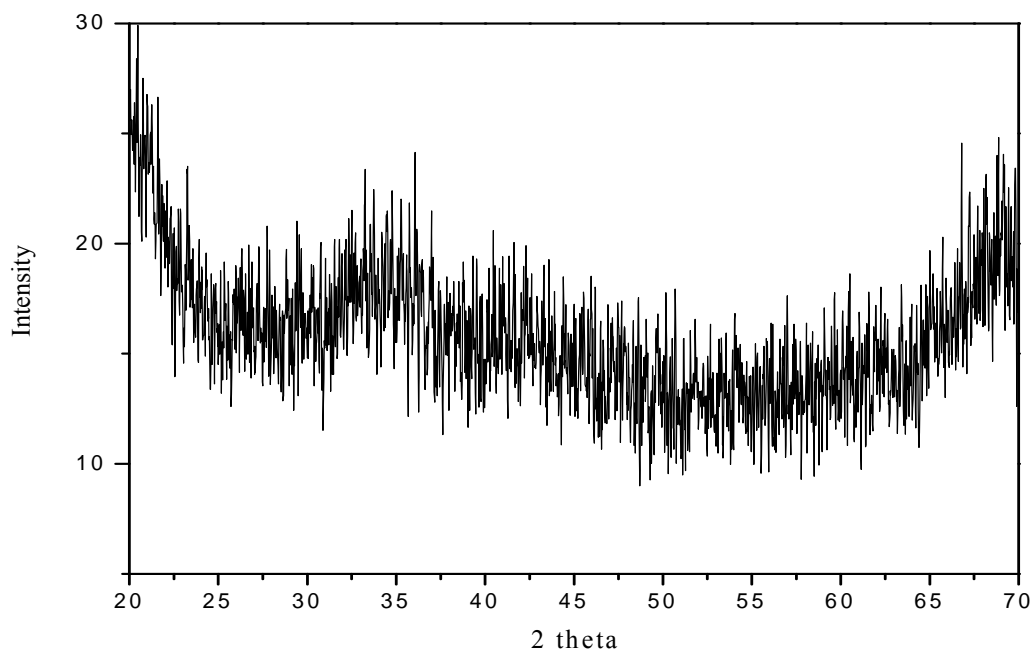


Figure 3.53 XRD spectrum of particles from a synthesis attempt of core-shell AlMn nanoparticles

Several other attempts to produce core-shell AlMn nanoparticles with an iron oxide cover failed to yield a successful synthesis. All other synthesis produced either the same results as the two reactions described here, or they produced only amorphous material. Parameters were varied such as using different precursors [$\text{Fe}(\text{acac})_2$ and $\text{Fe}(\text{CO})_5$] for the iron oxide shell, the ratio of Fe to AlMn was adjusted from 4:1, 8:1, and 10:1, and different solvents such as TOA, benzyl ether, and dioctyl ether were tried with no success. The various isolation and purification techniques listed in chapter 2 were implemented for these reactions with little to no success. It appeared the problem with

these unsuccessful synthesis attempts revolved around the AlMn nanoparticle production and not the iron oxide shell formation.

This chapter detailed the results from all of the different synthesis techniques that were attempted during this research effort to produce AlMn nanoparticles. Synthesis routes of FePt and MnPt were presented as a model to follow for synthesis attempts to make AlMn nanoparticles. Cyclic voltammetry results were described to determine reduction potentials for Al and Mn precursors used in AlMn nanoparticle syntheses to determine a suitable reducing agent. Results were presented using different reducing agents such as Na, K, LiAlH₄, superhydride, and H₂ with mixed results but none produced AlMn nanoparticles. Also, results were reported for synthesis attempts of a core-shelled structure of AlMn nanoparticles with an iron oxide shell and the synthesis attempts to produce AlMn(X) tertiary nanoparticles. XRD, AGM, XPS, SEM EDS, and TEM were the analytical tools used to characterize the particle synthesis results. XPS was determined to not be very helpful because it is a surface analyzer which tells the oxidation states of the elements present on the surface. Every time XPS was run on a sample it was determined to be in the oxidized state of Mn or Al. FePt has an outside shell of oxide on it and it is tough to make any conclusive statements from XPS analysis. Most metal nanoparticles have a small oxide layer around the particles. The difficulty was determining if the Al and Mn precursors were reduced, formed particles, and then oxidized upon contact with the atmosphere or if AlMn particles just never formed. Also, SEM EDS was not accurate for obtaining particle compositions because of the presence

of amorphous material from the reaction product. Single particle EDS was performed on some particles during this research as shown in the previous sections and produced a more accurate composition of the particles. There were many reactions mainly using LiAlH_4 and Na as the reducing agents where the solution turned black either before or during reflux indicating particle formation. Unfortunately, the particles formed as metal oxide nanoparticles in some solutions not AlMn. The ferromagnetic behavior observed in several samples as made and annealed was unable to be explained thoroughly.

Overall, the synthesis attempts to produce a reliable wet chemical method of AlMn nanoparticles were unsuccessful, and the main goal of this dissertation research effort was not met. The goal of producing ferromagnetic AlMn nanoparticles was not met, but it was important to research AlMn nanoparticles for the tape industry as a future particulate media candidate to meet future storage demands.

CHAPTER 4

CONCLUSIONS AND FUTURE WORK

After examining all of the results from the reactions performed during this dissertation it was concluded that the ultimate goal of producing ferromagnetic AlMn nanoparticles through a wet chemical synthesis was not achieved. Future work for using the AlMn system in magnetic tape could lie in thin films of ferromagnetic AlMn for ME tapes. It could be possible to combine different techniques for synthesizing nanoparticles to find a solution that would produce AlMn nanoparticles. The conclusions of this research project along with possible avenues for future work into producing AlMn nanoparticles are presented in this chapter.

Even though the main objective of this dissertation was not met, the exploration into making ferromagnetic AlMn nanoparticles was an important topic. The magnetic tape industry is searching for a candidate to meet future storage demands because today's tapes are fast approaching their thermal limit for recording capacity by decreasing particle size. The phase diagram coupled with the results from this research indicates that there are thermodynamic and kinetic issues in producing AlMn nanoparticles via a wet chemical synthesis. Thermodynamically, Al and Mn do not alloy together at low temperatures except in the compositional range of around 5-11 at % Mn according to the phase diagram. The ferromagnetic τ phase is a metastable phase that requires several processes or steps to obtain, and it occurs in the range of 50-59 at % Mn, which is a very

narrow composition distribution to obtain with nanoparticles. Kinetics is suspected of being a problem for making AlMn nanoparticles also. At low temperatures during a wet chemical synthesis, Al and Mn do not like to nucleate and grow into alloys or particles. Oxidation is an important parameter in this research and the AlMn nanoparticles could be oxidized when they are exposed to the atmosphere, from ethanol or methanol to precipitate the particles, or it could be from the acetylacetonate precursors which tend to form CO₂ in the reaction when they are reduced. These are some of the difficulties that reside with producing a wet chemical synthesis of AlMn nanoparticles.

Several suggestions are given on possible avenues to explore if any future work on this research topic is pursued. To produce AlMn nanoparticles via a solution phase synthesis maybe a combination of the techniques for producing metal nanoparticles that were detailed in section 1.4 could be used in the future. For example, maybe it would be possible to use a combination of an electrochemical deposition, a wet chemical method of reduction of metal salt precursors, a reduction of organic ligands in organometallic precursors, and metal vapor chemistry. High surface area core-shell metal nanoparticles have been produced using a combination of a wet chemical reduction of metal salts and a wet chemical reduction of metal salts. This research effort exhausted most all possibilities of producing AlMn nanoparticles via a wet chemical synthesis. The highest boiling point solvents and the strongest reducing agents were used with no success. The one area that could possibly be expanded to try and make AlMn nanoparticles would be to focus on developing a core-shell structure comprised of a center of AlMn and a shell of

silica, iron oxide, etc. to prevent any oxidation and stabilize the core of AlMn. This research briefly explored this idea by coating an AlMn nanoparticle with an iron oxide shell. The results from those synthesis attempts were unsuccessful, but maybe it could be feasible with a lot of fine tuning of the process. Another avenue to further explore would be creating tertiary AlMn(X) alloys using Cu, Fe, or Ni as the third element. These other metals are relatively inexpensive and they form cubic phases which could be a good precursor for producing the τ phase. For the magnetic recording industry, the idea of creating a monodispersed array of ferromagnetic AlMn nanoparticles for use in tapes may not be realistic, but the use of AlMn thin films for metal evaporated (ME) tapes could be of great interest. Future work on creating a material containing ferromagnetic AlMn may be in the area of thin films for ME tapes instead of AlMn nanoparticles for particulate media tapes. The ferromagnetic τ phase of AlMn has been successfully sputtered in the form of thin films on a substrate by many researchers. Several research efforts as mentioned in section 1.2 have produced films of AlMn containing the τ phase which exhibits good magnetic properties including high coercivity and magnetization. Studies show that the τ phase can be sputtered epitaxially onto substrates such as gallium arsenide (GaAs) with the “easy” c-axis of the tetragonal crystal parallel to the substrate which provides perpendicular magnetization. Recently within the recording industry, ME tapes have been explored as digital data storage alternatives to particulate tapes due to particulate tapes coming closer to their theoretical limits. High coercivity films on flexible substrates demonstrate superior performance in high frequency recording. This

technology can increase the capacity of tape storage products by increasing the areal density of the tape media. The inherent problem of thin films on tape is brittleness which can subsequently cause failure of the media. Most metal thin films that have been used for ME tapes contain a cobalt based alloy. With many studies producing thin films with single phases of the ferromagnetic τ phase of AlMn, this alloy system could be a prime candidate for use in ME tapes. Sometimes it is possible that lofty goals are unattainable during the research time period, and a concrete and final solution is not within reach, such is the case for AlMn nanoparticles.

APPENDIX
EQUATIONS

(1.1) Calculation for crystalline anisotropies: $E = KV\sin^2\theta$30

To use this equation it is assumed that the array of particles is comprised of uniaxial, single domain particles. The variables in this equation are the following: K is the anisotropy constant (erg/cc), V is the volume, and θ is the angle between M_s and the easy axis. If the volume of particles is V, then the energy barrier ΔE that must be overcome before a particle can reverse its magnetization is KV ergs.

(1.2) Sharrock equation: $H_c(t) = H_0 \{1 - [kT/KV\ln(f_0t/0.693)]^{1/m}\}$31

Sharrock's law is used to determine a medium's thermal stability by extracting KV/kT data. The parameters of Sharrock's law are as follows: H_c = medium coercivity, H_0 = intrinsic coercivity, k = Boltzmann's constant, T = temperature, K = anisotropy constant, V = volume, t = time, $f_0 = 1 \times 10^9$, and m = constant. The most important information that can be extracted from the Sharrock equation is the particle's thermal stability, KV/kT.

(1.3) Calculation for the time before media spontaneously reverses magnetization: $t = 1/f_0\exp(KV/kT)$31

KV/kT data can be plugged into the Arrhenius equation to calculate the time before the media spontaneously reverses magnetization and data is lost. Values for media used for magnetic recording are on the order of KV/kT > 60, which equals a time of 10^9 years.

(2.1) Bragg's Law: $n\lambda = 2d\sin\theta$48

In XRD, only the planes in crystalline materials which satisfy Bragg's Law will generate diffraction peaks. The parameters of Bragg's Law are defined as follows: n is the diffraction order (usually 1), λ is the wavelength of the incident x-ray, d is the spacing between the two adjacent planes (d-spacing), and θ is the diffraction angle of corresponding planes.

(2.2) **D-spacing hexagonal eqn:** $1/d_{hkl}^2 = 4/3(h^2 + hk + k^2/a^2) + l^2/c^2$50

D-spacings for individual planes can be calculated for the hexagonal structured ϵ phase. The parameters for this equation are as follows: d = d-spacing, hkl = the miller indices for each plane, and lattice parameters a and c . The calculated d-spacings can then be put into Bragg's Law to calculate 2θ .

(2.3) **D-spacing tetragonal eqn:** $1/d_{hkl}^2 = (h^2 + k^2)/a^2 + l^2/c^2$50

D-spacings for individual planes can be calculated for the tetragonal structured τ phase. The parameters for this equation are as follows: d = d-spacing, hkl = the miller indices for each plane, and lattice parameters a and c . The calculated d-spacings can then be put into Bragg's Law to calculate 2θ .

(2.4) **Scherrer equation:** $d = k\lambda/\beta\cos\theta$52

For samples of nanoparticles, the width of diffraction peaks can be directly correlated to the average size of the particles by using the Scherrer equation. The parameters of this equation are defined as follows: d is the size of the particles, k is a coefficient (0.9), λ is the wavelength of incident x-ray, β is the full width a half maximum (FWHM) of the largest diffraction peak, and θ is the diffraction angle.

(2.5) **D-spacings from electron diffraction:** $dR = \lambda L$55

The diffraction patterns are taken by a camera on the TEM, and then the film is developed into an image with diffraction rings. This equation is used to determine d-spacing from electron diffraction patterns taken on the TEM. The parameters of this equation are defined as follows: d -spacing (\AA), R is the radius of the diffraction ring (mm), λ is the wavelength of the electron beam (0.0254\AA), and L is the camera length (mm).

(2.6) **Binding energy in XPS:** $BE = h\lambda - KE - \Phi$64

The binding energy of ejected electrons is characteristic of the elements and the oxidation states of the elements. The parameters of this equation are defined as follows: BE is the binding energy of the electron emitted from one electron configuration within the atom, KE is the kinetic energy of the emitted electrons as measured by the instrument, $h\lambda$ is the energy of the incident x-ray photon, and Φ is the work function of the spectrometer. From this equation, the instrument collects a spectrum based on binding energy.

REFERENCES

1. Wang, S.X. and A.M. Taratorin, *Magnetic Information Storage Technology*. 1999: Academic Press.
2. Sharrock, M.P., *Recent Advances in Metal Particulate Media: Toward the Ultimate Particle*. IEEE Transactions on Magnetics, 2000. **36**(5): p. 2420-2425.
3. Mee, C.D. and E.D. Daniel, *Magnetic Recording Technology, Second Edition*. 1996: McGraw-Hill.
4. Cullity, B.D., *Introduction to Magnetic Materials*. 1972, Reading, Ma: Addison-Wesley Publishing Company, Inc.
5. Consortium, I.S.I., *International Magnetic Tape Storage Roadmap*.
6. Berman, D., et al, IEEE Transactions on Magnetics, 2007. **43**: p. 3502-3504.
7. Matsumoto, A., et al, IEEE Transactions on Magnetics, 2006. **42**: p. 2315-2317.
8. Nagata, T., et al., IEEE Transactions on Magnetics, 2006. **42**: p. 2312-2314.
9. Sasaki, Y., et al., *Development of NanoCAP Technology for High-Density Recording*. IEEE Transactions on Magnetics, 2005. **41**(10): p. 3241-3243.
10. Shouheng Sun, C.B.M., Dieter Weller, Liesl Folks, Andreas Moser, *Monodispersed FePt Nanoparticles and Ferromagnetic FePt Nanocrystal Superlattices*. Science Magazine, 2000. **287**: p. 1989-1992.
11. Sun, S., Murray, C.B., Doyle, H., Materials Research Society Symposium Proceedings, 1999(577): p. 385.
12. Sun, S., Murray, C.B., Journal of Applied Physics, 1999. **85**: p. 4325.
13. Kono, H., *On the Ferromagnetic Phase in the Manganese-Aluminum System*. Journal of the Physical Society of Japan, 1958. **13**(12): p. 1444-1451.

14. A.J.J. Koch, P.H., M.G. Van Der Steeg, and K.J. de Vos, *New Material for Permanent Magnets on a Base of Mn and Al*. Journal of Applied Physics, 1960. **31**(5): p. 75S-77S.
15. Braun, P.B., *An X-ray and Neutron Diffraction Investigation of the Magnetic Phase Al_{0.89}Mn_{1.11}*. Acta Crystallographica, 1963. **16**: p. 737-740.
16. K. Kamino, T.K., and M. Nagakura, *Magnetic Properties of MnAl System Alloys*. IEEE Transactions on Magnetics, 1966. **Mag-2**(3): p. 506-510.
17. J.J. Van Den Broek, H.D., G. Van Tendeloo, and J. Van Landuyt, *Phase Transformations in Pure and Carbon-Doped Al₄₅Mn₅₅ Alloys*. Acta Metallurgical, 1979. **27**: p. 1497-1504.
18. Hindricks, G., Z. Anorg. Chem., 1908. **59**: p. 444.
19. Ishiwara, T., Kinzoku no Kenkyu (Japanese), 1926. **3**: p. 13.
20. W. Koster, W.B., Z. Metallk., 1938. **30**: p. 294.
21. J.J. Wyslocki, P.P., A. Przybyl, *Magnetic properties of the non-oriented ε-phase in Mn-Al-C permanent magnet*. Materials Chemistry and Physics, 1999. **60**: p. 211-213.
22. Stafford, G.R., Grushko, B., McMichael, R.D., *The electrodeposition of Al-Mn ferromagnetic phase from molten salt electrolyte*. Journal of Alloys and Compounds, 1993. **200**: p. 107-113.
23. Kojima, S.e.a., AIP Conference Proceedings, 1974. **24**: p. 768.
24. Vintaykin, Y.Z.e.a., Physical Metallurgy, 1974. **38**(2): p. 157.
25. Hoydick, D.P., Palmiere, E.J., Soffa, W.A., *Microstructural development in Mn-Al base permanent magnet materials: New perspectives*. Journal of Applied Physics, 1997. **81**(8): p. 5624-5626.
26. Yanar, C., Wiezorek, J.M.K., Radmilovic, V. Soffa, W.A., *Massive Transformation and the Formation of the Ferromagnetic L10 Phase in Manganese-Aluminum Based Alloys*. Metallurgical and Materials Transactions A, 2002. **33A**: p. 2413-2423.

27. P. Mullner, B.E.B., H. Heinrich, A.S. Sologubenko, and G. Kostorz, *Observation of the shear mode of the ϵ phase transformation in a Mn-Al-C single crystal*. Philosophical Magazine Letters 2002. **82**(2): p. 71-79.
28. Pareti, L., Bolzoni, F., Leccabue, F., *Magnetic anisotropy of MnAl and MnAlC permanent magnet materials*. Journal of Applied Physics, 1986. **59**(11): p. 3824-3828.
29. McAlister, A.J., Murray, J.L., *Al-Mn (Aluminum Manganese)*. Binary Alloy Phase Diagram, 1987: p. 171-174.
30. Liu, X.J., Ohnuma, I., Kainuma, R., Ishida, K., *Thermodynamic Assessment of the Aluminum-Manganese (Al-Mn) Binary Phase Diagram*. Journal of Phase Equilibria, 1999. **20**(1): p. 45-56.
31. X.J. Liu, R.K., H. Ohtani, K. Ishida, *Phase equilibria in the Mn-rich portion of the binary system Mn-Al*. Journal of Alloys and Compounds, 1996. **235**: p. 256-261.
32. Huang, J.H., Kuo, P.C., Shen, S.C., *High Coercivity and High Saturation Magnetization Mn-Al Thin Films*. IEEE Transactions on Magnetics, 1995. **31**(5): p. 2494-2498.
33. J. De Boeck, W.V.R., C. Bruynseraede, A. Van Esch, H. Bender, C. Van Hoof and G. Borghs, *Ferromagnetic Mn-based Thin Films with Perpendicular Magnetization on Semiconductors*. Physica Scripta, 1996. **T66**: p. 183-189.
34. A. Morisako, M.M.a.M.N., *Sputtered Mn-Al-Cu Films for Magnetic Recording Media*. IEEE Transactions on Magnetics, 1987. **Mag-23**(5): p. 2470-2472.
35. Matsumoto, A.M.a.M., *Synthesis of ferromagnetic τ -phase of Mn-Al films by sputtering*. Journal of Applied Physics, 1987. **61**(8): p. 4281-4283.
36. Takeuchi, T., Hirayama, Y., Futamoto, M., *Structure and magnetic properties of Mn-Al multilayered films*. Journal of Applied Physics, 1990. **67**(9): p. 4465-4467.
37. Lauhoff, G.e.a., *Ferrimagnetic τ -MnAl/Co Superlattices on GaAs*. Physical Review Letters, 1997. **79**(26): p. 5290-5293.
38. Kuo, P.C., Yao, Y.D., Huang, J.H., Chen, C.H., *Preparation and magnetic studies of Mn₅₀Al₅₀/Al bilayer films*. Journal of Applied Physics, 1997. **81**(8): p. 5253-5255.

39. Yan, Z.C., Huang, Y., Zhang, Y., Hadjipanayis, G.C., Soffa, W. Weller, D. , *Magnetic and structural properties of MnAl/Ag granular thin films with L10 structure*. Scripta Materialia, 2005. **53**: p. 463-468.
40. G.R. Stafford, B.G., and R.D. McMichael *The electrodeposition of Al-Mn ferromagnetic phase from molten salt electrolyte*. Journal of Alloys and Compounds, 1993. **200**: p. 107-113.
41. Li, J.C., Nan, S.H., Jiang, Q., *Study of the electrodeposition of Al-Mn amorphous alloys from molten salts*. Surface Coatings and Technology, 1998. **106**: p. 135-139.
42. Hernandez, T., Bautista, C., Martin, P., *Synthesis and thermal evolution of Mn-doped alumina nanoparticles by homogeneous precipitation with urea*. Materials Chemistry and Physics, 2005. **92**: p. 366-372.
43. E. Fazakas, L.K.V., F. Mazaleyrat, *Preparation of nanocrystalline Mn-Al-C magnets by melt spinning and subsequent heat treatments*. Journal of Alloys and Compounds, 2007. **434-435**: p. 611-613.
44. Buschow, K.H.J. and F.R. de Boer, *Physics of Magnetism and Magnetic Materials*. 2004: Kluwer Academic Publishers.
45. Leslie-Pelecky, D.L., *Magnetic Properties of Nanostructured Materials*. Journal of the American Chemical Society, 1996. **8**(8): p. 1770-1783.
46. C.B. Murray, C.R.K., and M.G. Bawendi, *Synthesis and Characterization of Monodispersed Nanocrystals and Close-Packed Nanocrystal Assemblies*. Annual Review Material Science, 2000. **30**: p. 545-610.
47. Elena V. Shevchenko, D.V.T., Heimo Schnablegger, Andreas Kornowski, Orjan Festin, Peter Svedlindh, Markus Haase, and Horst Weller, *Study of Nucleation and Growth in the Organometallic Synthesis of Magnetic Alloy Nanocrystals: The Role of Nucleation Rate in Size Control of CoPt₃ Nanocrystals*. Journal of the American Chemical Society, 2003. **125**(30): p. 9090-9101.
48. Peng, X., Wickham, J., Alivisatos, A.P., *Kinetics of II-VI and III-V Collodial Semiconductor Nanocrystal Growth: "Focusing" of Size Distributions*. Journal of the American Chemical Society, 1998. **120**: p. 5343-5344.

49. Leff, D.V., Ohara, P.C., Heath, J.R., Gelbart, W.M., *Thermodynamic Control of Gold Nanocrystal Size: Experiment and Theory*. Journal of Physical Chemistry, 1995. **99**: p. 7036-7041.
50. Park, S.J., Kim, S., Lee, S., Khim, Z.G., Chan, K., Hyeon, T.J., Journal of the American Chemical Society, 2000. **122**: p. 8581.
51. Murray, C.B., Sun, S., Doyle, H., Betley, T. , MRS Bulletin, 2001: p. 985.
52. Puentes, V.F., Krishan, K.M., Alivisatos, A.P., Science Magazine, 2001. **291**: p. 2115.
53. Shevchenko, E.V., Talapin, D.V., Rogach, A.L., Kornowski, A., Haase, M., Weller, H., *Colloidal Synthesis and Self-Assembly of CoPt₃ Nanocrystals*. Journal of the American Chemical Society, 2002. **124**: p. 11480-11485.
54. Sun, S., Murray, C.B., Weller, D., Folks, L., Moser, A., *Monodisperse FePt Nanoparticles and Ferromagnetic FePt Nanocrystal Superlattices*. Science Magazine, 2000. **287**: p. 1989-1992.
55. La Mer, V.K., Dinegar, R. H., Journal of the American Chemical Society, 1950. **72**: p. 4847-4854.
56. Reiss, H., Journal of the American Chemical Society, 1951. **19**: p. 482.
57. Talapin, D.V., Rogach, A.L., Haase, M., Weller, H., *Evolution of an Ensemble of Nanoparticles in a Colloidal Solution: Theoretical Study*. Journal of Physical Chemistry, 2001. **B(105)**: p. 12278-12285.
58. De Smet, Y., et al, Langmuir, 1997. **13**: p. 6884-6888.
59. Gratz, H., Scripta Materialia, 1997. **37**: p. 9-16.
60. Steigenwald, M.L., Journal of the American Chemical Society, 1988. **110**: p. 3046-3051.
61. Murray, C.B.e.a., Journal of the American Chemical Society, 1993. **115**(8706-8715).
62. Yamaki, M., Higo, J., Langmuir, 1995. **11**: p. 2975-2978.

63. Ohara, P.C., et al, *Physics Review Letters*, 1995. **75**: p. 3466-3469.
64. Salguerino-Maceira, V., Liz-Marzan, L.M., Farle, M., *Water-Based Ferrofluids from FePt Nanoparticles Synthesized in Organic Media*. *Langmuir*, 2004. **20**: p. 6946-6950.
65. Lee, D.C., et al, *Synthesis and Magnetic Properties of Colloidal MnPt₃ Nanocrystals*, *Journal of Physical Chemistry B*, 2006, Vol. 110, 42, p. 20906-20911.
66. Seo, W.K., et al, *Size-Dependent Magnetic Properties of Colloidal Mn₃O₄ and MnO Nanoparticles*, *Angewandte Chemie*, 2005, 43, p. 1115-1117.
67. McHenry, M., Soffa, W.A., *Preface to viewpoint set on: L10 phases for permanent magnet and recording applications*, *Scripta Materialia*, 2005, 53, p. 381-382.
68. Pachon, L.D., Rothenberg, G., *Transition Metal Nanoparticles: Synthesis, Stability, and the Leaching Issue*, *Applied Organometallic Chemistry*, 2008, 22, p. 288-299.
69. Fredriksson, P., Sundman, B., *A Thermodynamic Assessment of the Fe-Pt System*, *National Institute for Materials Science*, 2001, 25, p. 535-548.
70. Williams, D., Carter, C., *Transmission Electron Microscopy, A Textbook for Materials Science, Volumes I-IV*.